

**EXPERIMENTAL INVESTIGATION OF THE FLOW FIELD  
IN THE VICINITY OF THE SUCTION INLET OF A MODEL  
CUTTER SUCTION DREDGE**

A Thesis

by

COLIN PATRICK DISMUKE

Submitted to the Office of Graduate Studies of  
Texas A&M University  
in partial fulfillment of the requirements for the degree of

MASTER OF SCIENCE

May 2012

Major Subject: Ocean Engineering

**EXPERIMENTAL INVESTIGATION OF THE FLOW FIELD  
IN THE VICINITY OF THE SUCTION INLET OF A MODEL  
CUTTER SUCTION DREDGE**

A Thesis

by

COLIN PATRICK DISMUKE

Submitted to the Office of Graduate Studies of  
Texas A&M University  
in partial fulfillment of the requirements for the degree of

MASTER OF SCIENCE

Approved by:

Chair of Committee,	Robert E. Randall
Committee Members,	Scott A. Socolofsky
	Gerald L. Morrison
Head of Department,	John M. Niedzwecki

May 2012

Major Subject: Ocean Engineering

## **ABSTRACT**

Experimental Investigation of the Flow Field in the Vicinity of the Suction Inlet  
of a Model Cutter Suction Dredge. (May 2012)

Colin Patrick Dismuke, B.S., Texas A&M University

Chair of Advisory Committee: Dr. Robert E. Randall

The purpose of this thesis is to describe the three-dimensional velocity flow field measurements in the vicinity of the inlet mouth of a cutterhead suction dredge. Using acoustic Doppler velocimeters (ADV), an accurate visualization of the velocity flow field was used to determine the region of influence around the cutterhead. Similitude is used in the experimental study to determine the correlation between the velocity flow field and other dredge parameters such as suction intake diameter without the cutterhead and with a rotating cutterhead. This is useful to the dredging community for two reasons: first, knowing the region of influence around the cutterhead helps the dredger achieve higher production by using a more efficient cutting depth and second, achieving similitude with the velocity flow field allows for more accurate model testing in the future.

In order to help understand the more complex flow field around the cutterhead created by the cutting process, scenarios involving three different suction flow rates, three cutterhead rotation speeds, and two swing speeds, were investigated.

Prior studies of the flow field around the cutterhead provided a means to predict the velocity at the cutterhead intake. The flow field studies herein provide an extension into three dimensions as well as a verification of the previous results.

The highest velocities were found to occur nearest the cutterhead, specifically in the lower hemisphere of the cutterhead where the suction intake is located. The magnitude of these values greatly decreased with increasing distance from the cutterhead. In addition, the flow rate is shown to directly correlate to the velocity around the cutterhead.

It was found that the region of influence was nearly symmetrical around the cutterhead, but the shape could more accurately be described as an ellipsoid. The volumes of the regions of influence ranged from 10 ft<sup>3</sup> (0.283 m<sup>3</sup>) to 80 ft<sup>3</sup> (2.27 m<sup>3</sup>) for the model dredge and from 2,250 ft<sup>3</sup> (63.70 m<sup>3</sup>) to 17,000 ft<sup>3</sup> (481.40 m<sup>3</sup>).



## ACKNOWLEDGEMENTS

I would like to thank Dr. Robert E. Randall for his support and guidance throughout the process of completing this thesis. Without it, this would not have been possible. My knowledge and fondness of dredging has increased greatly from just a year ago. I would also like to thank Dr. Scott A. Socolofsky and Dr. Gerald L. Morrison for their support and guidance as well.

With the help of Po-Hung Yeh, John Reed, Garry Liles, and John Rizutti the experimental setup and data collection went much quicker and smoother than I could have imagined. Thank you for taking time to help me with *my* project.

Also, thank you to Jonathan Leake, a fellow graduate student and long time friend, who helped with various programming questions and obstacles.

Finally, thank you to my wife, Christina, and to my parents: to my parents for continued support throughout my academic career and to Christina for putting up with my late hours and frustration – I am forever thankful for you.

## NOMENCLATURE

$A_{pipe}$	= Area of pipe	cm <sup>2</sup> (ft <sup>2</sup> )
$D_{cutter}$	= Diameter of cutterhead	cm (ft)
$D_{ROI}$	= Diameter of region of influence	cm (ft)
$D_{sp}$	= Diameter of suction pipe	cm (ft)
$d_{50}$	= Median grain size of sediment	mm
$e$	= Unity vector	-
$g$	= Gravitational constant	m/s <sup>2</sup> (ft/s <sup>2</sup> )
$\Gamma$	= Circulation	-
$H$	= Depth of water in tank	cm (ft)
$H_{velocity}$	= Velocity head	ft
$\mu$	= Mean	-
$N_{cutter}$	= Cutterhead rotational speed	RPM
$\nu$	= Kinematic viscosity	m <sup>2</sup> /s (ft <sup>2</sup> /s)
$\omega_{cutter}$	= Rotational velocity of cutterhead	rad/s
$\omega_f$	= Angular velocity of forced vortex	rad/s
$\phi$	= Velocity potential	-
$p$	= Static pressure	PSI
$Q_{suction}$	= Suction flow rate	GPM (ft <sup>3</sup> /s)
$\rho$	= Fluid density	lb <sub>f</sub> /(ft <sup>3</sup> )
$r$	= Radial distance from center of pipe	cm (ft)
$\Omega_f$	= Rotation of cutterhead	rad/s
$\Omega R$	= Circumferential velocity	rad/s
Re	= Reynolds number	-
$\sigma$	= Standard deviation	-
$\theta$	= Flow number	-

$U_{suction}$	= Average suction pipe velocity	cm/s (ft/s)
$V_t / V_{settling}$	= Particle settling velocity	mm/s
$V_{f,vortex}$	= Velocity of forced vortex	cm/s (ft/s)
$V_{sp}$	= Velocity inside suction pipe	cm/s (ft/s)
$x$	= Vertical distance above bottom	cm (ft)
$x_{sp,0}$	= Distance between suction axis and cutter axis	cm (ft)
$X_{sp}$	= Suction pipe axis in x-direction	-
$Y_{sp}$	= Suction pipe axis in y-direction	-
$Z_c$	= Cutterhead axis in z-direction	-

## TABLE OF CONTENTS

	Page
ABSTRACT .....	iii
ACKNOWLEDGEMENTS .....	v
NOMENCLATURE .....	vi
TABLE OF CONTENTS .....	viii
LIST OF FIGURES .....	x
CHAPTER I INTRODUCTION .....	1
Cutter Suction Dredging .....	1
Dredging Process .....	2
Scope of Thesis .....	4
CHAPTER II LITERATURE REVIEW .....	5
Fluid Flow Visualization .....	5
Nature of Flow Around a Cutterhead and Inlet .....	7
Dredge Carriage Design and Modeling .....	8
Computational Model of Flow Around a Freely Rotating Cutterhead .....	9
Spillage and a Mathematical Model of Flow Inside a Cutterhead .....	14
Near-Field Sediment Resuspension Measurement and Modeling .....	17
CHAPTER III EXPERIMENTAL SETUP AND DESIGN .....	19
Tow/Dredge Tank .....	19
Dredge Carriage .....	19
Experimental Setup .....	20
Data Collection Grid Design .....	25
Data Conversion .....	31
CHAPTER IV RESULTS AND DISCUSSION .....	42
Flow Rate Effects .....	42

	Page
Rotation Effects .....	60
Region of Influence .....	71
Comparison to Herbich and Brahme (1986) .....	85
Dimensional Analysis.....	94
CHAPTER V CONCLUSIONS.....	99
REFERENCES.....	103
APPENDIX A QUIVER PLOTS.....	107
VITA .....	143

## LIST OF FIGURES

	Page
Figure 1: Representation of the slit surface behind the blade. $S_1$ is in the streamwise direction and $S_2$ is in the spanwise direction (Dekker et al., 2003). .....	11
Figure 2: Geometry of cutterhead used in experiments and the locations of measurement (Dekker et al., 2003). .....	12
Figure 3: Global coordinate system and suction pipe coordinate system as described by Burger (2003). .....	15
Figure 4: Angle of cutter arm with respect to the global x-axis. ....	22
Figure 5: Side view of experimental setup. ....	22
Figure 6: Front view of experimental setup. ....	23
Figure 7: Apparatus for measurement of velocity field around a swinging cutterhead. ....	24
Figure 8: Theoretical region of influence as described by Glover (2002). ....	26
Figure 9: 7x7x7 three-dimensional data collection grid. (L) Front View. (R) Oblique view. ....	28
Figure 10: 5x5x5 three-dimensional data collection grid. (L) Front view. (R) Oblique view. ....	29
Figure 11: Front view of cutterhead. ....	30
Figure 12: Front view of suction inlet. ....	30
Figure 13: Example of matrix used in data analysis. ....	32

Figure 14: Code snippet from file parsing program. ....	33
Figure 15: Detailed view of ADV mounting setup. ....	34
Figure 16: Comparison of original and despiked data using the method developed by Mori, Suzuki, and Kakuno (2007). (a) $u$ -component of velocity, (b) $v$ -component of velocity, and (c) $w$ -component of velocity.....	36
Figure 17: Velocity vector transformed from ADV axis to cutterhead axis.....	37
Figure 18: Velocity field plotted using a quiver plot.....	40
Figure 19: Velocity field plotted using a color quiver plot. ....	41
Figure 20: Plane location vs. maximum velocity at various x-planes for the no cutterhead scenario. ....	44
Figure 21: Plane location vs. maximum velocity at various x-planes for the cutterhead attached, 0 RPM scenario.....	44
Figure 22: Plane location vs. maximum velocity at various x-planes for the cutterhead attached, 15 RPM scenario. ....	46
Figure 23: Plane location vs. maximum velocity at various x-planes for the cutterhead attached, 30 RPM scenario.....	47
Figure 24: Plane location vs. maximum velocity at various y-planes for the no cutterhead scenario. ....	49
Figure 25: Plane location vs. maximum velocity at various y-planes for the cutterhead attached, 0 RPM scenario.....	50

Figure 26: Plane location vs. maximum velocity at various y-planes for the cutterhead attached, 15 RPM scenario. ....	51
Figure 27: Plane location vs. maximum velocity at various y-planes for the cutterhead attached, 30 RPM scenario.....	52
Figure 28: Plane location vs. maximum velocity at various z-planes for the no cutterhead attached scenario. ....	53
Figure 29: Plane location vs. maximum velocity at various z-planes for the cutterhead attached, 0 RPM scenario.....	53
Figure 30: Plane location vs. maximum velocity at various z-planes for the cutterhead attached, 15 RPM scenario. ....	54
Figure 31: Plane location vs. maximum velocity at various z-planes for the cutterhead attached, 30 RPM scenario.....	54
Figure 32: Plane location (x) vs. maximum velocity for overcutting scenarios...	56
Figure 33: Plane location (x) vs. maximum velocity for undercutting scenarios.	57
Figure 34: Plane location (y) vs. maximum velocity for overcutting scenarios...	58
Figure 35: Plane location (y) vs. maximum velocity for undercutting scenarios.	58
Figure 36: Plane location (z) vs. maximum velocity for overcutting scenarios. ..	59
Figure 37: Plane location (z) vs. maximum velocity for undercutting scenarios.	60
Figure 38: Plane location vs. maximum velocity at various x-planes for the different 200 GPM scenarios. ....	61
Figure 39: Plane location vs. maximum velocity at various x-planes for the different 300 GPM scenarios. ....	63



Figure 40: Plane location vs. maximum velocity at various x-planes for the different 360 GPM scenarios. ....	64
Figure 41: Plane location vs. maximum velocity at various y-planes for the different 200 GPM scenarios. ....	66
Figure 42: Plane location vs. maximum velocity at various y-planes for the different 300 GPM scenarios. ....	66
Figure 43: Plane location vs. maximum velocity at various y-planes for the different 360 GPM scenarios. ....	68
Figure 44: Plane location vs. maximum velocity at various z-planes for the different 200 GPM scenarios. ....	69
Figure 45: Plane location vs. maximum velocity at various z-planes for the different 300 GPM .....	69
Figure 46: Plane location vs. maximum velocity at various z-planes for the different 360 GPM scenarios. ....	70
Figure 47: Points with velocity greater than 1.5 cm/s plotted around the silhouette of a cutterhead. ....	71
Figure 48: Prototype settling velocities for various prototype sediment diameters. ....	73
Figure 49: Prototype settling velocity versus model settling velocity. This allows for easy scaling of settling velocities between prototype and model.	74
Figure 50: Basic geometry of the region of influence. ....	75

Figure 51: Region of influence dimensions when fine sand is the material being picked up. ....	76
Figure 52: Region of influence dimensions when medium sand is the material being picked up. ....	76
Figure 53: Region of influence dimensions when coarse sand is the material being picked up. ....	77
Figure 54: Volume (in ft <sup>3</sup> ) of region of influence for each of the three different grain sizes. ....	80
Figure 55: Region of influence dimensions when coarse sand is the material being picked up and the cutterhead is overcutting.....	82
Figure 56: Region of influence dimensions when coarse sand is the material being picked up and the cutterhead is undercutting. ....	82
Figure 57: Region of influence volume when coarse sand is the material being picked up. ....	83
Figure 58: Region of influence dimensions when very coarse sand is the material being picked up and the cutterhead is overcutting.....	84
Figure 59: Region of influence dimensions when very coarse sand is the material being picked up and the cutterhead is undercutting. ....	84
Figure 60: Region of influence volume when very coarse sand is the material being picked up. ....	85
Figure 61: Results from Herbich and Brahme's paper (1986). The dimensionless velocity field parameter plotted for various values of $r/H$ and $x/h$ . ..	87

Figure 62: The average of $Q/r^2V$ for three different flow rates (200, 300, 360) with no cutterhead attached plotted for various values of $r/H$ and $x/h$ .....	88
Figure 63: The average of $Q/r^2V$ for three different flow rates (200, 300, 360) with cutterhead rotation speed of 0 RPM plotted for various values of $r/H$ and $x/h$ . ....	89
Figure 64: The average of $Q/r^2V$ for three different flow rates (200, 300, 360) with cutterhead rotation speed of 15 RPM plotted for various values of $r/H$ and $x/h$ . ....	89
Figure 65: The average of $Q/r^2V$ for three different flow rates (200, 300, 360) with cutterhead rotation speed of 30 RPM plotted for various values of $r/H$ and $x/h$ . ....	90
Figure 66: The scaled down (to $Q=55$ GPM and $D=1.1$ in) average of $Q/r^2V$ for three different flow rates (200, 300, 360) with no cutterhead attached plotted for various values of $r/H$ and $x/h$ .....	92
Figure 67: The scaled down (to $Q=55$ GPM and $D=1.1$ in) average of $Q/r^2V$ for three different flow rates (200, 300, 360) with cutterhead rotation speed of 0 RPM plotted for various values of $r/H$ and $x/h$ . ....	92
Figure 68: The scaled down (to $Q=55$ GPM and $D=1.1$ in) average of $Q/r^2V$ for three different flow rates (200, 300, 360) with cutterhead rotation speed of 15 RPM plotted for various values of $r/H$ and $x/h$ .....	93

Figure 69: The scaled down (to $Q=55$ GPM and $D=1.1$ in) average of $Q/r^2V$ for three different flow rates (200, 300, 360) with cutterhead rotation speed of 30 RPM plotted for various values of $r/H$ and $x/h$ .....	93
Figure 70: Geometry of the prototype region of influence when the sediment is fine sand. ....	96
Figure 71: Geometry of the prototype region of influence when the sediment is medium sand.....	96
Figure 72: Geometry of the prototype region of influence when the sediment is coarse sand. ....	97
Figure 73: Volume (in $\text{ft}^3$ ) of the prototype region of influence for each of the three different grain sizes.....	98
Figure 74: Quiver plots in the y-z plane for the scenario with no cutterhead attached and 200 GPM. ....	107
Figure 75: Quiver plots in the x-z plane for the scenario with no cutterhead attached and 200 GPM. ....	108
Figure 76: Quiver plots in the y-x plane for the scenario with no cutterhead attached and 200 GPM. ....	109
Figure 77: Quiver plots in the y-z plane for the scenario with no cutterhead attached and 300 GPM. ....	110
Figure 78: Quiver plots in the x-z plane for the scenario with no cutterhead attached and 300 GPM. ....	111

Figure 79: Quiver plots in the y-x plane for the scenario with no cutterhead attached and 300 GPM. ....	112
Figure 80: Quiver plots in the y-z plane for the scenario with no cutterhead attached and 360 GPM.....	113
Figure 81: Quiver plots in the x-z plane for the scenario with no cutterhead attached and 360 GPM.....	114
Figure 82: Quiver plots in the y-x plane for the scenario with no cutterhead attached and 360 GPM.....	115
Figure 83: Quiver plots in the y-z plane for the scenario with cutterhead attached, 200 GPM, and 0 RPM. ....	116
Figure 84: Quiver plots in the x-z plane for the scenario with cutterhead attached, 200 GPM, and 0 RPM. ....	117
Figure 85: Quiver plots in the y-x plane for the scenario with cutterhead attached, 200 GPM, and 0 RPM. ....	118
Figure 86: Quiver plots in the y-z plane for the scenario with cutterhead attached, 300 GPM, and 0 RPM. ....	119
Figure 87: Quiver plots in the x-z plane for the scenario with cutterhead attached, 300 GPM, and 0 RPM. ....	120
Figure 88: Quiver plots in the y-x plane for the scenario with cutterhead attached, 300 GPM, and 0 RPM. ....	121
Figure 89: Quiver plots in the y-z plane for the scenario with cutterhead attached, 360 GPM, and 0 RPM. ....	122

Figure 90: Quiver plots in the x-z plane for the scenario with cutterhead attached, 360 GPM, and 0 RPM. ....	123
Figure 91: Quiver plots in the y-x plane for the scenario with cutterhead attached, 360 GPM, and 0 RPM. ....	124
Figure 92: Quiver plots in the y-z plane for the scenario with cutterhead attached, 200 GPM, and 15 RPM.....	125
Figure 93: Quiver plots in the x-z plane for the scenario with cutterhead attached, 200 GPM, and 15 RPM.....	126
Figure 94: Quiver plots in the y-x plane for the scenario with cutterhead attached, 200 GPM, and 15 RPM.....	127
Figure 95: Quiver plots in the y-z plane for the scenario with cutterhead attached, 200 GPM, and 30 RPM. ....	128
Figure 96: Quiver plots in the x-z plane for the scenario with cutterhead attached, 200 GPM, and 30 RPM. ....	129
Figure 97: Quiver plots in the y-x plane for the scenario with cutterhead attached, 200 GPM, and 30 RPM. ....	130
Figure 98: Quiver plots in the y-z plane for the scenario with cutterhead attached, 300 GPM, and 15 RPM.....	131
Figure 99: Quiver plots in the x-z plane for the scenario with cutterhead attached, 300 GPM, and 15 RPM.....	132
Figure 100: Quiver plots in the y-x plane for the scenario with cutterhead attached, 300 GPM, and 15 RPM.....	133

Figure 101: Quiver plots in the y-z plane for the scenario with cutterhead attached, 300 GPM, and 30 RPM. ....	134
Figure 102: Quiver plots in the x-z plane for the scenario with cutterhead attached, 300 GPM, and 30 RPM. ....	135
Figure 103: Quiver plots in the y-x plane for the scenario with cutterhead attached, 300 GPM, and 30 RPM. ....	136
Figure 104: Quiver plots in the y-z plane for the scenario with cutterhead attached, 360 GPM, and 15 RPM. ....	137
Figure 105: Quiver plots in the x-z plane for the scenario with cutterhead attached, 360 GPM, and 15 RPM. ....	138
Figure 106: Quiver plots in the y-x plane for the scenario with cutterhead attached, 360 GPM, and 15 RPM. ....	139
Figure 107: Quiver plots in the y-z plane for the scenario with cutterhead attached, 360 GPM, and 30 RPM. ....	140
Figure 108: Quiver plots in the x-z plane for the scenario with cutterhead attached, 360 GPM, and 30 RPM. ....	141
Figure 109: Quiver plots in the y-x plane for the scenario with cutterhead attached, 360 GPM, and 30 RPM. ....	142

# CHAPTER I

## INTRODUCTION

### **Cutter Suction Dredging**

Cutter suction dredges are used globally for dredging shallow to medium depth waterways and harbors. In comparison to the more widely used trailing suction hopper dredge, which can dredge in depths in excess of 150 m (492.1 ft), cutter suction dredges dredge at only 35 m (114.8 ft) water depth. However, advancements in technology steadily push dredging depths deeper each year.

The most integral piece of a cutter suction dredge is the cutterhead itself. It is responsible for cutting through the material, ranging from silts and clays to rock. In recent years, new cutterheads have been introduced that are capable of breaking and removing hard rock without the need for blasting, which is both dangerous and harmful to marine life.

A typical cutter head has five or six blades. In some cases cutting teeth or serrated edges are used to aid in the crushing or dislodging of harder materials. The cutter is attached to the ladder arm in front of the suction inlet.

---

This thesis follows the style of the *Journal of Dredging Engineering*.



The ladder arm allows the cutter head to be raised and lowered to different depths depending on the type of sediment being dredged. The cutter head serves two purposes, to cut and dislodge the material and to create a mixture of sediment and water to transport to the surface. Usually, the cutter head will only be partially embedded into the sediment to prevent wear, clogs in the pipe, and to reduce forces on the ladder arm.

The sediment is transported to the surface and to the hopper or placement zone by means of the suction pipe. The suction pipe is placed behind the lower half of the cutterhead and runs along the ladder arm back to the surface. At this point the produced sediment either continues along in the pipe to its final location or is accelerated by a booster pump in cases where the placement zone is far away from the cutting location.

### **Dredging Process**

There are two types of cutter suction dredge: the walking-working spud, in which both spuds are located outside the dredge's stern, and the spud carriage, in which one spud is located in a spud carriage and the other outside the dredge's stern. Spuds are large anchor pilings that are driven into the ground to keep the dredge stationary and advance the vessel forward when needed (Herbich, 2000). In both cases the dredge swings from side to side using one spud as a pivot. Two cables attached to either side of the ladder arm control the rate of swing. In

order to move forward after the first initial cut has been made, the digging spud must be raised and the walking spud lowered into the ground. This will advance the dredge and production can begin with the continuation of the swing. It has been shown that the spud carriage arrangement is superior to the walking-working spud, improving the efficiency from 50 to 75% (Turner, 1984).

Depending on which way the dredge is swinging, the cutterhead will be either under-cutting or over-cutting. Over-cutting occurs when the cutterhead is rotating in the same direction that the dredge is moving. This causes the sediment to be drawn in towards the suction inlet that is located near the bottom of the cutterhead. Under-cutting occurs when the cutterhead is rotating in the opposite direction to the movement of the dredge. In this situation the material is pulled away from the suction mouth by the blades. In both cases it is important to know the size of the region of influence created by the cutterhead rotation and suction. The region of influence determines to what extent the sediment that has been placed into suspension around the cutterhead will be pulled into the suction intake. More precisely, the region of influence is defined as the volume surrounding the cutterhead in which the velocity field created by the cutterhead is greater than the settling velocity of the sediment that is being dredged. Factors affecting the region of influence are flow rate, cutterhead rotation speed, swing speed, and swing direction. Determining the most efficient

operating condition for each of these will lead to an increase in region of influence and therefore an increase in production.

### **Scope of Thesis**

The flow field in the vicinity of the inlet mouth of a cutterhead suction dredge is very complex in nature. The complexity is caused by the interaction between the suction flow, rotating cutterhead blades, and swinging of the ladder. Studies have been conducted in the past that measured the magnitudes of the velocities in two dimensions in a limited number of scenarios, mostly with a stationary cutterhead or no cutterhead at all (Brahme and Herbich, 1986). These past studies serve as a basis for this thesis. An investigation of greater breadth is needed to better understand the nature of the flow field. Using acoustic Doppler velocimeters (ADV), a more accurate visualization of the velocity field can be created and used to determine the region of influence around the cutterhead. Similitude will be used to determine any relationships between dredge parameters suction intake diameter, suction flow rate, and cutterhead rotation speed.

This is useful to the dredging community for two reasons: first, knowing the region of influence around the cutterhead helps the dredger achieve higher production by using a more efficient cutting depth and two, achieving similitude with the velocity flow field - allows for more accurate model testing in the future.

## CHAPTER II

### LITERATURE REVIEW

Several studies have been completed pertaining to the measurement and modeling of the flow field around a cutter suction head dredge. In order to develop the most accurate model, it will be useful to look back at previous research for guidance.

#### **Fluid Flow Visualization**

Slotta (1968) describes the experimental visualization of fluid flow around a cutterhead. Bubbles created by electrolysis were used to visualize the flow of water in and around a cutterhead during different testing scenarios. The goal was to determine how operating conditions affected both the turbidity and sediment production.

The research assumed that similitude could be achieved for the Reynolds number, Froude number, kinematic scale of velocities, and the specific speed of the rotating cutterhead (Slotta, 1968). The criteria for each are:

$$\text{Reynolds: } \left[ \frac{U_{suction} D_{cutter}}{\nu} \right]_{\text{model}} = \left[ \frac{U_{suction} D_{cutter}}{\nu} \right]_{\text{prototype}} \quad (1)$$

$$\text{Froude:} \quad \left[ \frac{(U_{suction})^2}{gD_{cutter}} \right]_{\text{model}} = \left[ \frac{(U_{suction})^2}{gD_{cutter}} \right]_{\text{prototype}} \quad (2)$$

$$\text{Kinematic:} \quad \left[ \frac{\omega_{cutter} D_{cutter}}{U_{suction}} \right]_{\text{model}} = \left[ \frac{\omega_{cutter} D_{cutter}}{U_{suction}} \right]_{\text{prototype}} \quad (3)$$

$$\text{Specific speed:} \quad \left[ \frac{\omega_{cutter} \sqrt{Q_{suction}}}{(H_{velocity})^{3/4}} \right]_{\text{model}} = \left[ \frac{\omega_{cutter} \sqrt{Q_{suction}}}{(H_{velocity})^{3/4}} \right]_{\text{prototype}} \quad (4)$$

$$\text{where: } H_{velocity} = \frac{(U_{suction})^2}{2g}.$$

The similitude criteria were determined by dimensional analysis on the cutterhead and suction pipe parameters. Slotta (1968) found that satisfying similitude for the Reynolds and Froude number together was physically impossible. However, equations (3) and (4) accurately correlated the data for suction velocity, cutterhead speed, and volumetric flow rate (Glover 2002).

Since similitude could not be found across all four parameters it was determined that it was not possible to project results from model tests at the time, except on a qualitative basis. Dimensional analysis could provide a basis and guide but came with inherent difficulties (Slotta 1968).

## **Nature of Flow Around a Cutterhead and Inlet**

Brahme and Herbich(1986) published the results of their research of the nature of flow around a cutterhead and inlet, and investigated how inlet flow affected turbidity. The goal was to determine ways to reduce turbidity in the vicinity of the cutterhead and avoid resuspension of potential pollutants in the sediment (Brahme and Herbich 1986).

In contrast to work previously done by Slotta (1968), Brahme and Herbich (1986) wanted to measure the flow field both qualitatively and quantitatively. This was important since the velocity field around the cutterhead determines the amount of suspended sediment that is picked up by suction. A new parameter measuring the radial distance between the suction tube and suspended sediment,  $R_1$ , was studied by Brahme (1983). This new parameter was useful in determining the area of influence of the cutterhead suction.

Based on their research, Brahme and Herbich (1986) made the following general observations:

1. Velocity increased as the flow rate through the suction pipe increased.
2. Velocity was highest near the suction pipe but decreased rapidly away from the pipe.
3. The region of highest velocity was always near the suction pipe.
4. A change in pipe diameter did not affect the velocity field.

A dimensionless parameter,  $Q/r^2V$  where  $Q$  is the suction flow rate,  $r$  is the radial distance to the center of the suction inlet, and  $V$  is the velocity any point, was developed that made it possible to reasonably estimate the velocity field if the volumetric flow rate and radial distance from the suction inlet are known. By plotting this dimensionless parameter for different values of  $x/h$  and  $r/H$ , where  $x$  is the distance from the bottom,  $r$  is the radial distance,  $h$  is the distance from the suction pipe to the sediment, and  $H$  is the water depth, the velocity field at the intake can be determined. This was important since it was found that the velocity field did not depend on the intake velocity or intake diameter if the volumetric flow rate remained constant. Rather, it only depends on the flow rate through the suction pipe (Brahme and Herbich, 1986).

### **Dredge Carriage Design and Modeling**

Glover (2002) conducted research on dredge carriage design and laboratory modeling of hydraulic dredges. Three sets of scaling laws were examined. One scaling parameter was based on sediment pick-up behavior, the second was based on similarity with respect to the Froude number, and the third was based on similarity with respect to cavitation during the cutting process.

Since solid-fluid interaction is so complex in nature, it has been difficult to develop model-prototype similitude. Glover believed that being able to relate quantities such as suction flow rate, swing speed, cutterhead RPM, bank height,

and depth of cut to sediment production would require a working hydraulic model (Glover 2002). Two different ways of scaling the flow through the suction were used:

$$(Q_{suction})_{model} = (Q_{suction})_{prototype} \left[ \frac{(D_{cutter})_{model}}{(D_{cutter})_{prototype}} \right]^2 \left[ \frac{(V_{settling})_{model}}{(V_{settling})_{prototype}} \right] \quad (5)$$

$$(Q_{suction})_{model} = (Q_{suction})_{prototype} \left[ \frac{(D_{cutter})_{model}}{(D_{cutter})_{prototype}} \right]^2 \quad (6)$$

All three scaling laws (hydraulic, kinematic, and dynamic) cannot be achieved with one set of modeling parameters. Glover (2002) found theoretically that kinematic similarity exists for the velocity fields created by the suction inlet, cutterhead rotation, and swing speed. Further, there is a strong suggestion that for an accurate hydraulic model to exist the model suction must be scaled such that the sediment pick-up behavior is similar to that of the prototype (Glover 2002). This means that the ratio of the velocity field geometry to the cutterhead diameter must be the same for both the model and prototype and the ratio of the velocity field magnitude to particle settling velocity must also be the same for both the model and prototype dredges.

### **Computational Model of Flow Around a Freely Rotating Cutterhead**

Dekker et al. (2003) used numerical and experimental models to examine the complex flow inside a freely rotating cutterhead in order to better understand how the sediment and water mixture in an actual dredging environment behaves



inside the cutterhead. A simplified model, considering only water, was used so the multiphase nature of the flow was not yet taken into account. Due to a variety of factors such as soil type, angular velocity of the cutterhead, flow rate into the pipe, and cutterhead geometry the amount of production can vary (Dekker et al., 2003).

An experiment and computational fluid dynamics model (CFD) were setup to investigate and compare the velocity and pressure fields inside and along the blades of the cutterhead. Two model parameters important for the characterization of different flows used in these experiments were the flow number,  $\theta$ , and Reynolds number,  $Re$ :

$$\theta = \frac{Q}{\Omega R^3} \quad Re = \frac{\Omega R^2}{\nu} \quad (7)$$

In setting up the CFD analysis the potential flow model was used because of its relative simplicity. In comparison with other flow models based on Reynolds-averaged Navier Stokes equations with empirical closure for turbulent stresses, the computation times are modest (Pope, 2000). Since the Reynolds number is large in almost all cases regarding dredging, the flow entering the cutterhead can be assumed to be irrotational with no large boundary layer separation (Dekker et al., 2003). The governing Laplace equation for the velocity potential,  $\phi$ , is

$$\nabla^2 \phi = 0 \quad (8)$$

Assuming incompressible, inviscid, and irrotational flows, the Navier Stokes equations can be simplified to:

$$\frac{d\phi}{dt} + \frac{p}{\rho} + \frac{1}{2} \bar{v} \cdot \bar{v} + gz = \text{constant} \quad (9)$$

where  $\frac{d\phi}{dt}$  is the derivative of the potential,  $\phi$ , with respect to time,  $t$ ;  $p$  is the static pressure;  $\rho$  is the fluid density;  $g$  is the acceleration due to gravity;  $v$  is the velocity; and  $z$  is the coordinate indicating elevation.

On the surface of each cutterhead blade there will be circulation,  $\Gamma$ , as each water particle leaves the trailing edge (Batchelor, 1967). To model this circulation slit surfaces are used as shown in Figure 1. Knowing the behavior of the particle trajectories on the cutterhead blades is important for further investigations of their relationship to the flow field in the area surrounding the cutterhead.

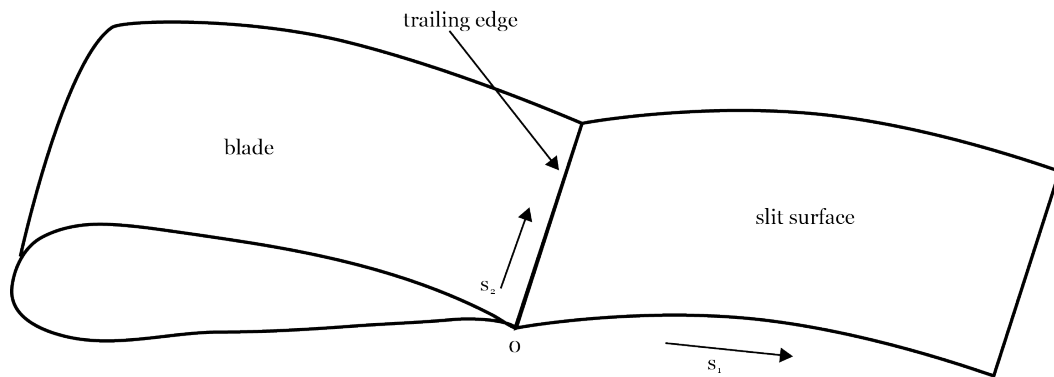


Figure 1: Representation of the slit surface behind the blade.  $S_1$  is in the streamwise direction and  $S_2$  is in the spanwise direction (Dekker et al., 2003).

The experimental study was performed at the Laboratory of Dredging Technology at the Delft University of Technology. An aluminum cutterhead with an outer radius of 0.35 m was used; this is very similar to the cutterhead used at the Haynes Coastal Engineering Laboratory. The cutterhead blades are attached to a cutterhead ring and inside that ring the blades are also attached to a conical plate as seen in Figure 2 (Dekker et al., 2003).

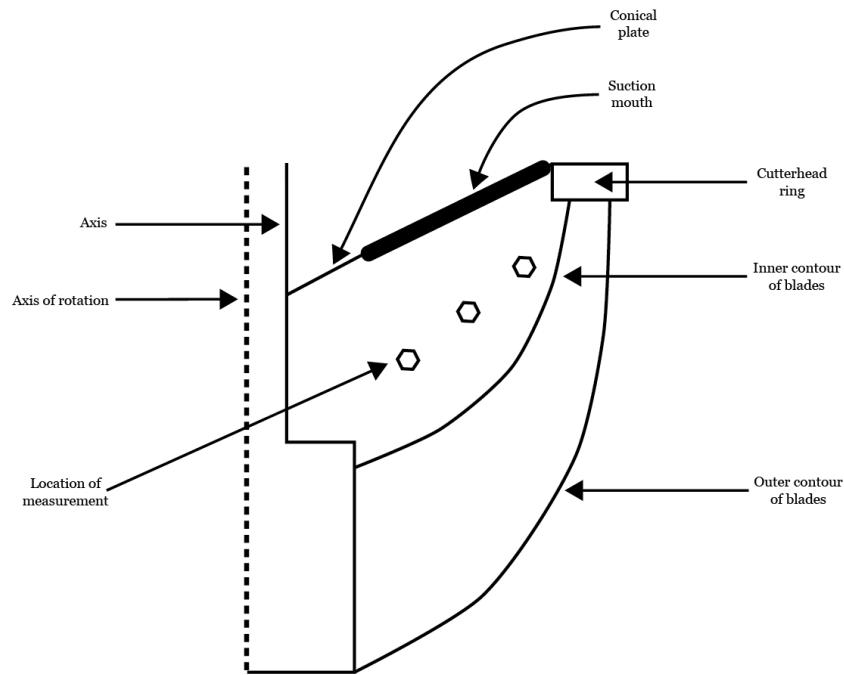


Figure 2: Geometry of cutterhead used in experiments and the locations of measurement (Dekker et al., 2003).

In all of the tests that were run the flow was turbulent ( $N_R = 2.6 \times 10^5 - 14.8 \times 10^5$ ). The flow field was measured at 12 points inside of the cutterhead using Nortek acoustic Doppler velocimeters as shown in the geometry of cutterhead above

(Figure 2). The ADVs were stationary and recorded the three velocity components at 25 Hz.

Their results showed a comparison between their measured and computed velocity vectors inside of the cutterhead. In both cases, the radial and circumferential velocities were nondimensionalized, the circumferential velocity by  $\Omega R$  and the axial velocity by  $Q/A_{\text{pipe}}$  (Dekker et al., 2003). The velocities were nondimensionalized so that the two models, both experimental and numerical, could be easily compared on both a quantitative and qualitative level. The axial velocities were generally small, except for the points lying in front of the suction inlet. The CFD analysis showed the same behavior, however the magnitudes were approximately 50% of the experimentally collected velocities. As the flow number is increased, it is clear that suction flow has a direct impact on the velocities as indicated by the velocity vectors directed in the opposite direction of the rotation (Dekker et al., 2003). Solutions to the governing Laplace equation (8) were determined using the numerical method of Kruyt et al. (1999), which is based on the three-dimensional finite element method and uses superelement techniques and implicit Kutta-Joukowski conditions. Their findings reinforce the assumption that the highest velocities around the cutterhead occur in the region closest to the suction mouth.

As with any flow model there were limitations, mostly dealing with computational resources. Selecting a proper model that takes into account all of the viscous and rotational effects is a very difficult task and even then, choosing a reasonable mesh size and quality can greatly affect the outcome of the model (Dekker et al., 2003).

The scope of this thesis is only experimental, however, eventually a CFD analysis of the flow field surrounding the cutterhead should be done to verify the experimentally determined values.

### **Spillage and a Mathematical Model of Flow Inside a Cutterhead**

Burger's (2003) focused on the process and cause of spillage and how it could be minimized. Models were set up both experimentally and mathematically in order to determine the trajectory of a single particle inside of the cutterhead.

In order to simulate a single particle inside of the cutterhead the dimensionless Navier-Stokes equations and dimensionless equations of motion were used. The flow inside of the cutterhead is very complex due to the turbulence caused by the rotation of the cutterhead and the flow from the suction. These two factors, along with the two-phase flow that occurs when sediment is introduced, make this simulation a very difficult task. Instead of initially using a CFD model to predict the particle trajectory Burger (2003) used a much simpler model to help

understand the basic physics behind the particle motion. He proposed that with this knowledge others would be able to build on his findings in the future.

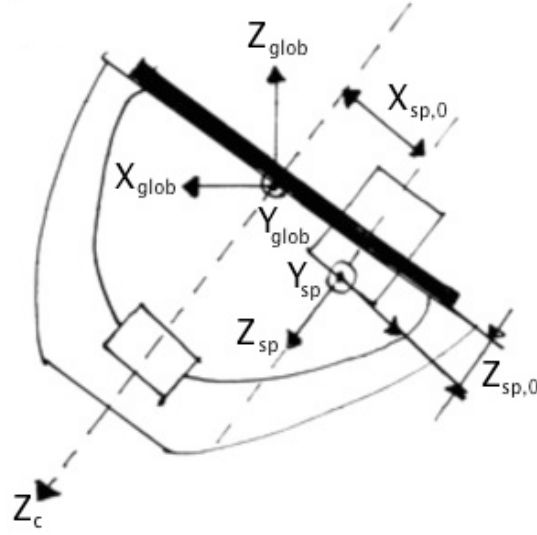


Figure 3: Global coordinate system and suction pipe coordinate system as described by Burger (2003).

The model for the rotating cutterhead with suction used the superposition of a forced vortex (neglecting turbulence) onto a three-dimensional sink. The equation for the velocities inside of the cutterhead due to the rotation of the cutterhead, in the coordinate system of the suction pipe, is:

$$\vec{v}_{f,vortex} = \omega_f \left( (x_{sp} + x_{sp,0}) \vec{e}_{Y,sp} - Y_{sp} \vec{e}_{X,sp} \right) \quad (10)$$

where  $\vec{v}_{f,vortex} = \vec{\Omega}_f \times \vec{r}$  and  $\vec{r} = (X_{sp} + X_{sp,0}) \vec{e}_{x,sp} + Y_{sp} \vec{e}_{Y,sp}$  (Burger, 2003).  $\vec{\Omega}_f$  is the vector for the rotation of the cutterhead about the cutter axis ( $Z_c$ ) and is given by:

$$\vec{\Omega} = \vec{e}_{Z_c} \omega_c \quad (11)$$

where  $\bar{e}_{Z_c}$  is the unity vector in the direction of  $Z_c$  and  $\omega_c$  is the angular velocity of the cutter head. Since a forced vortex is not irrotational it does not satisfy the potential flow theory.

Burger derived the water velocities inside of the cutter head due to the suction flow from the continuity equation (Burger, 1998). The equation is:

$$v_{f,suction} = -\frac{Q_s}{2\pi R^2} \bar{e}_R = -\frac{1}{8} \left( \frac{D_{sp}}{R} \right)^2 v_m \bar{e}_R \quad (12)$$

where  $D_{sp}$  is the diameter of the suction pipe and  $v_m$  is the water velocity inside of the suction pipe:

$$\bar{R} = X_{sp} \bar{e}_{X,sp} + Y_{sp} \bar{e}_{Y,sp} + Z_{sp} \bar{e}_{Z,sp} \quad (13)$$

$$\bar{e}_R = \frac{X_{sp}}{R} \bar{e}_{X,sp} + \frac{Y_{sp}}{R} \bar{e}_{Y,sp} + \frac{Z_{sp}}{R} \bar{e}_{Z,sp} \quad (14)$$

Superimposing the velocity vectors for the rotation of the cutterhead and suction flow lead to the following velocity components in the  $X_{sp}$ ,  $Y_{sp}$ , and  $Z_{sp}$  directions:

$$v_{f,X_{sp}} = -\frac{1}{8} \left( \frac{D_{sp}}{R} \right)^2 v_m \frac{X_{sp}}{R} - \omega_f Y_{sp} \quad (15)$$

$$v_{f,Y_{sp}} = -\frac{1}{8} \left( \frac{D_{sp}}{R} \right)^2 v_m \frac{Y_{sp}}{R} + \omega_f (X_{sp} + X_{sp,0}) \quad (16)$$

$$v_{f,Z_{sp}} = -\frac{1}{8} \left( \frac{D_{sp}}{R} \right)^2 v_m \frac{Z_{sp}}{R} \quad (17)$$

Based on the above equations the flow inside of the cutterhead can be determined. After conducting numerous simulations using the above equations

for the flow field and the equations of motion for the forces on the particle, it was concluded that particles are entrained if the particles are released very near to the suction pipe. Regarding the effect of the rotational speed of the cutterhead on the particle trajectory, he found that as the rotational speed was increased there was always a negative impact on particle that meant the particle did not get entrained and was thrown away from the cutterhead.

The model that was used to determine the trajectory of single particle inside of the cutterhead could be extended to simulate the flow field around the outside of the cutterhead as well. This could be done by superimposing a free vortex (rather than a forced vortex) onto a sink. Burger (2003) found that the model was too simplistic to determine the actual trajectories of particles inside of the cutterhead because it left out the pump effect due to the cutterhead. It is unlikely that this problem would occur when modeling the flow outside of the cutterhead since the pump effect is not present there.

### **Near-Field Sediment Resuspension Measurement and Modeling**

Henriksen (2009) examined turbidity generation in a laboratory setting by using resuspension data collected at the Haynes Coastal Engineering Laboratory at Texas A&M University. In addition, a near-field advection diffusion model that incorporated the experimental data into it was created to predict sediment resuspension.



Henriksen found that undercutting caused more spatial turbidity than overcutting in each different scenario despite varying the suction flow rate, cutterhead speed, and thickness of the cut (Henriksen, 2009). Generally, it was shown that increasing the suction flow rate increased production and decreased turbidity (Henriksen, 2009). Also, increasing the cutterhead speed increased the turbidity in most scenarios that Henriksen tested, however, increasing the cutterhead speed also resulted in a higher turbulent diffusion rate (2009). Turbulence characteristics were investigated using both turbidity and velocity data collected during experimentation which made it possible to determine the diffusion field for each different scenario (Henriksen, 2009).

There is still work to be done on the topic of flow visualization and analysis around and through a cutter suction head dredge inlet. Both Slotta (1968) and Brahme and Herbich (1986) were able to visualize the flow field in two dimensions but their methods could be improved with modern instrumentation. Burger (2003) and Dekker et al. (2003) investigated the flow field in three dimensions, however, their focus was on the flow inside of the cutterhead. A three dimensional model outside of the cutterhead is useful in physically interpreting the flow field and how it relates to other dredging parameters.

## **CHAPTER III**

### **EXPERIMENTAL SETUP AND DESIGN**

#### **Tow/Dredge Tank**

The Haynes Coastal Engineering Laboratory has a three-dimensional shallow water wave basin and a two-dimensional tow/dredge tank. A dredge carriage was designed, built, and installed in 2006 to facilitate experiments and testing of various dredging techniques.

The tow-dredge tank is 45.7 m (149.90 ft) long, 3.05 m (10.01 ft) deep, and 3.70 m (12.10 ft) wide. In addition, a sediment pit is located near the west end of the tank that is 7.6 m (24.93 ft) long and 1.7 m (5.58 ft) deep. There are six observation windows, three located on the north side of the tank in the center and three in the sediment pit. Both the shallow water wave basin and tow/dredge tank are capable of having 35,000 GPM (2.208 m<sup>3</sup>/s) of water current pumped through the tanks using four axial flow pumps. In the tow/dredge tank, the water enters the tank through a diffuser located at the west end of the tank.

#### **Dredge Carriage**

The dredge carriage was conceptually designed by Glover (2002). In 2004, Glover and Randall finalized the design and construction and installation began.

The dredge carriage was delivered to the Haynes Coastal Engineering Laboratory in April 2005. Construction and installation were completed by Oilfield Electric Marine Inc. (OEM) and Digital Automation Control Systems (DACS) in 2007 (Henriksen, 2009). In 2007, the dredge carriage was christened the “B. G. Hindes” in honor of the donor of initial funds to begin construction.

The dredge carriage consists of the ladder cradle, upper and lower ladder, articulating arm, and cutter head. Movement of the carriage is restricted to the east and west directions along two guide rails. Measuring devices that were built into the carriage include: a flow meter, a nuclear density gauge, a horizontal location laser, pressure, and force sensors. The flow meter and density gauge can be used to accurately predict the production during dredging tests (Glover 2002).

The dredge carriage is a 1:6 scale of a 0.609 m (2 ft) prototype cutter suction head dredge which means that the suction inlet is 0.102 m (0.33 ft) and discharge outlet is 0.076 m (0.25 ft).

### **Experimental Setup**

The experiment and data collection took place in the sediment pit located in the tow/dredge tank. Since the ladder can only be raised a maximum of 0.91 m (3 ft) above the tow/dredge tank floor it was necessary to use the sediment pit so that

the ladder would have a wider range of vertical motion, making it possible to collect more data points without any unintended boundary interference.

The cutterhead was initially placed at a  $30^\circ$  cutting angle as seen in Figure 4. Cutting angles are typically between  $20^\circ$  and  $30^\circ$  in most dredging scenarios. Three Nortek Vectorino acoustic Doppler velocimeters (ADV) were positioned .61 m (2 ft) away. The ADVs are high-resolution acoustic Doppler velocimeters that measure water velocity in three dimensions with an accuracy of 1% of the measured velocity (Nortek, 2009). Velocity measurements were taken at a sampling rate of 25 Hz and a sampling volume of .25 cm<sup>3</sup>. The ADVs can be positioned either vertically or horizontally. In this case, the ADVs were mounted facing horizontally inward towards the cutterhead. The ADVs were spaced 3D (three suction inlet diameters) apart in the vertical direction. The reasoning for the 3D spacing is explained further in the Data Collection Grid Design section.



Figure 4: Angle of cutter arm with respect to the global x-axis.

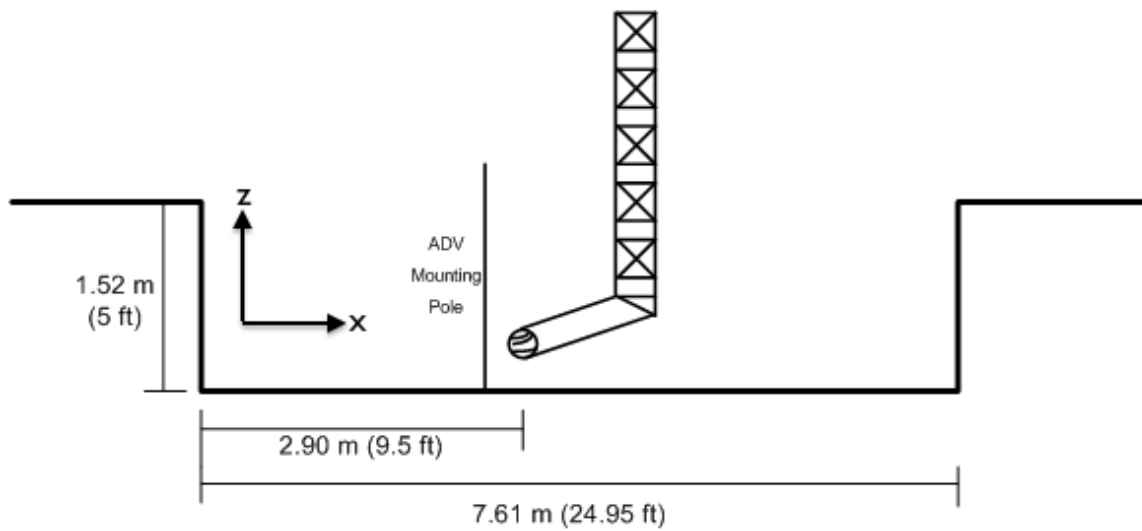


Figure 5: Side view of experimental setup.

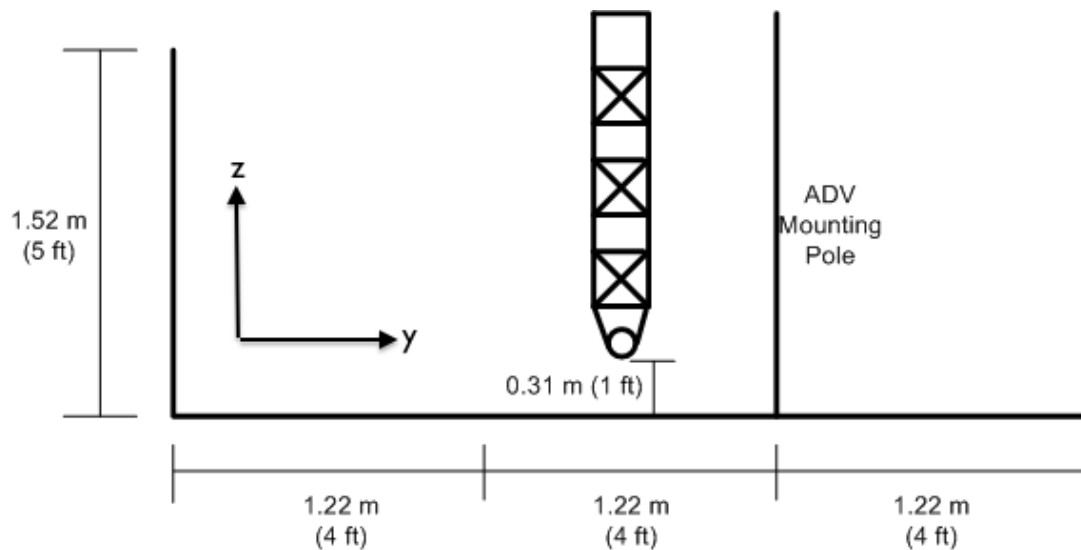


Figure 6: Front view of experimental setup.

For scenarios that involved swing speed the setup was slightly different. The spacing of the measurements was still 3D, however, the ADVs were affixed to the ladder as shown in Figure 7. This made it possible to measure the velocity around the cutterhead without the possibility of a collision between the cutter and an ADV. Points within approximately 3D of the tip of the cutterhead and below the cutterhead were not measured due to precautions related to damage of the ADV and the structural limits of the measuring apparatus, respectively. Since the ADVs were affixed to the ladder they had to be manually moved after each test. This was done by draining the tow-dredge tank, moving each ADV, and then refilling the tank.

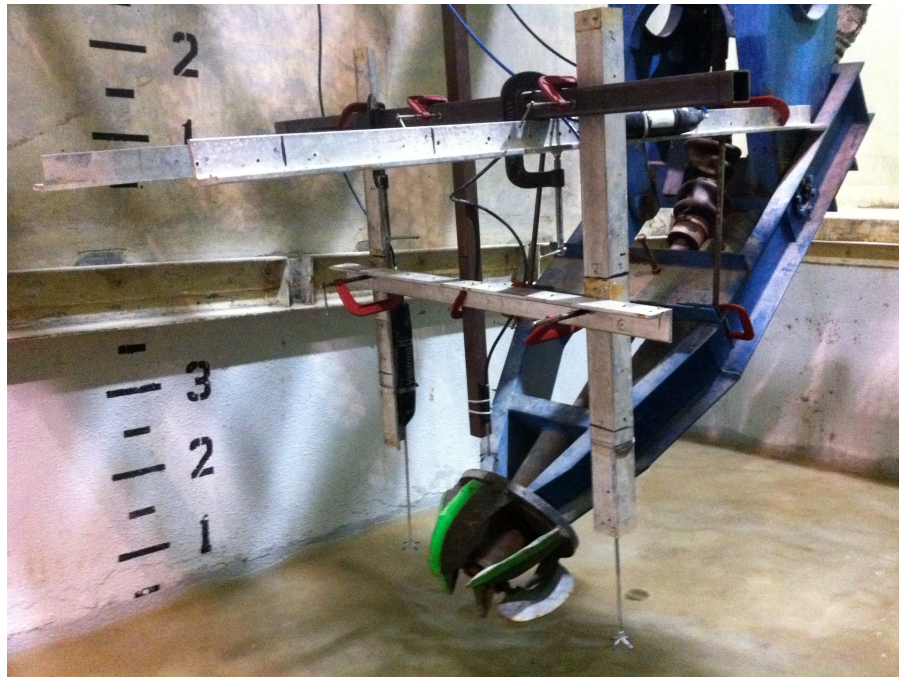


Figure 7: Apparatus for measurement of velocity field around a swinging cutterhead.

When determining the correct grid and spacing of data points to be collected there are multiple factors that must be addressed. The first is data collection resolution. Since one of the objectives of this thesis is to determine the region of influence of the cutterhead suction, the grid of data collected must be able to clearly show where this boundary occurs. As the distance increases in the x-direction away from the cutterhead the effect of the suction and cutterhead rotation will decrease so it was necessary that the ADVs be able to detect the point where the velocity field from the cutterhead equaled that of the particle settling velocity. Ideally, many weeks would have been spent collecting data in the finest grid possible; however, a balance had to be struck between resolution and time.

The second factor is the ability of the dredge carriage to be moved small distances. The dredge carriage can be moved either manually with a joystick or by inputting coordinates into its control system. Both options were tested to determine which method allowed for quicker data collection. Since the dredge carriage is controlled by servomotors and digital variable frequency drives it should have the ability to be moved on the order of 12.5 cm (1 in.) increments (Young 2009). In practice, however, there was variation on the order of 2-10 cm in both the x and y directions. When compared to the grid spacing, this type of error could not be overlooked so for each movement of the cutterhead additional time was spent correcting to the right position. For the most part, the dredge carriage overshot its inputted coordinates. This problem could be solved by a few different methods: an analysis of the average overshoot distance could be conducted then incorporated into the digital logic controller or some type of braking mechanism could be attached to each motor to allow for more accurate stopping.

### **Data Collection Grid Design**

Considering these factors, two main grids were designed with variations on each also considered. The diameter (D) of the suction inlet was used as the basis for the spacing between each data point to be collected. This is a customary length scale used in the design and analysis of various dredging parameters.



In order to form a preliminary region of influence, conservation of mass was used. Based on the cross sectional area of the cutterhead intake,  $0.008107 \text{ m}^2$  ( $0.0873 \text{ ft}^2$ ), and a flow rate of  $0.025 \text{ m}^3/\text{s}$  (400 GPM) the preliminary boundary will have a diameter of  $1.016 \text{ m}$  ( $3.33 \text{ ft}$ ). This was determined under the conservative assumption that the velocity near the boundary of the region of influence would be 1% of the intake velocity. Both Glover (2002) and Burger (2003) investigated the velocity field around the inlet. Burger (2003) focused mainly on the behavior of the velocity field inside the cutter head and Glover (2002) only in a qualitative sense.

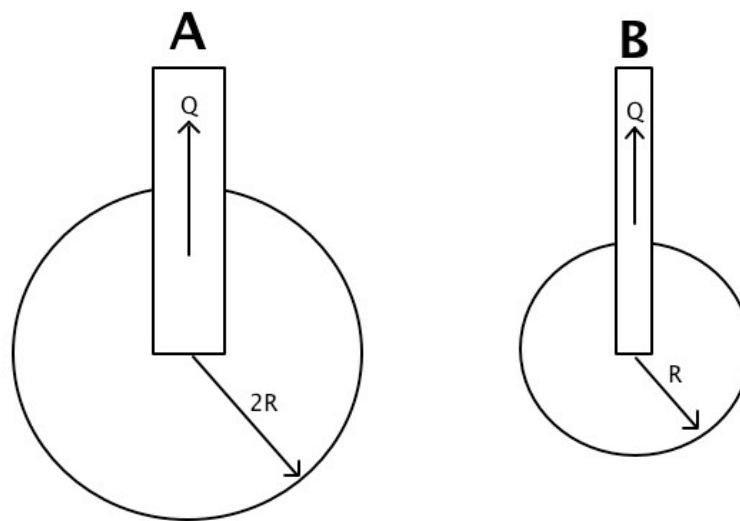


Figure 8: Theoretical region of influence as described by Glover (2002).

The focus was on similitude between model and prototype dredges. With respect to the velocity field, he compared two theoretical suction pipes that were geometrically similar at a 1:2 geometric scale ratio. In Figure 8, Q is the suction

into the pipe, the circular lines are lines of constant velocity potential, and  $R$  is the distance at which the suction velocity ( $V$ ) equals the settling velocity of the sediment. For the two suction pipes to be geometrically similar the range of pipe A must be twice that of pipe B (Glover, 2002). Since the diameter of the suction pipe on the 'B.G. Hindes' dredge carriage is constant throughout each scenario the important part of Glover's observations are his conclusions about the shape and relationship between the velocity field and particle settling velocity. For a given particle size, the range,  $R$ , increases with a higher velocity and decrease with weaker velocity fields (Glover, 2002). In relation to this thesis, this is important because it provides an initial hypothesis for the behavior of the velocity field when different parameters are varied. It is expected that the scenarios where no cutterhead is attached that the velocity field will look and behave very similar to what Glover describes. Once the cutterhead is attached, though, it is possible that the velocity field will be distorted in some way and may not behave as would be expected with a simple pipe with suction.

Two different grid designs were considered for use in data collection, a  $7 \times 7 \times 7$  grid and a  $5 \times 5 \times 5$  grid, shown in Figures 9 and 10, respectively. After performing a short run through of both, it was evident that both designs had desirable qualities - the  $7 \times 7 \times 7$  grid for its fine mesh and the  $5 \times 5 \times 5$  grid for its quick completion time. The final grid design is a hybrid of the two previously described. Once setup for the experiment began, it was clear that the  $7 \times 7 \times 7$  grid

was not only too large (particularly the amount of  $7 \times 7$  vertical grids), but also the area 3D and 6D behind the cutterhead would not be affected by the suction or the cutterhead rotation. Taking this into account, each plane behind the cutterhead was removed from the design, which left only the planes even with and in front of the cutterhead. Based on the simple calculations above it was assumed that only three planes would need to be measured in front of the cutterhead. The grid design differs depending on whether or not the cutter is attached. For the cases when cutter is not attached, a  $3 \times 5 \times 5$  grid was used as a basis for data collection. Once the cutter is attached, a  $1 \times 8 \times 5$  grid was used for the two planes nearest to the cutter and a  $2 \times 14 \times 5$  grid was used for the plane farthest away from the cutter. By increasing the fineness of the grid, a more detailed view of the region of influence was available.

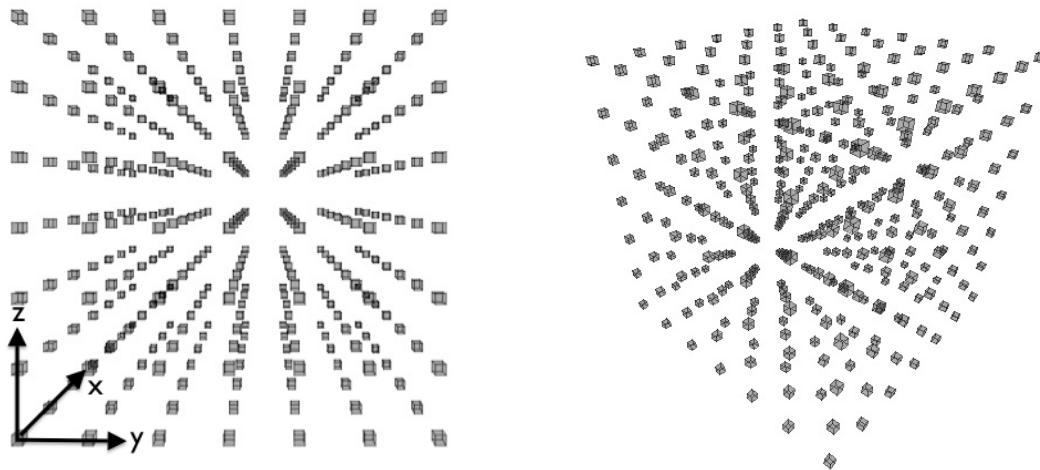


Figure 9:  $7 \times 7 \times 7$  three-dimensional data collection grid. (L) Front View. (R) Oblique view.

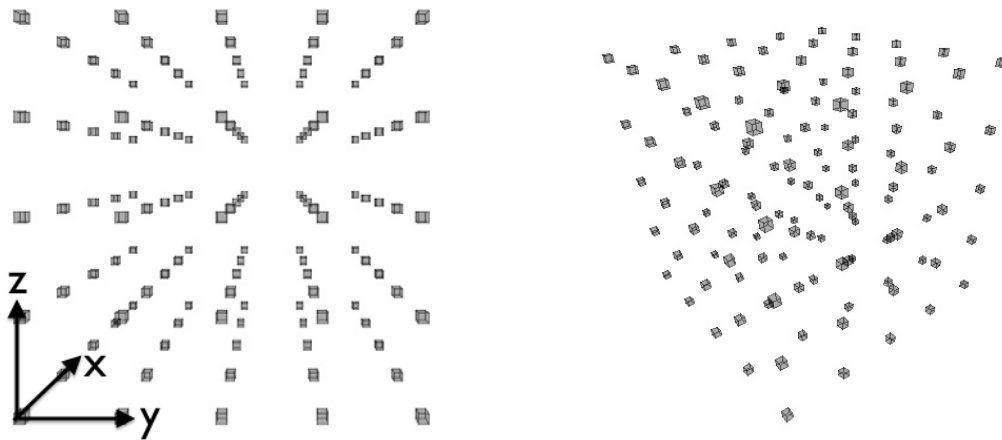


Figure 10: 5x5x5 three-dimensional data collection grid. (L) Front view. (R) Oblique view.

For both designs, data were collected with the cutterhead both attached and detached, at different flow rates, at different cutterhead rotation speeds (when the cutter head is attached), and swing speeds. The first test was conducted with the cutter head removed so that there was nothing obstructing the 0.102 m diameter intake. Testing without the cutter head allowed for a baseline performance to be determined as well as a comparison to past data collected by Herbich and Brahme (1986). The flow rates that were tested were 200 GPM, 300 GPM, and 360 GPM. At each flow rate, data was collected at all points in each grid. Next, the cutter head was attached and flow rates were varied again. The cutter head is shown below. With the cutter head attached, however, at each flow rate the cutter head rotation was varied between 0 RPM, 15 RPM, and 30 RPMs. 0 RPMs provides a visualization of how the cutterhead itself affects the flow field and a base for what the flow field should look like once it begins rotating. Finally, the ladder was moved in the North and South directions at 4 cm/s and 8 cm/s in

order to simulate the swinging movement during dredging. Measurements were taken as it moved each way so that both overcutting and undercutting data could be collected. In total, fourteen scenarios were completed.



Figure 11: Front view of cutterhead.



Figure 12: Front view of suction inlet.

Table 1: Data Collection Scenarios

	Flow rate, Q (GPM)	Cutter head speed, N (RPM)	Swing Speed (cm/s)
<b>No cutter head</b>	200		
	300		
	360		
<b>With cutter head</b>	200	0	
		15	
		30	
	300	0	
		15	
		30	
	360	0	
		15	
		30	
<b>Ladder undercutting</b>	360	15	4
		30	
<b>Ladder overcutting</b>		15	8
		30	

### Data Conversion

The data collected at each point throughout experimentation was stored in a proprietary, .vno, file format. The .vno file format is used for unconverted Nortek Polysync files and can only be converted to a useful format using the data conversion tool within Polysync. Once converted, the file extension is changed to .vel.txt which contains all of the metadata relating to data collection as well as the velocities in the  $u$ ,  $v$ , and  $w$  directions over the entire interval of measurement.

Since a new file was created every time data was collected, there were 800 files each containing data at two or three different data points. This was not useful for

two reasons: separate data points are essentially meaningless in the context of this thesis since the overall behavior of the velocity field is being examined and combining them all into a useful format would not be a trivial task. To determine if the data collected was suitable for further analysis a small number of sampling points, from the first scenario with no cutterhead attached and flow rate of 200 GPM, were taken and the velocity field was plotted. The results were satisfactory and a more efficient method for analyzing and plotting the data was created.

It was determined that the most efficient way to analyze each scenario was to combine all data points into a large matrix, shown in Figure 13, containing the description of each (cutter/no cutter, flow rate, cutterhead speed, location) and the velocities. Using Matlab it would then be much simpler to sort through the data by each attribute and group sets of data points into their respective testing scenarios.

Cutter/No Cutter	Flow Rate (GPM)	Cutterhead Rotation (RPM)	Plane	x (cm)	y (cm)	z (cm)	u (cm/s)	v (cm/s)	w (cm/s)
:	:	:	:	:	:	:	:	:	:

Figure 13: Example of matrix used in data analysis.

A program was written to accomplish this task. Since a consistent naming convention was used throughout the data collection process, it was possible to parse the relevant data from the file name and use when filling in the various columns of the master matrix. A small portion of the code that was used for this is shown in Figure 14.

```

for i = 1 : length(struct_data)
    s = struct_data(i);
    for j = 1 : length(s.pairs)
        p = s.pairs(j);
        data(size(data, 1) + 1, :) = [s.cutter s.flow s.rpm s.plane p.loc(1) p.loc(2) p.loc(3) p.vel(1) p.vel(2) p.vel(3)];
    end
end

```

Figure 14: Code snippet from file parsing program.

Before beginning analysis of the data, error in the experiment and how it was reduced should be discussed. In most experiments anomalous or extraneous data are collected due to user or equipment error. This is why experiments should be repeatable, so that any conclusions that are reached can be tested at a later time.

There is much that is unknown regarding the dredging process as it takes place along the river, lake, or ocean floor. Debris from the rotating cutterhead, turbulence from the combined rotation and suction, environmental factors, and other unknowns cause great difficulty when trying to determine the source of a problem near the floor. Similarly, when running model dredge tests, there are variables that may not be taken into account or corrected for during the duration of the experiment. Any sort of calibration could be altered slightly once the experiment begins, the ADVs can be oriented and positioned correctly but can move 1-2 cm (0.39-0.79 cm) due to the current in the dredge tank.

At this point, the focus is on examining any errors in the velocity data that might have occurred during testing due to the acoustic Doppler velocimeters. As



described in experimental setup and design, the ADVs were attached to a mounting pole that was then moved into position next to the mouth of the cutterhead. Each ADV was mounted using a combination of metal rods, pipe clamps, and thin high strength wire. The wire allowed for easy adjustment of each ADV so that they would remain level. The system is shown in Figure 15.

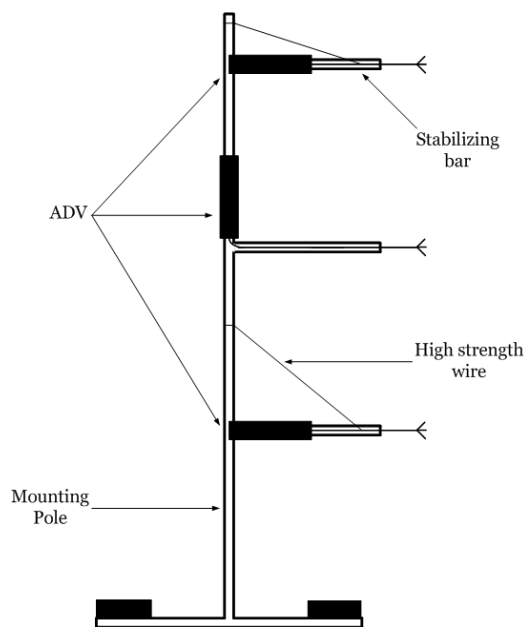


Figure 15: Detailed view of ADV mounting setup.

The mounting pole weighed greater than 22.68 kg (50 lb) and the combined weight of the ADVs was 3.6 kg (7.94 lb). Additionally, two 11.34 kg (25 lb) lead weights were used to secure the mounting pole in place. The total weight of the system was much greater than the overturning moment that could be caused by any ambient current, suction, or initial surge produced during the filling of the

dredge tank. Because of this, it is very unlikely that error was introduced due to the movement of the entire system.

The most uncertainty in the design occurs in the attachment of the ADVs to steel rods and the steel rods to the central mounting pole. Since all three of these are cylindrical shapes special attachments had to be used to secure them together. Despite the special attachments, a small amount (approximately 2-3 cm) of movement occurred when force was applied to any of the ADV arms. The wire was also used to prevent this but could not completely eliminate the problem.

It is because of this somewhat unstable attachment that there may be slight errors in the data collected during some of the different scenarios. The accuracy of each ADV is 1% of the measured velocity so this must be taken into account as well.

Secondly, spike noise in the ADV data must be removed. Spike noise can be present due to Doppler signal aliasing in turbulent flows as well as other factors (Voulgaris and Trowbridge, 1998). A number of different despiking algorithms have been developed to remove spike noise from ADV data. Goring and Nikora (2002) proposed an efficient three-dimensional phase space method that did not require any empirical coefficients. Wahl (2003) modified Goring and Nikora's method by using true 3D phase space rather than a projection in 2D space and

found that the algorithm identified more spikes. Goring and Nikora's (2002) method for spike removal was chosen for use on the data collected for this thesis. Mori, Suzuki, and Kakuno evaluated the use of the three-dimensional phase space method on ADV data in bubbly flows and developed a MATLAB software package that automates the despiking process (Mori, Suzuki, and Kakuno, 2007). Figure 16 shows a comparison between the original data and despiked data at one measurement point. The results discussed after this point have all been despiked using the process described above.

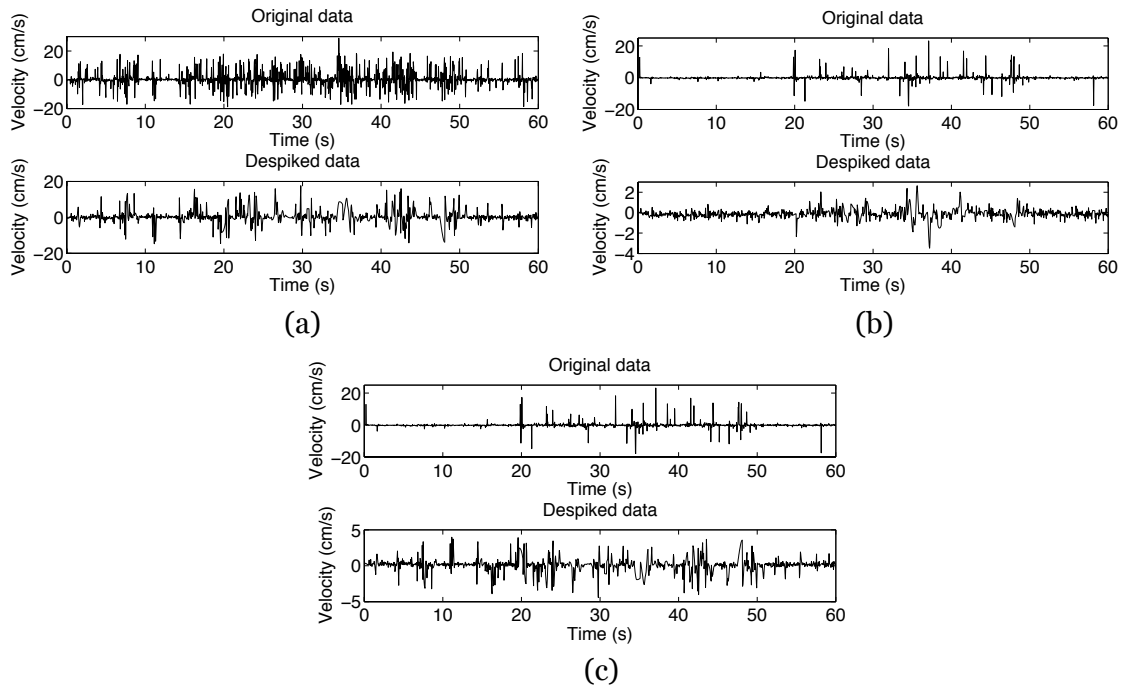


Figure 16: Comparison of original and despiked data using the method developed by Mori, Suzuki, and Kakuno (2007). (a)  $u$ -component of velocity, (b)  $v$ -component of velocity, and (c)  $w$ -component of velocity.

Finally, coordinate transformation and the difference between the ADV measurement axis and the axis of the cutter head should be discussed. As was

described earlier, the cutterhead was positioned at a  $30^\circ$  angle with respect to the x-axis of the ADV's coordinate system. In order for the velocities measured by the ADVs to be correct, each velocity vector must be transformed from the coordinate system of the ADVs (x, y, and z) to the coordinate system of the cutterhead (x', y', and z'). This was accomplished with a simple coordinate transformation. Figure 17 shows the two coordinate systems transposed onto one another and the old velocity vectors alongside the transformed velocity vectors.

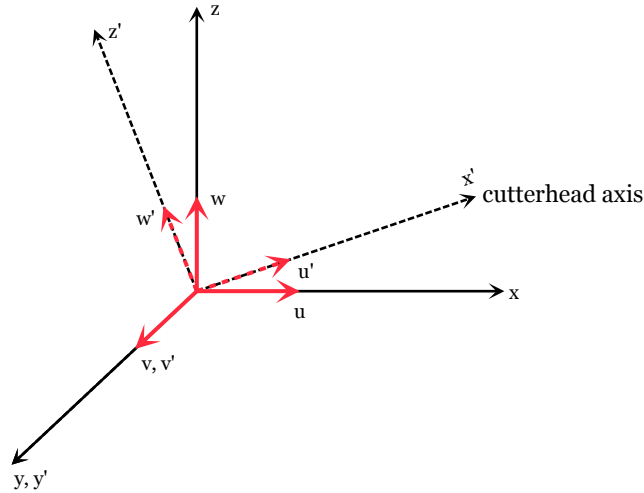


Figure 17: Velocity vector transformed from ADV axis to cutterhead axis.

The matrix equation used for the transformation is:

$$r_n = M_{no} r_o \quad (18)$$

where  $r_n = \begin{bmatrix} u_n & v_n & w_n \end{bmatrix}^T$  and  $r_o = \begin{bmatrix} u_o & v_o & w_o \end{bmatrix}^T$ . The transformation matrix

is represented by:

$$\begin{aligned}
M_{no} &= \begin{bmatrix} a_{11} & a_{12} & a_{13} & a_{14} \\ a_{21} & a_{22} & a_{23} & a_{24} \\ a_{31} & a_{32} & a_{33} & a_{34} \\ 0 & 0 & 0 & 1 \end{bmatrix} \\
&= \begin{bmatrix} (i_n \cdot i_o) & (i_n \cdot j_o) & (i_n \cdot k_o) & (\overline{O_n O_o} \cdot i_n) \\ (j_n \cdot i_o) & (j_n \cdot j_o) & (j_n \cdot k_o) & (\overline{O_n O_o} \cdot j_n) \\ (k_n \cdot i_o) & (k_n \cdot j_o) & (k_n \cdot k_o) & (\overline{O_n O_o} \cdot k_n) \\ 0 & 0 & 0 & 1 \end{bmatrix} \\
&= \begin{bmatrix} \cos(\hat{x}_n, \hat{x}_o) & \cos(\hat{x}_n, \hat{y}_o) & \cos(\hat{x}_n, \hat{z}_o) & x_n^{O_o} \\ \cos(\hat{y}_n, \hat{x}_o) & \cos(\hat{y}_n, \hat{y}_o) & \cos(\hat{y}_n, \hat{z}_o) & y_n^{O_o} \\ \cos(\hat{z}_n, \hat{x}_o) & \cos(\hat{z}_n, \hat{y}_o) & \cos(\hat{z}_n, \hat{z}_o) & z_n^{O_o} \\ 0 & 0 & 0 & 1 \end{bmatrix}
\end{aligned}$$

where  $n$  is the new coordinate system and  $o$  is the old coordinate system.  $O_n$  and  $O_o$  are the origins of the new and old coordinate axes, respectively. The elements of the  $3 \times 3$  submatrix represent the direction cosines of the old unit vectors (with respect to the ADV axis) in the new coordinate system and elements  $a_{14}$ ,  $a_{24}$ , and  $a_{34}$  represent the new coordinates of the old origin. Since the origin is not moving in this case, elements  $a_{14}$ ,  $a_{24}$ , and  $a_{34}$  will all be equal to 1 and the  $3 \times 3$  submatrix can be used on its own to transform the velocity vectors.

Taking the cosines of the various angles the transformation matrix becomes:

$$M_{no} = \begin{bmatrix} .819 & 0 & -.574 \\ 0 & 1 & 0 \\ -.574 & 0 & .819 \end{bmatrix}$$

which is a bisymmetric matrix. Multiplying by the old velocity vectors, the velocity vectors were evaluated with respect to the cutterhead coordinate system.

$$r_n = \begin{bmatrix} .819 & 0 & -.574 \\ 0 & 1 & 0 \\ -.574 & 0 & .819 \end{bmatrix} \begin{bmatrix} u_o \\ v_o \\ w_o \end{bmatrix}$$

This transformation was applied to each velocity vector and the resulting matrix is composed completely of the transformed velocities.

The first method of visualization of the velocity data was a simple quiver plot using Matlab's built in quiver function, shown in Figure 18. The location and velocity for each point is plotted in two dimensions and the length of the arrow corresponds to the magnitude of the velocity. Velocity at each point was measured for 60 seconds. At 25 Hz, this corresponds to a total of 1500 individual points. For analysis the velocities were time averaged over entire duration of the measurement.

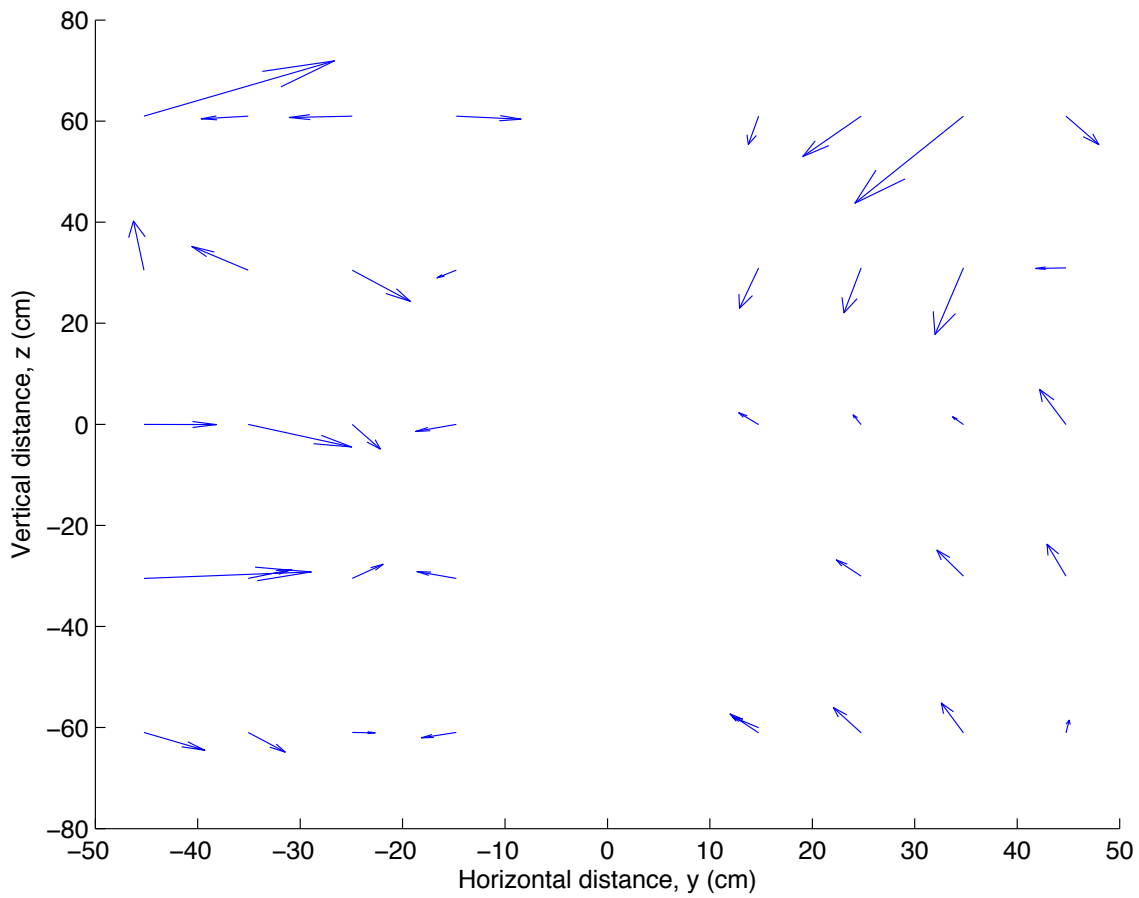


Figure 18: Velocity field plotted using a quiver plot.

Since the goal of this thesis is to determine the extent of the flow field, knowing the magnitudes of the velocity at each point are of great importance. For this reason, a color quiver plot, Figure 19, was the logical progression in visualizing the data. Color made it much easier to locate the areas of higher velocity.

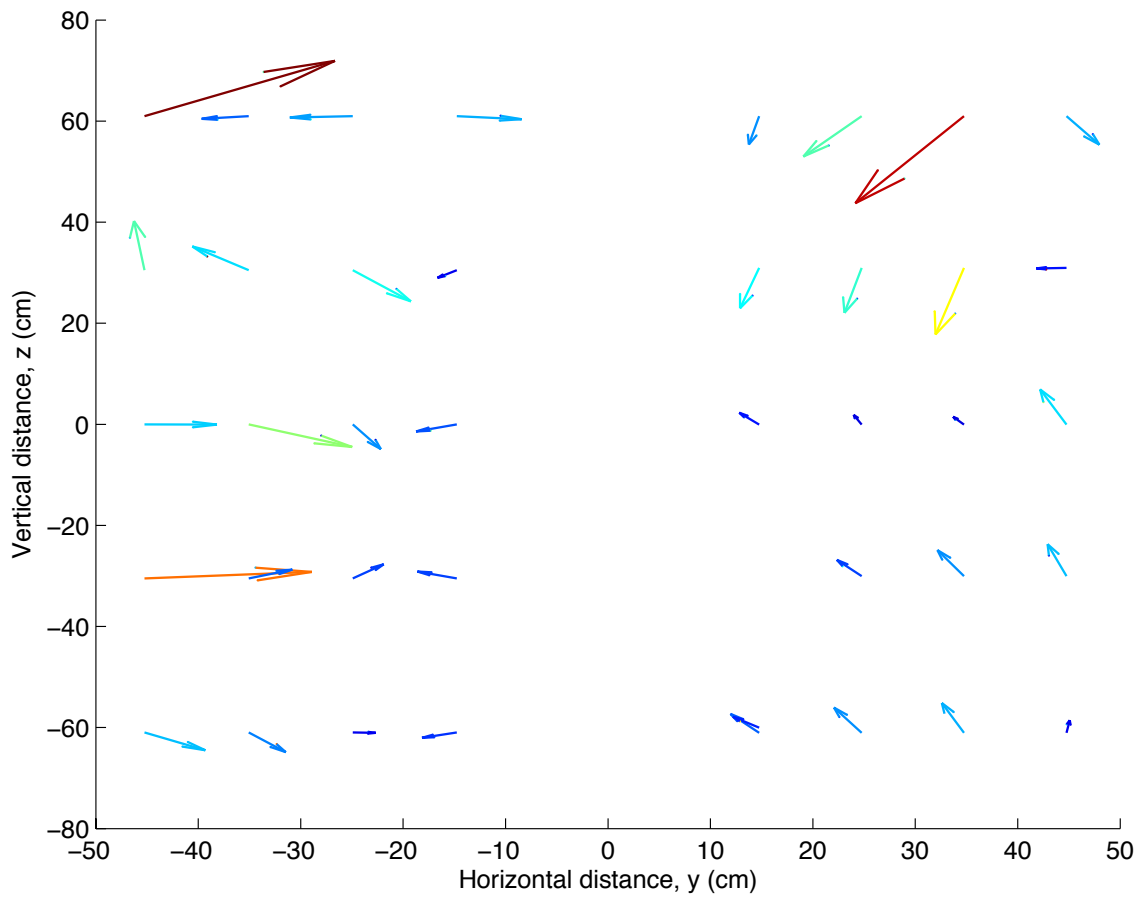


Figure 19: Velocity field plotted using a color quiver plot.

There are many ways to visualize velocity data depending on the application that is being studied. Quiver plots were used in conjunction with other methods of analysis to aid in the determination of the direction of the flow field.



## CHAPTER IV

### RESULTS AND DISCUSSION

Once data collection was completed, the analysis process began. There are a variety of parameters that affect the velocity field around the cutterhead and ultimately determine what the region of influence will be. In this case, the effects of differing flow rates and rotational velocities are investigated.

#### **Flow Rate Effects**

The primary goal of this thesis is to determine the region of influence that the suction from a cutterhead suction dredge has on the area surrounding it. As observed by Herbich and Brahme (1986), the velocity generally increases with increasing flow rate (Herbich and Brahme, 1986). This is true at the intake where the velocity is determined with the continuity equation:

$$Q = VA \tag{19}$$

However, it is less obvious at points away from the suction inlet where more complex flow occurs or when there is cutterhead rotation.

The data presented in this section are used to verify whether Herbich and Brahme's (1986) generalizations are correct as well as to draw new conclusions about the relationship between the flow rate and the extent of the velocity field. It is expected that the velocity decreases as distance from the intake increases as

well as decrease with decreasing flow rate. Once this is verified or discounted estimates of the region of influence around the cutterhead can be made.

The different scenarios are grouped together by their cutter rotational velocity.

So, for each cutter rotational velocity it is simple to compare the difference in velocities between scenarios with the cutterhead rotating at 200 GPM, 300

GPM, and 360 GPM as well as with no cutterhead attached. In addition,

scenarios that included a swing speed were grouped together by swing speed and whether the cutterhead was undercutting or overcutting. Error bars extend one

sample standard deviation above and below the calculated maximum velocity.

Error bars are useful in helping to determine if differences in values, in this case velocities, are statistically significant.

Figure 20 shows that directly in front of the cutterhead (at  $x=0$  cm) the maximum velocities for each different flow rate are higher than the two planes located 30 cm and 60 cm away. As stated previously, higher velocities are usually observed very close to the suction inlet with a rapid decrease as the distance increases.

The maximum velocities decrease with decreasing flow rate. For each flow rate, the maximum velocity 60 cm from the suction inlet is approximately 50% of the maximum velocity observed in the plane of the suction inlet ( $x=0$  cm).

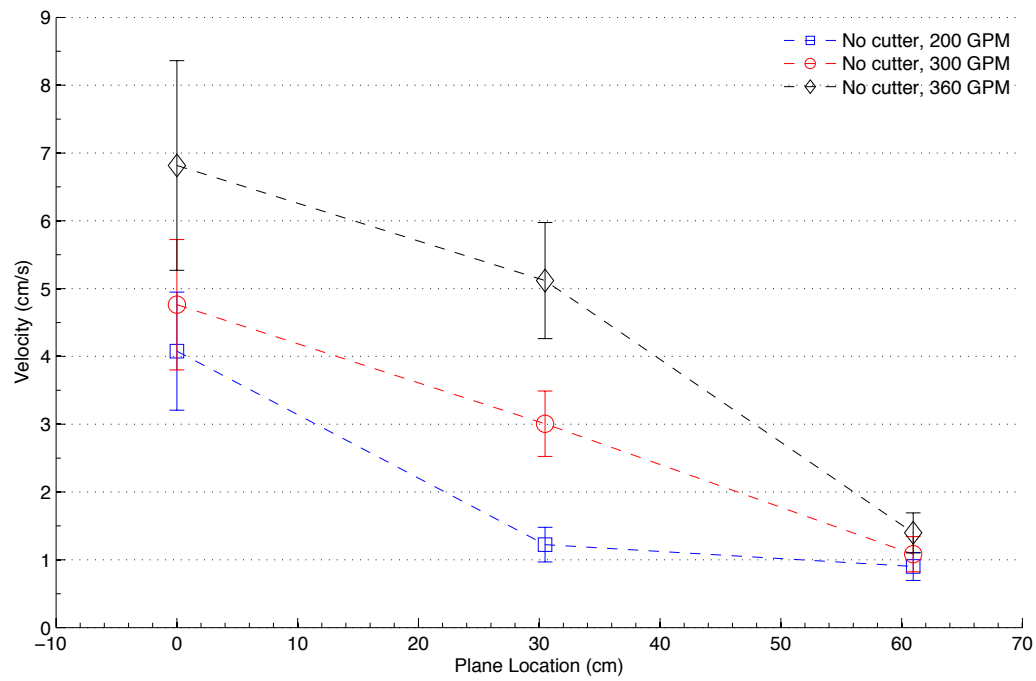


Figure 20: Plane location vs. maximum velocity at various x-planes for the no cutterhead scenario.

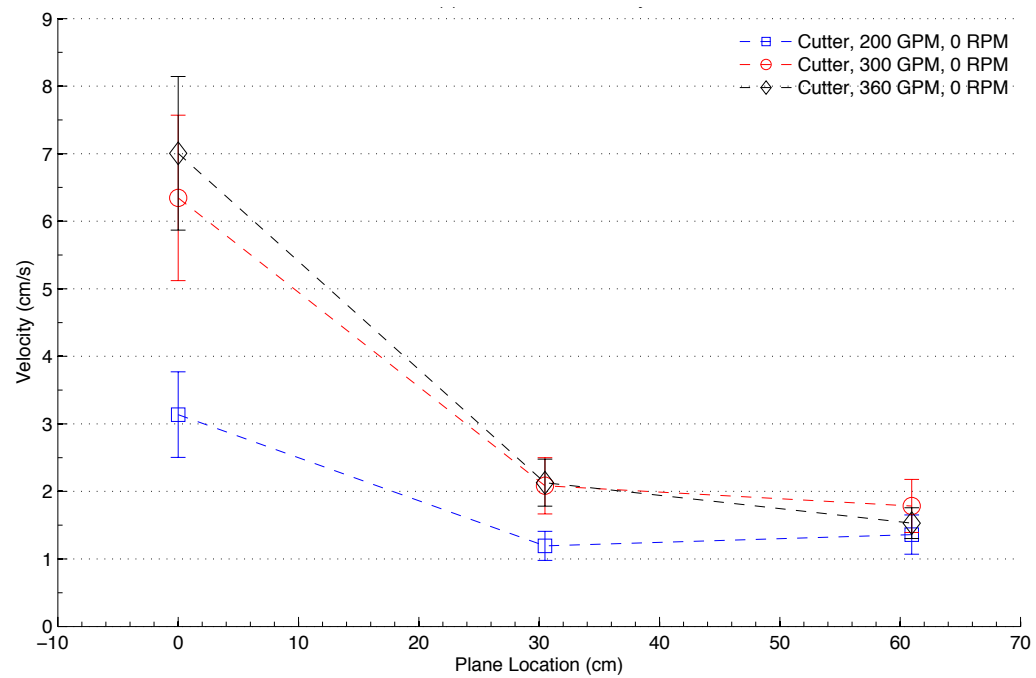


Figure 21: Plane location vs. maximum velocity at various x-planes for the cutterhead attached, 0 RPM scenario.

Figure 21 shows that the expected maximum velocity behavior is present once again in the plane of the cutterhead. The maximum velocities measured nearest the cutterhead are similar to those when no cutterhead was attached. In fact, the velocities are slightly greater at the lower flow rate without the cutterhead, possibly due to the lack of obstruction. Herbich and Brahme (1986) found that the presence of a stationary cutterhead did not affect the region of influence of the velocity field on the surrounding area. However, it is possible that maximum velocities are reduced without effecting overall extent of sediment pick-up.

As with the no cutterhead scenario, the maximum velocities at the furthest plane were approximately 50% of the maximum velocities at the nearest plane. There is a slight decrease in the velocities near the suction inlet due to the obstruction of the blades, cutterhead ring, and plates within the cutter. However, the decrease is not significant.

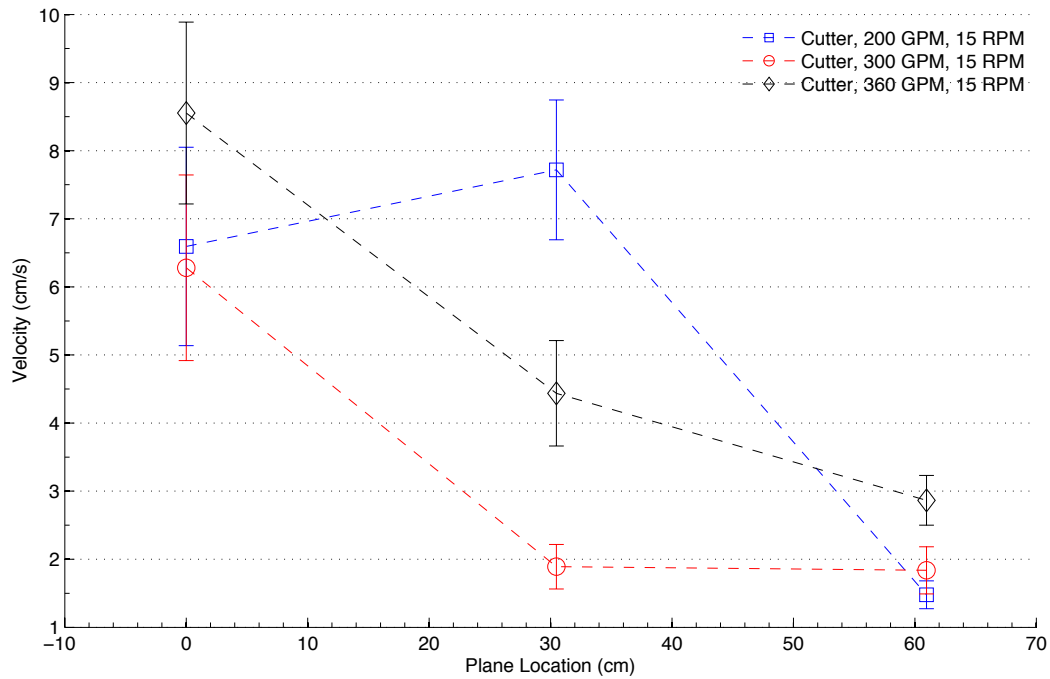


Figure 22: Plane location vs. maximum velocity at various x-planes for the cutterhead attached, 15 RPM scenario.

Figure 22 shows there was a difference from the two groups of scenarios previously examined. The maximum velocities recorded for the 200 GPM flow rate were greater than those at the 300 GPM flow rate for the planes located at  $x=0$  cm and  $x=30$  cm. This behavior is difficult to explain and could possibly be due to measurement error.

Examining Figures 20, 21, and 22 it is clear that there is a significant decrease in maximum velocities as the distance between the cutterhead and plane of measurement is increased. This explains the lack of correlation between flow rate and maximum velocity at  $x=30$  cm and  $x=60$  cm.

In the three scenarios examined above, the highest velocities caused by the suction, cutterhead rotation, or a combination of both occur very near the cutterhead. This was expected and serves as a validation of Herbich and Brahme's observations (1986). Since the decrease in velocity was so great, at least 50%, it is likely that the effects of the cutterhead rotation and suction decrease in significance at a distance greater than or equal to 30 cm in front of the cutterhead. It is difficult to determine from the data collected whether this is true at all points around the cutterhead or only directly in front of the suction intake.

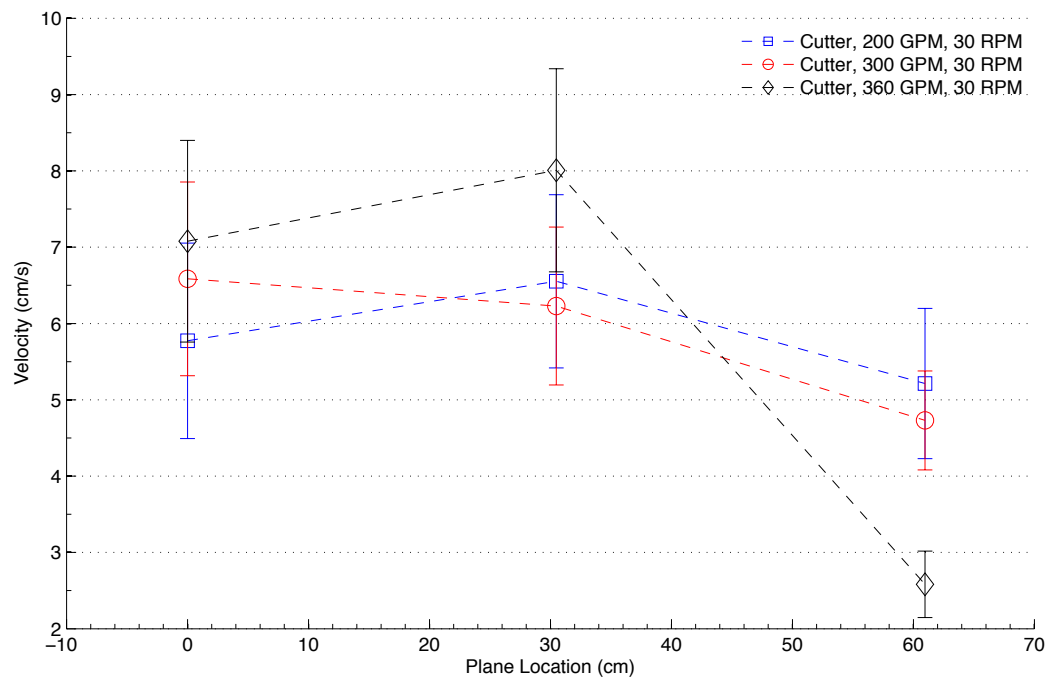


Figure 23: Plane location vs. maximum velocity at various x-planes for the cutterhead attached, 30 RPM scenario.

It is clear from Figure 23 that the 30 RPM scenario does not share the characteristics of the three previously examined scenarios. Rather than exhibiting a sharp decline in maximum velocities at  $x=30$  cm, the velocities are rather constant with a slight increase  $x=30$  cm. Compared to the other scenarios, a cutterhead rotational speed of 30 RPM has a visible effect on the maximum velocity at each plane of measurement, in particular at  $x=30$  cm and  $x=60$  cm. Since velocities were only measured up to 60 cm in front of the cutterhead it is not possible to determine where a significant decline in maximum velocity occurs. It will be at greater than 60 cm, though.

Examining the planes that are perpendicular to the floor of the dredge tank and parallel to the south wall, the y-planes, adds a second dimension to the analysis of how the flow rate affects the maximum velocity. At each different cutterhead rotation speed and when no cutterhead was attached the correlation between flow rate and maximum velocity is strong.

For the no cutterhead scenario shown in Figure 24 the suction intake was centered at  $x=0$  cm. It was possible to take measurements without having to worry about any interaction between the cutterhead and ADV since the cutterhead was not attached.

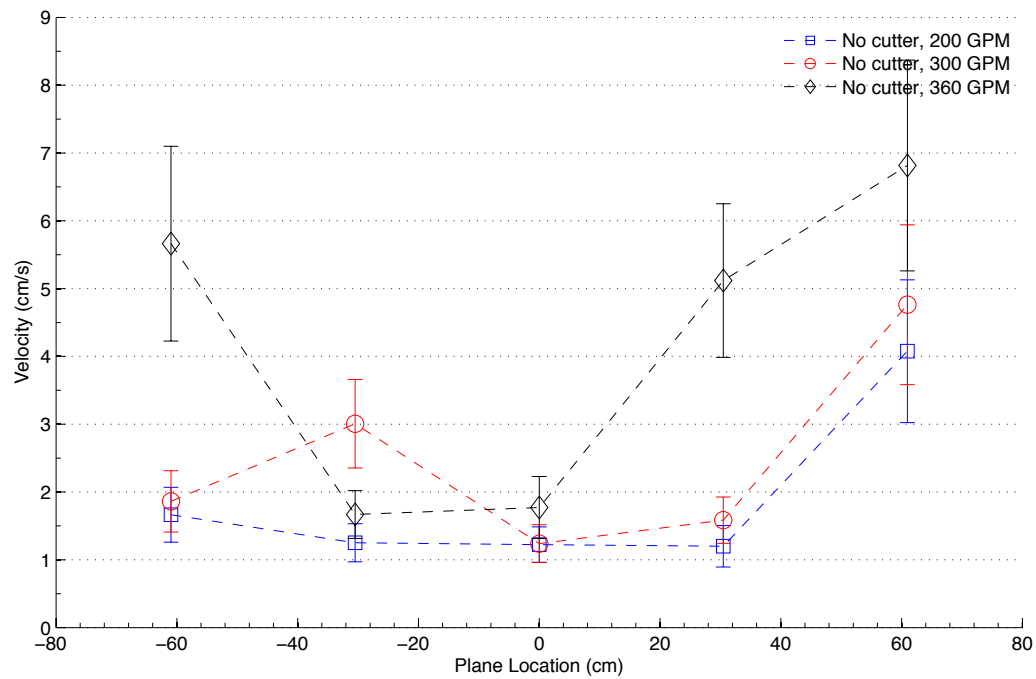


Figure 24: Plane location vs. maximum velocity at various y-planes for the no cutterhead scenario.

All three scenarios in which the cutterhead is attached, whether it is rotating or not are similar, the maximum velocities peak just to the right and left of the cutterhead. This is shown in Figures 25, 26, and 27. In Figure 25 the maximum velocities peak approximately 44 cm to the left of the center of the suction intake and 44 cm to the right of the center of the suction intake. The cutterhead was 25.4 cm (0.83 ft) in diameter which means that the maximum velocities occurred 31 cm (1.02 ft) to the left and right of the cutterhead.



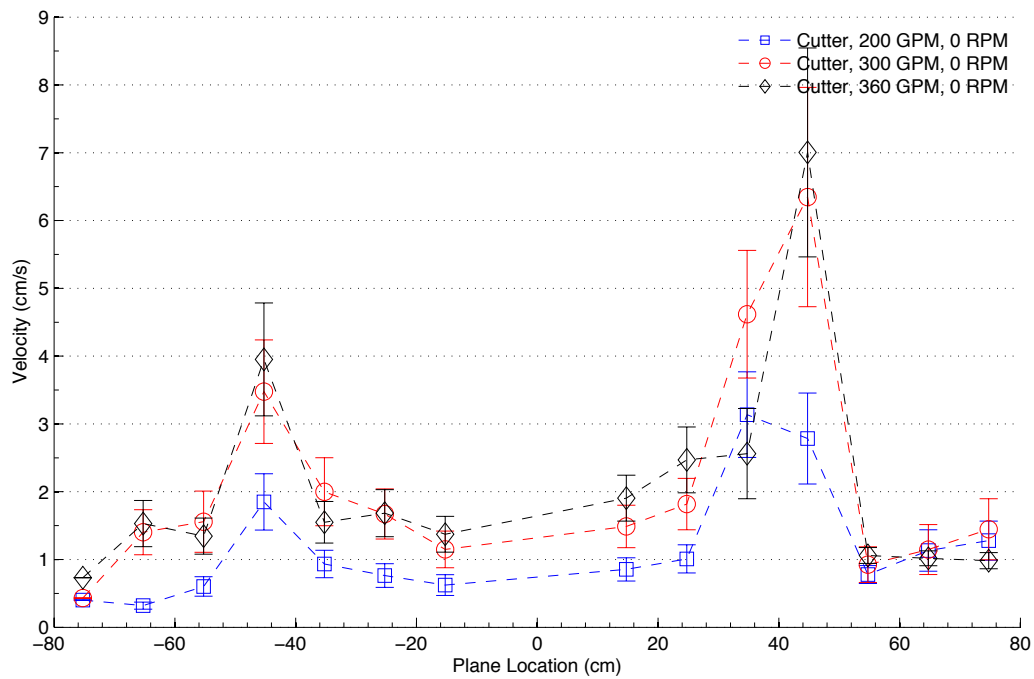


Figure 25: Plane location vs. maximum velocity at various y-planes for the cutterhead attached, 0 RPM scenario.

In Figure 26 the maximum velocities peak approximately 26 cm to the left of the center of the suction intake and 44 cm to the right of the center of the suction intake. This means that the maximum velocities occurred 13.3 cm (0.44 ft) to the left of the cutterhead and 31 cm (1.02 ft) to the right of the cutterhead.

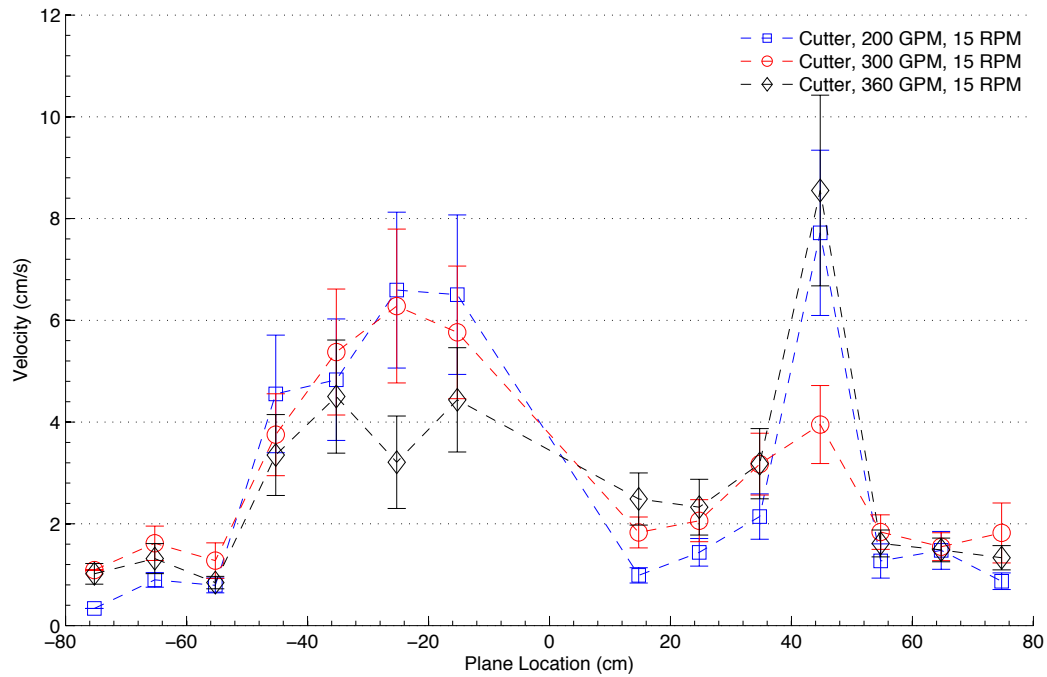


Figure 26: Plane location vs. maximum velocity at various y-planes for the cutterhead attached, 15 RPM scenario.

For the 30 RPM scenarios, shown in Figure 27, the maximum velocities peak approximately 16 cm to the left of the center of the suction intake and 36 cm to the right of the center of the suction intake. This means that the maximum velocities occurred 3.3 cm (0.11 ft) to the left of the cutterhead and 23.3 cm (0.76 ft) to the right of the cutterhead. There is a trend in which the maximum velocities occur nearer the cutterhead as the cutterhead rotation speed is increased.

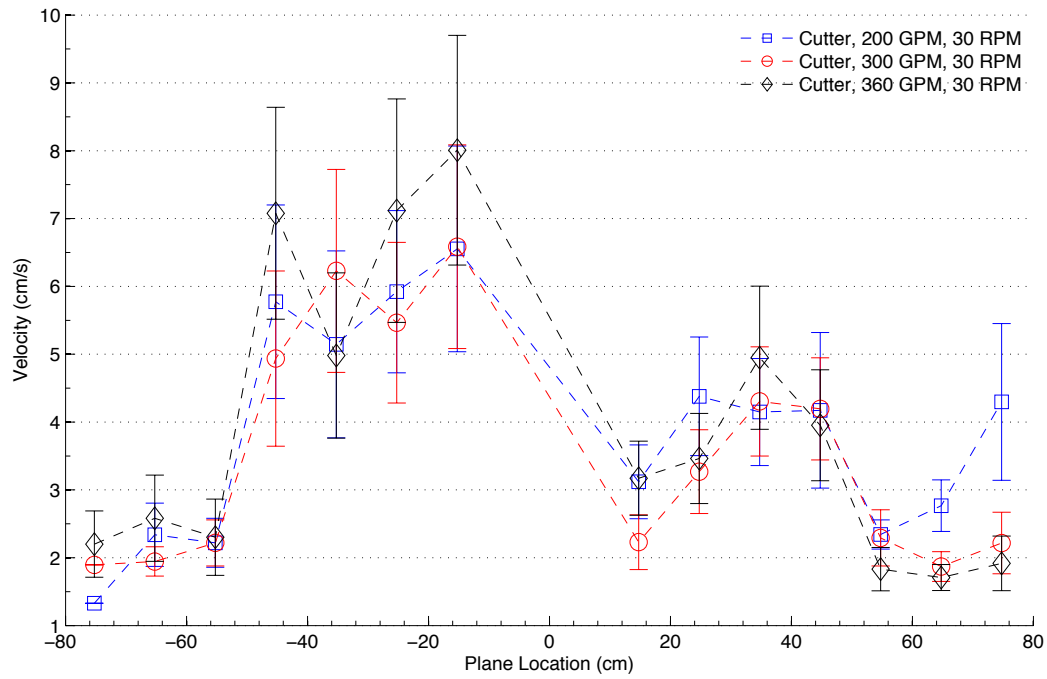


Figure 27: Plane location vs. maximum velocity at various y-planes for the cutterhead attached, 30 RPM scenario.

The analysis of the maximum velocities in each of the different z-planes was less helpful than the other two planes of measurement. For the most part, any conclusions that could be made were contradicted by another scenario, rendering the analysis inconclusive. The results are shown in Figures 28, 29, 30, and 31.

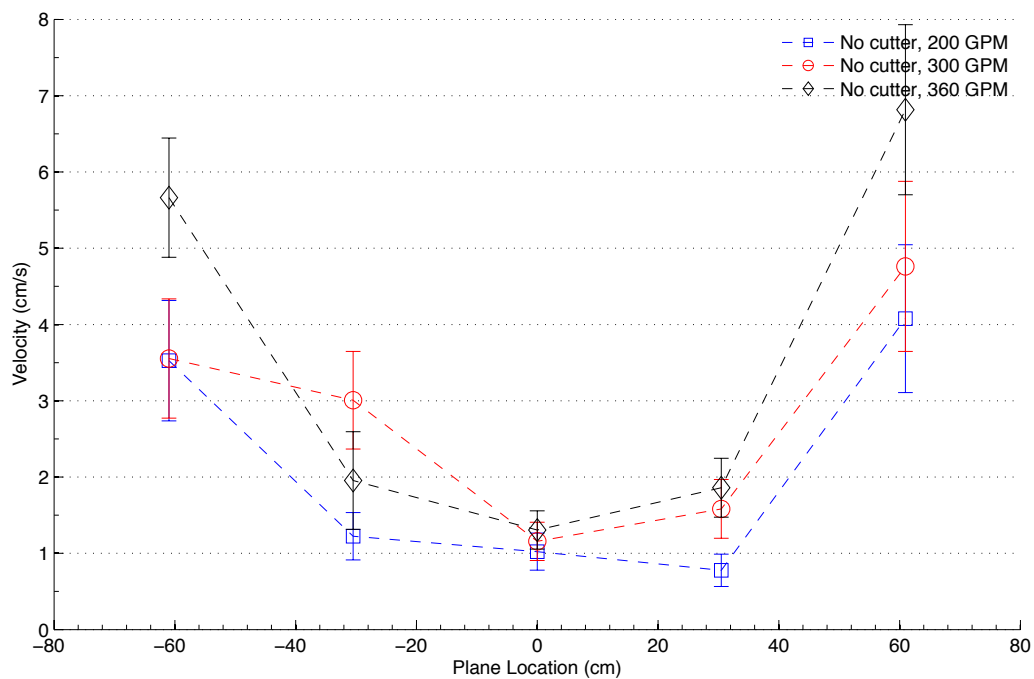


Figure 28: Plane location vs. maximum velocity at various z-planes for the no cutterhead attached scenario.

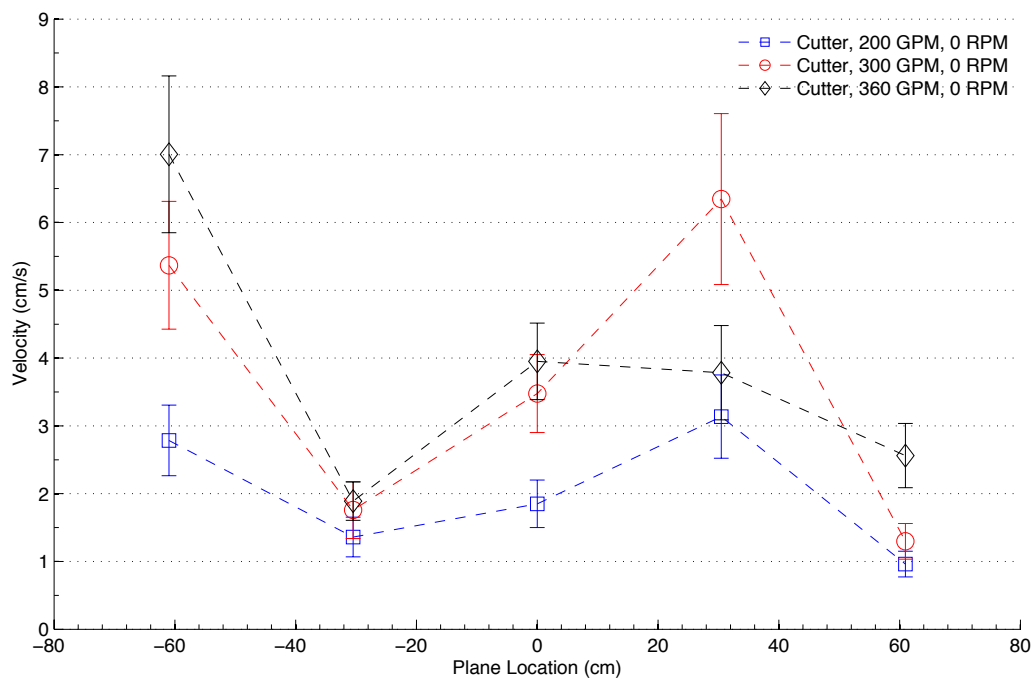


Figure 29: Plane location vs. maximum velocity at various z-planes for the cutterhead attached, 0 RPM scenario.

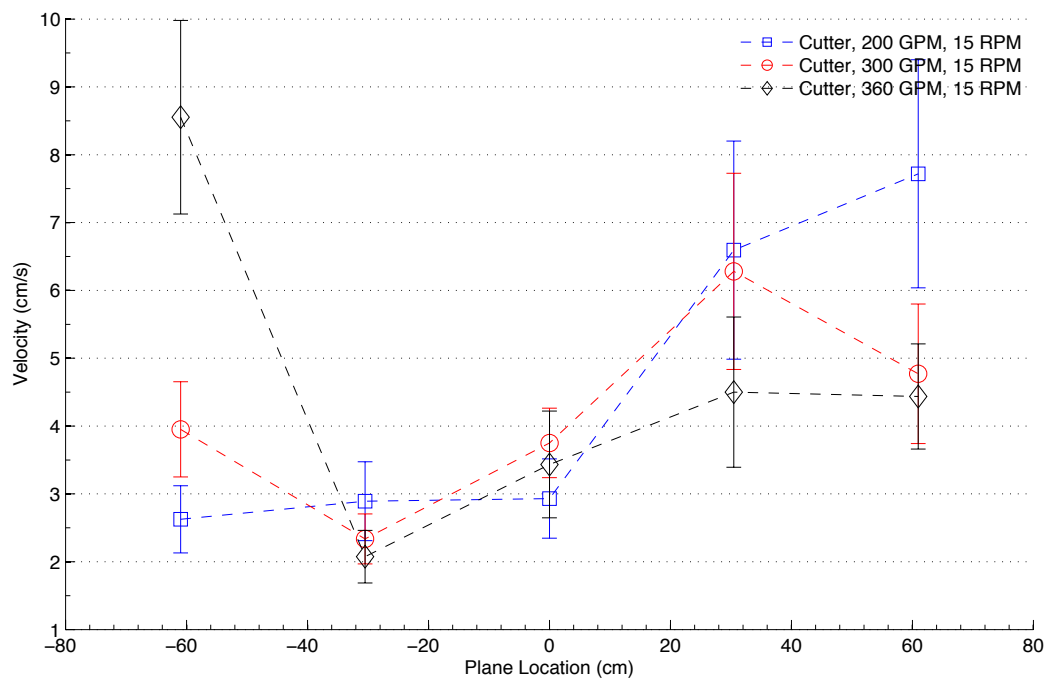


Figure 30: Plane location vs. maximum velocity at various z-planes for the cutterhead attached, 15 RPM scenario.

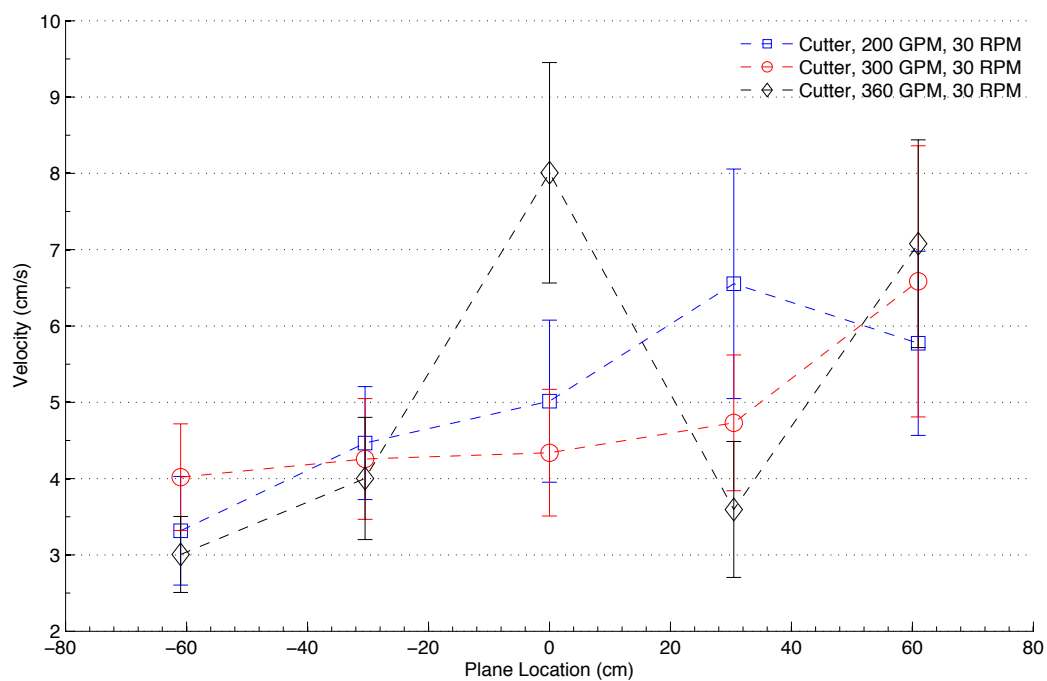


Figure 31: Plane location vs. maximum velocity at various z-planes for the cutterhead attached, 30 RPM scenario.

With the exception of the scenario with the cutterhead attached rotating at 30 RPM, there were much higher velocities at the upper and lowermost planes of measurement. This can be explained simply in the scenarios when the cutterhead is present. Since the cutterhead is 25 cm in diameter, measurements could not be taken directly in front of the suction inlet - so the nearest measurements were located approximately 30 cm away. The suction inlet is kidney bean shaped so velocities should be higher in the lower half of the cutterhead as well as below cutterhead. This is indeed the case as shown in Figures 29 and 30. However, it is clear that in Figure 31 there is little change in velocity above or below the cutterhead. In Figure 28, there is a slight increase directly below the suction inlet but the most prominent increase occurs 60 cm below at  $z = 154$  cm. Since the cutterhead was not attached in this scenario, measurements were taken directly in front of the cutterhead so the plot should not exhibit the same characteristics as Figures 29, 30, and 31 in terms of significant velocity increases above and below the cutterhead.

In both the overcutting and undercutting scenarios the maximum velocities were greatest in the x-planes measured nearest the cutterhead. Figures 32 and 33 show the overcutting and undercutting scenarios, respectively. This is caused by the superposition of the swing speed, cutterhead rotation speed, and suction flow rate. The cutterhead rotation speed and suction flow rate have their greatest effect near the cutterhead so the addition of a constant swing speed will simply

increase the maximum velocities. It is clear that higher swing speed results in higher maximum velocities; however, the velocities are not twice as large for the 8 cm/s swing speed scenarios compared to the 4 cm/s swing speed scenarios. Maximum velocities occur at ~10 cm/s with a swing speed of 8 cm/s but range from 5 cm/s to 8 cm/s when swinging at 4 cm/s. The constant maximum velocities are due to an error in measurement technique. Since the ADVs were attached directly to the swinging ladder, the velocities that were measured were dominated by the velocity resulting from the swinging motion.

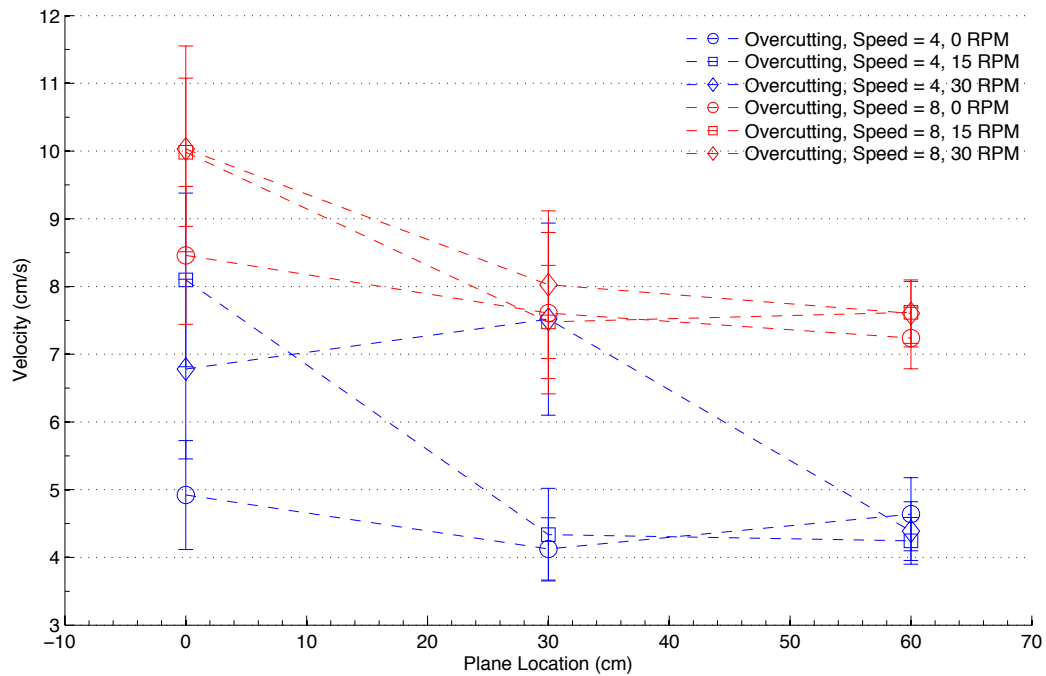


Figure 32: Plane location (x) vs. maximum velocity for overcutting scenarios.

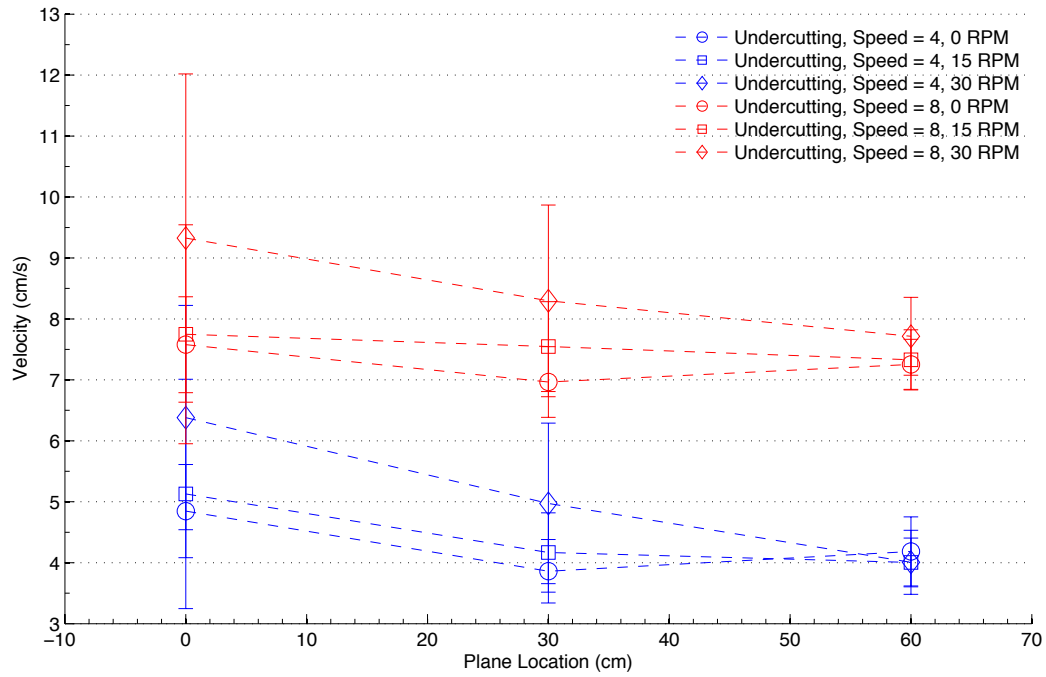


Figure 33: Plane location (x) vs. maximum velocity for undercutting scenarios.

The maximum velocities measured in the y-planes were relatively steady in each scenario as shown in Figures 34 and 35. The magnitudes were slightly increased between the planes located at 90 cm and 120 cm. These planes are located directly in front of the cutterhead's leading edge as it is making the cut so an increase in velocity there was expected.



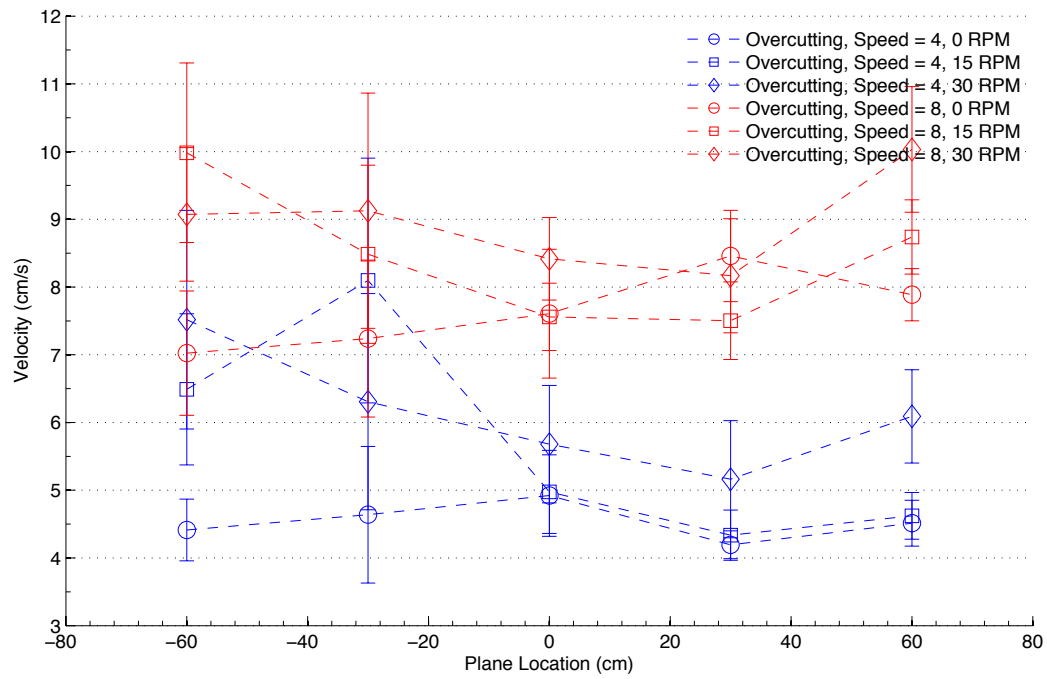


Figure 34: Plane location (y) vs. maximum velocity for overcutting scenarios.

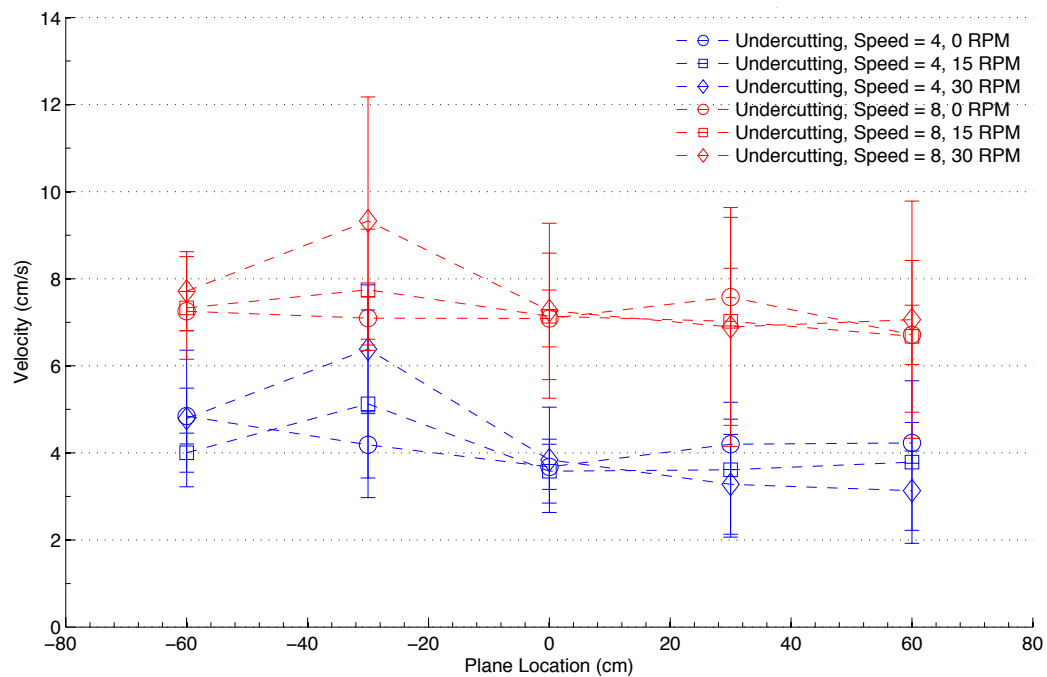


Figure 35: Plane location (y) vs. maximum velocity for undercutting scenarios.

Velocities above the cutterhead were greater in the overcutting scenarios. There is an approximate 2 cm/s increase when overcutting than when undercutting. In both the overcutting and undercutting scenarios the maximum velocities were steady across all of the z-planes measured above the cutterhead. Figures 36 and 37 show the maximum velocities in each of the measured z-planes.

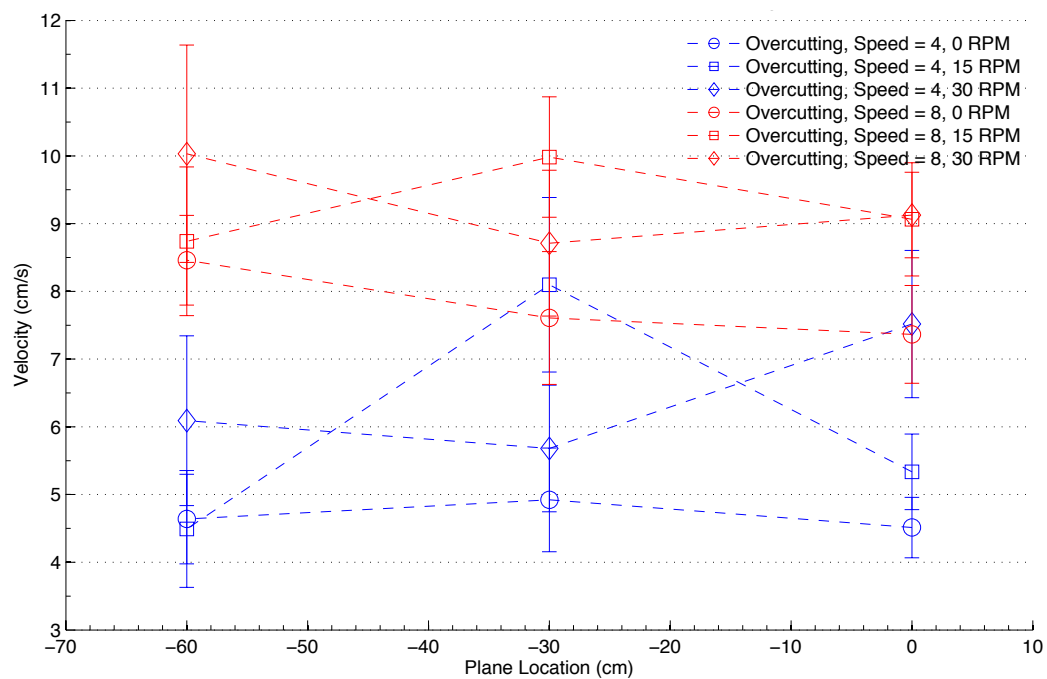


Figure 36: Plane location (z) vs. maximum velocity for overcutting scenarios.

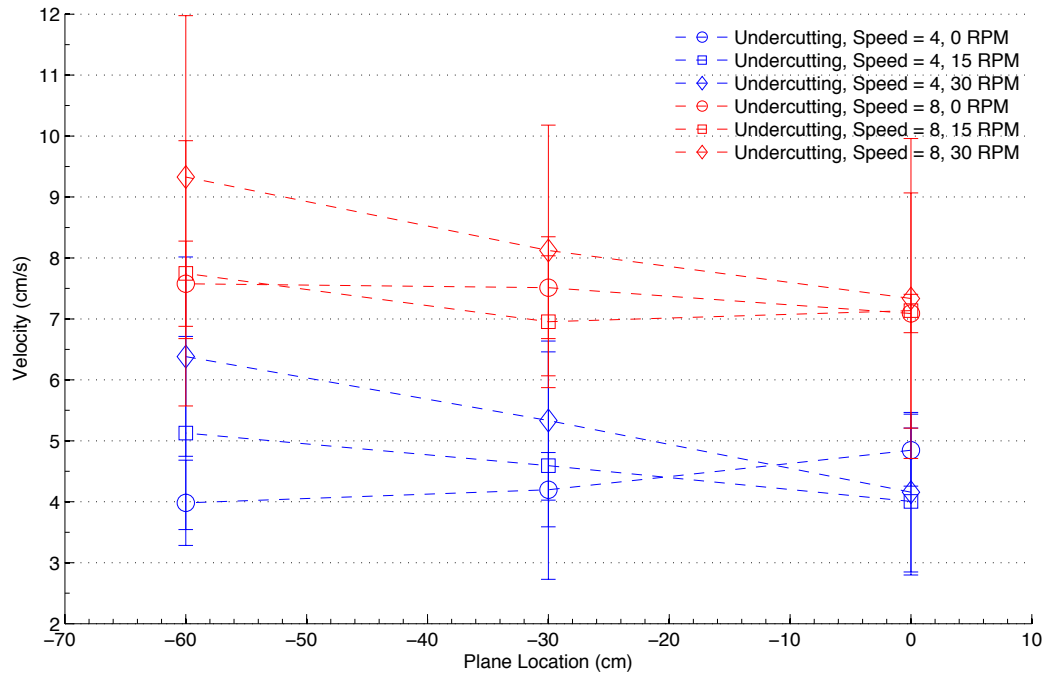


Figure 37: Plane location (z) vs. maximum velocity for undercutting scenarios.

## Rotation Effects

In many situations some type of agitation is required to loosen the sediment and allow for the suction to draw the sediment into the pipe and then into a hopper or different location. Depending on the type of material being dredged, the dredge operator chooses the most efficient rotational speed of the cutterhead. The rotational speed must be great enough so that the sediment is taken inside the cutterhead and into the suction inlet. Below a certain cutterhead rotational speed the sediment particles will simply roll off of the cutterhead blades and very little of the sediment is removed (Burger, 2003).

Previously, in the Flow Rate section, the effects of flow rate on the velocity field around the cutterhead were examined. Now, the same analysis is applied to the effect of cutterhead rotational velocity on the surrounding velocity field in order to gain new insight. New patterns emerge that eventually aid in the determination of a region of influence around the cutterhead.

The different scenarios are grouped together by their flow rate. So, for each flow rate it is simple to compare the difference in velocities between scenarios with the cutterhead rotating at 0 RPM, 15 RPM, and 30 RPM as well as with no cutterhead attached.

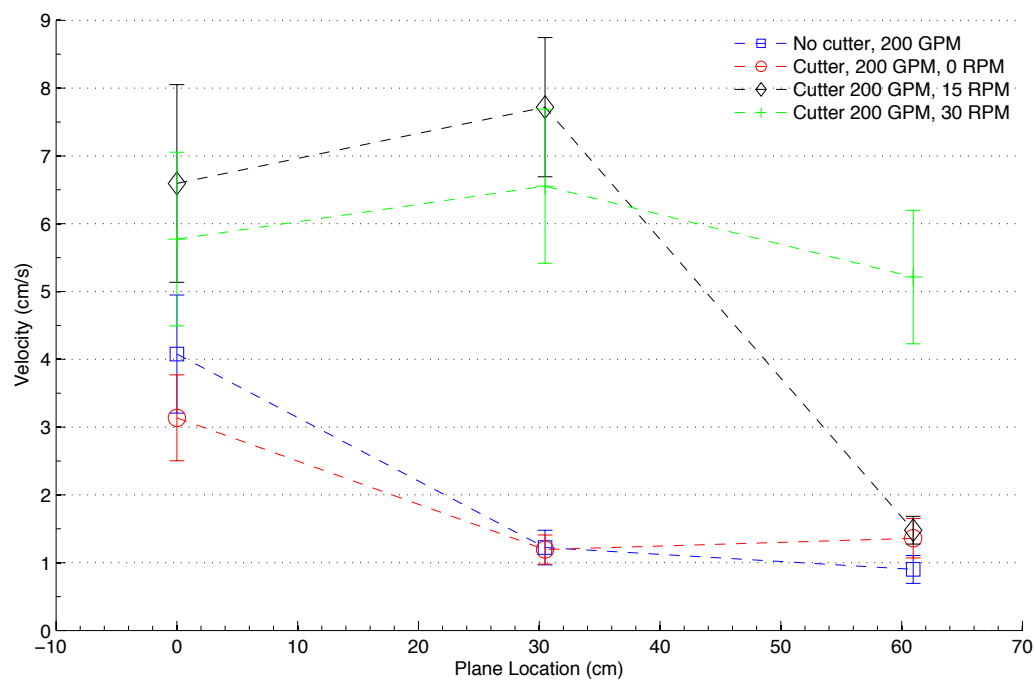


Figure 38: Plane location vs. maximum velocity at various x-planes for the different 200 GPM scenarios.

The highest velocities for the 200 GPM scenarios with no cutterhead attached and with a stationary cutterhead occurred in the plane nearest the cutterhead; approximately twice that measured in the other two planes. This is the same behavior that was observed when analyzing the effects of flow rate on the velocities. At higher cutterhead rotational speeds, 15 and 30 RPM, the maximum velocities do not decrease until 60 cm from the cutterhead. As seen in Figure 38, the highest velocities were observed at a rotational velocity of 15 RPM. This is not entirely unexpected since the velocity field was found to depend solely on the flow rate through the suction inlet (Herbich and Brahme, 1986).

It is notable that when the cutterhead was rotating at 30 RPM, the maximum tested, there were no decreases in maximum velocities over the three distances measured. The higher rotational speed caused the extent of high velocity to greatly increase. Burger showed that increasing the cutterhead rotational speed would increase the production up to a certain point (~100 RPM). Further increasing the rotational velocity would result in a decrease in production due to large centrifugal forces.

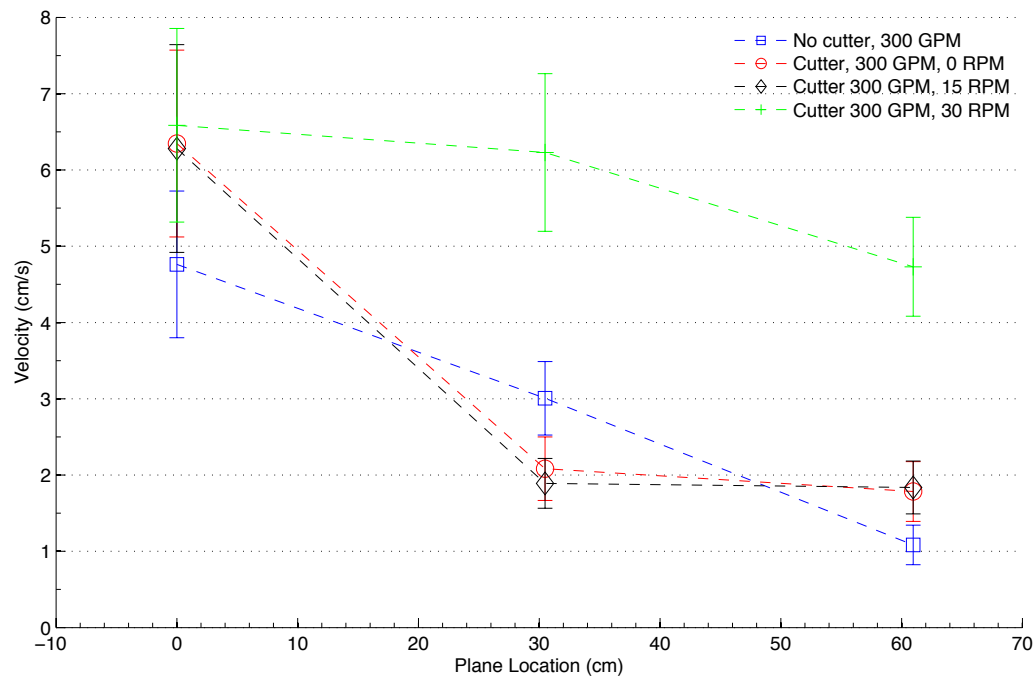


Figure 39: Plane location vs. maximum velocity at various x-planes for the different 300 GPM scenarios.

As expected the highest velocities for the scenarios with a 300 GPM flow rate, shown in Figure 39, occurred in the plane nearest the cutterhead. They were approximately 2-3 times greater than the velocities in the other planes. With the cutterhead rotating at 30 RPM the high velocities are sustained throughout all three planes of measurement. This is the same behavior that occurred in the 200 GPM group of scenarios and it is clear that this is caused by the cutterhead rotational speed and not the flow rate.

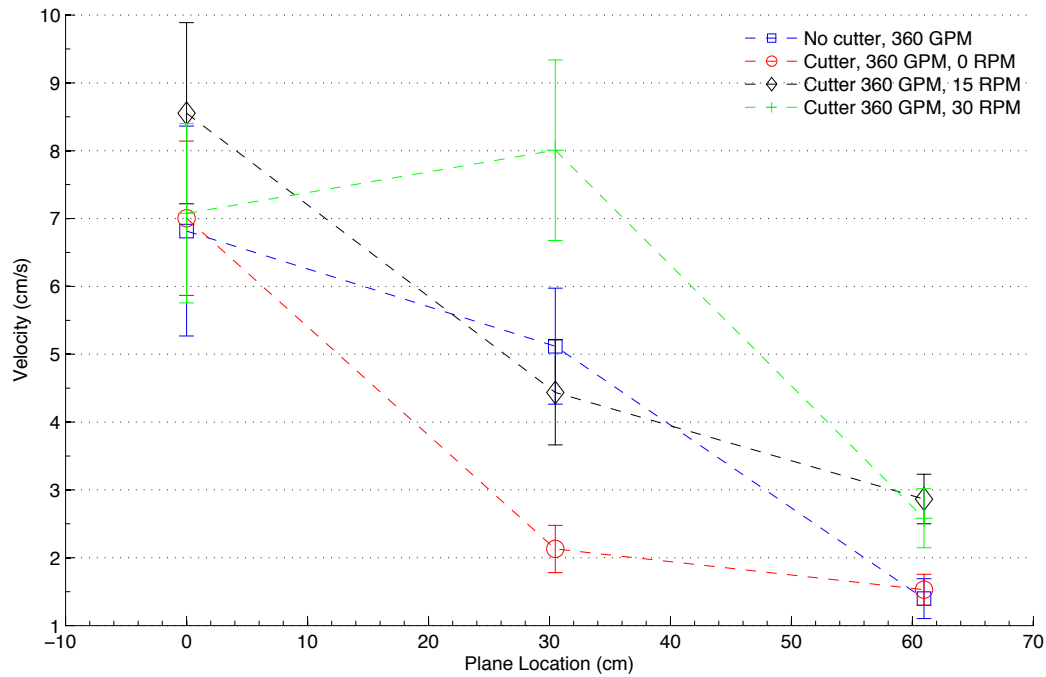


Figure 40: Plane location vs. maximum velocity at various x-planes for the different 360 GPM scenarios.

The groups of scenarios at 300 GPM and 360 GPM were similar, as shown in Figures 39 and 40. At 360 GPM, the maximum velocities were approximately 2-3 cm/s greater than those at 300 GPM. The maximum velocities nearest the cutterhead ( $x=0$  cm) were 2-3 times greater than those in the second and third planes at  $x=30$  cm and  $x=60$  cm, respectively.

Plots of the maximum velocity versus the various y-planes are useful in determining where the suction is greatest with respect to the cutterhead. When no cutterhead is attached it is expected that the velocity will be greatest directly in front of the suction inlet and either decrease or stay approximately the same as the distance increases to the left or right of the inlet. It is unknown exactly

how the addition of the cutterhead affects the behavior of the velocity field around the cutterhead. Examining the maximum velocity helps determine this behavior. There are many similarities between Figures 24, 25, 26, and 27 in the flow rate section and Figures 41, 42, and 43 presented in this section.

In Figure 41 it is clear that the highest velocities occur to the left and right of the cutterhead. In this case, the velocities to the left are greatest at approximately 20 cm (0.66 ft) from the suction inlet and to the right are greatest at approximately 40 cm (1.31 ft). These maximums occur when the cutterhead is rotating. Since the 30 RPM scenario has the highest overall velocities followed by the 15 RPM and 0 RPM scenarios it is possible that there is a correlation between the speed of cutterhead rotation and maximum velocities. When the cutterhead is not rotating the highest velocities occur to the right of the cutterhead. This is due to the geometry of the cutterhead blades and the counterclockwise rotation. Ideally, the cutterhead blades would not affect the velocity field and velocities would be equal at all points around the cutterhead. However, the blades (when not rotating) partially block the flow from entering from the left side and therefore decrease the velocity.



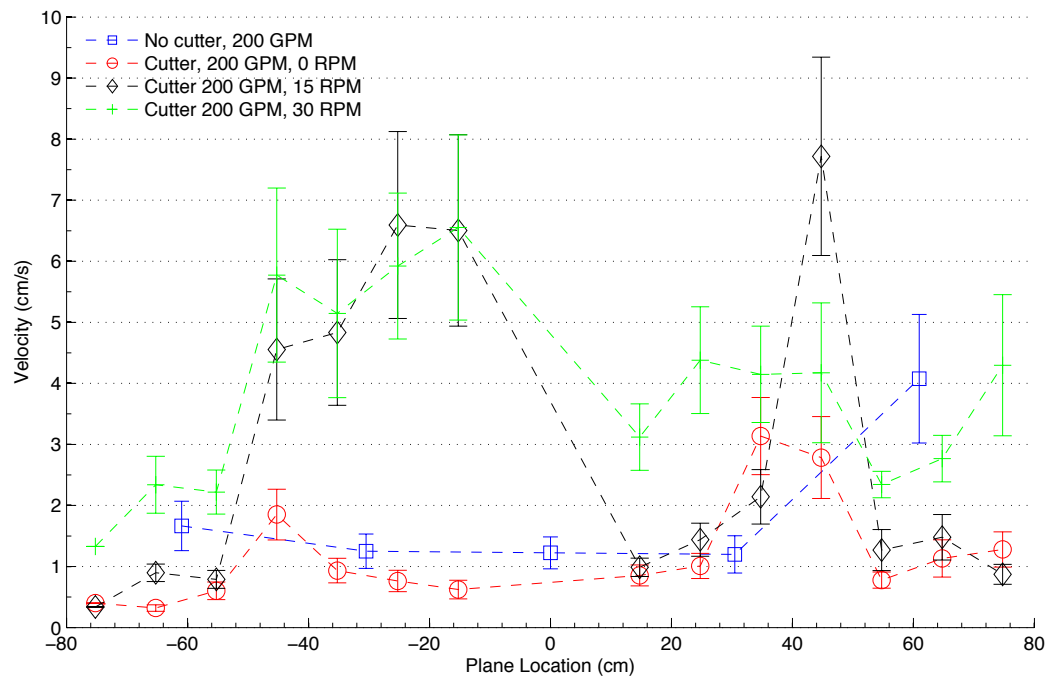


Figure 41: Plane location vs. maximum velocity at various y-planes for the different 200 GPM scenarios.

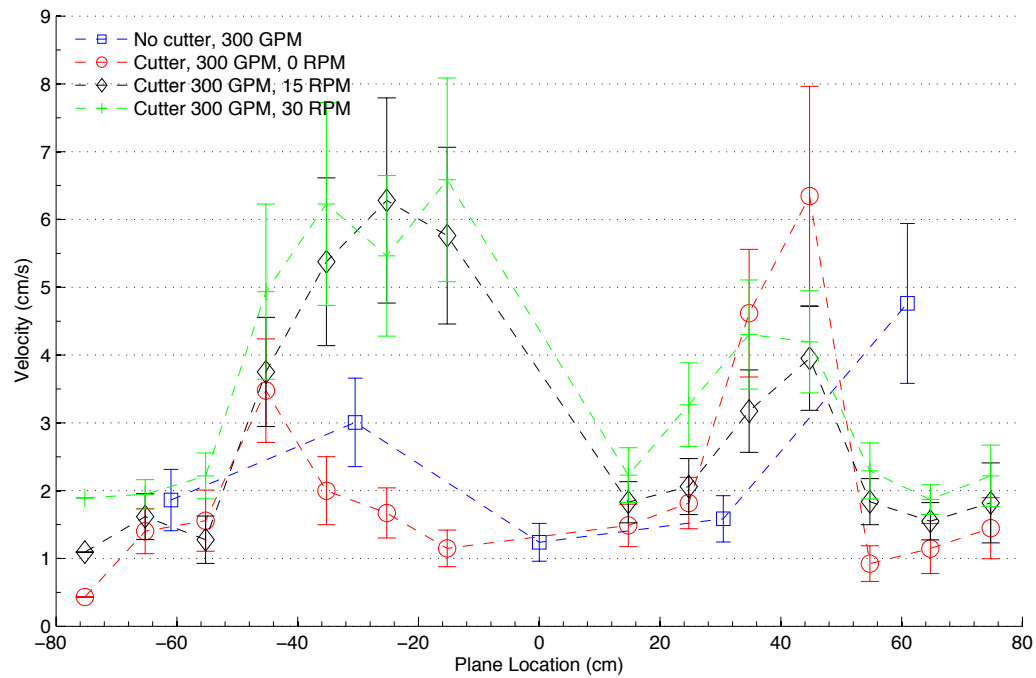


Figure 42: Plane location vs. maximum velocity at various y-planes for the different 300 GPM scenarios.

The results in Figure 42 are similar to those in Figure 41. There are elevated velocities on either side of the cutterhead which are most noticeable when the cutterhead is rotating. The velocities to the left are greatest at approximately 28 cm (0.92 ft) from the suction inlet and to the right are greatest at approximately 44 cm (1.44 ft). When the cutterhead is stationary the maximum velocities only increase to the right of the cutterhead. This is in line with the observations made for the 200 GPM flow rate. Once again, there is a strong correlation between the rotational velocity and maximum velocity. Rotation at 30 RPM caused slightly higher velocities than at 15 RPM and much higher than for a stationary cutterhead. The same velocity increase for the stationary cutterhead occurred to the right of the cutterhead. This strengthens the hypothesis that the cutterhead design affects the velocity field surrounding it.

Most of the observations to be made about Figure 43 have already been made in discussion of Figures 41 and 42. The behavior of the velocities in this scenario serves to reinforce the observations made previously.

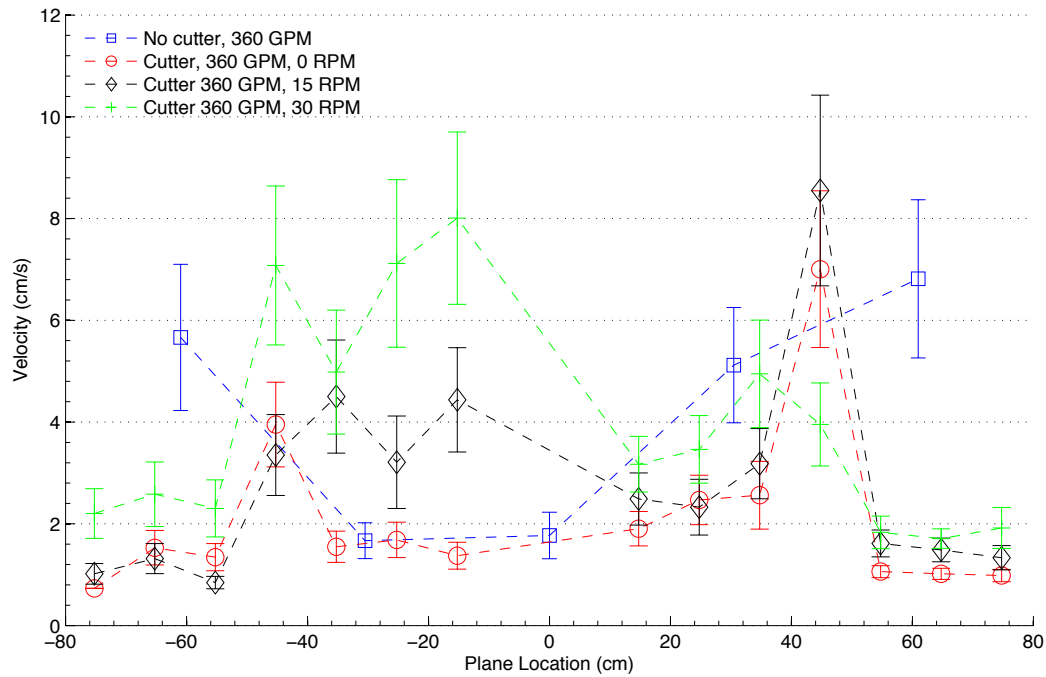


Figure 43: Plane location vs. maximum velocity at various y-planes for the different 360 GPM scenarios.

Figures 44, 45, and 46 show the maximum velocities in each z-plane (plane with constant z above the dredge tank floor). The figures are all similar so observations can be made about them in general. There is an increase in maximum velocities below the cutterhead and conversely a decrease above the cutterhead. Generally, the higher the cutterhead speed the greater the maximum velocities are. This is the case at both 200 GPM and 300 GPM, however, at 360 GPM, in Figure 46, the maximum velocities are much greater when the cutterhead is stationary and rotating at 15 RPM.

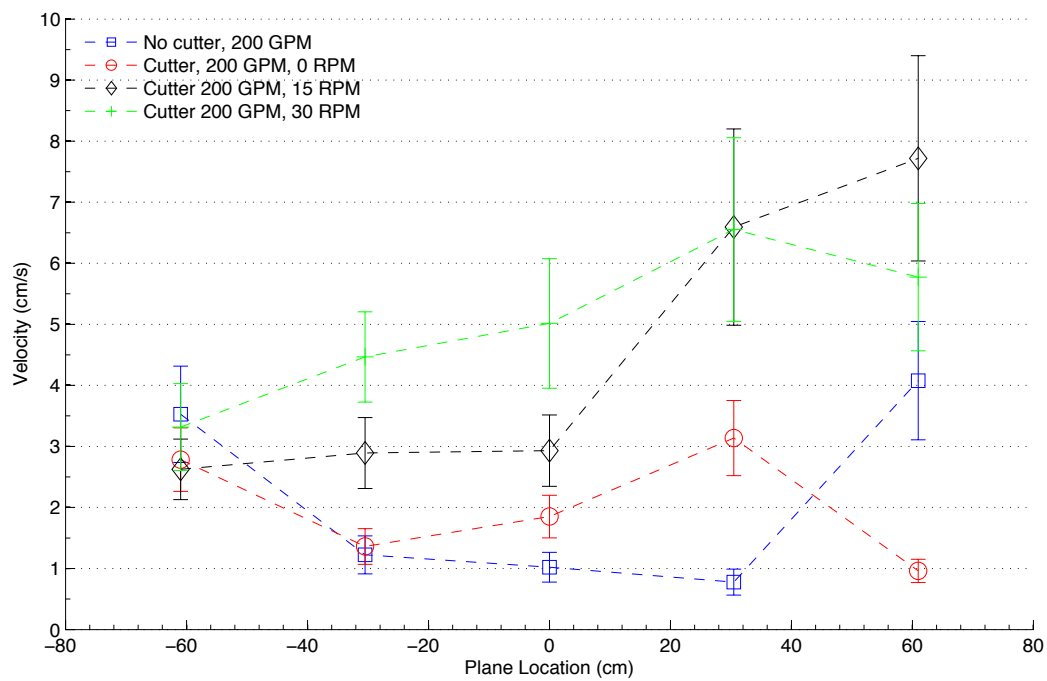


Figure 44: Plane location vs. maximum velocity at various z-planes for the different 200 GPM scenarios.

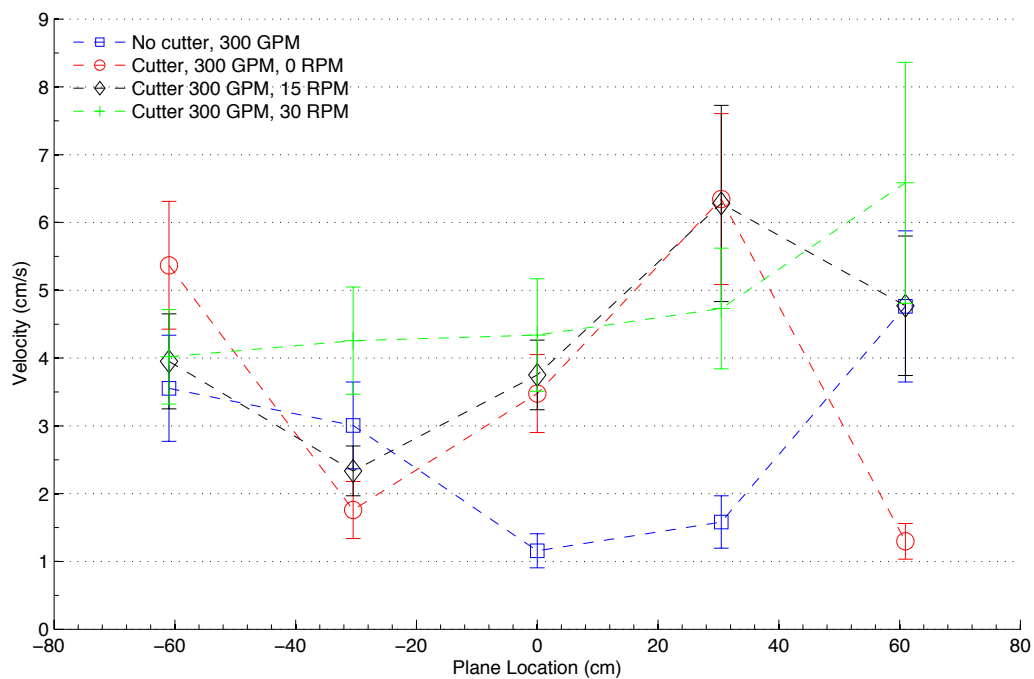


Figure 45: Plane location vs. maximum velocity at various z-planes for the different 300 GPM scenarios.

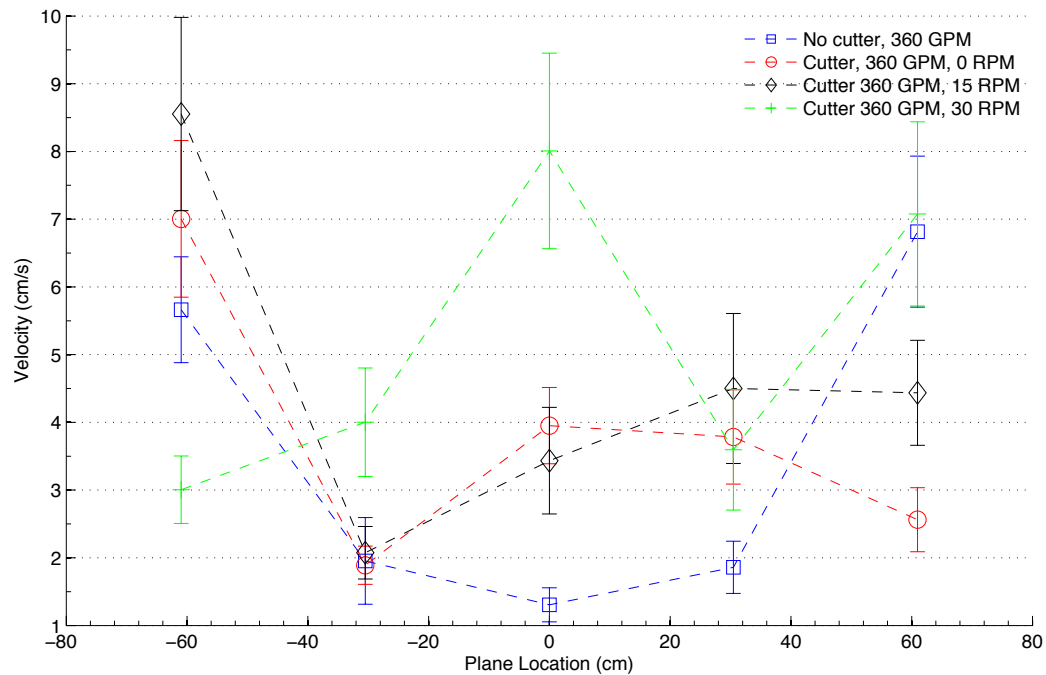


Figure 46: Plane location vs. maximum velocity at various z-planes for the different 360 GPM scenarios.

In order to visualize where the areas of highest velocity were in relation to the cutterhead, points with measured velocities greater than 1.5 cm/s were plotted around the cutterhead in Figure 47. There are clearly three areas to the right of the cutterhead that have higher velocities than other areas. To the left of the cutterhead the points are less clustered but it is possible to once again find two areas that have higher velocities than the surrounding region. The explanation for this clustering behavior is found by examining the cutterhead geometry. The cutterhead used in all tests had five blades without teeth and therefore five areas through which water could flow. So, the cutterhead geometry directly effects where the velocity is the greatest around the cutterhead.

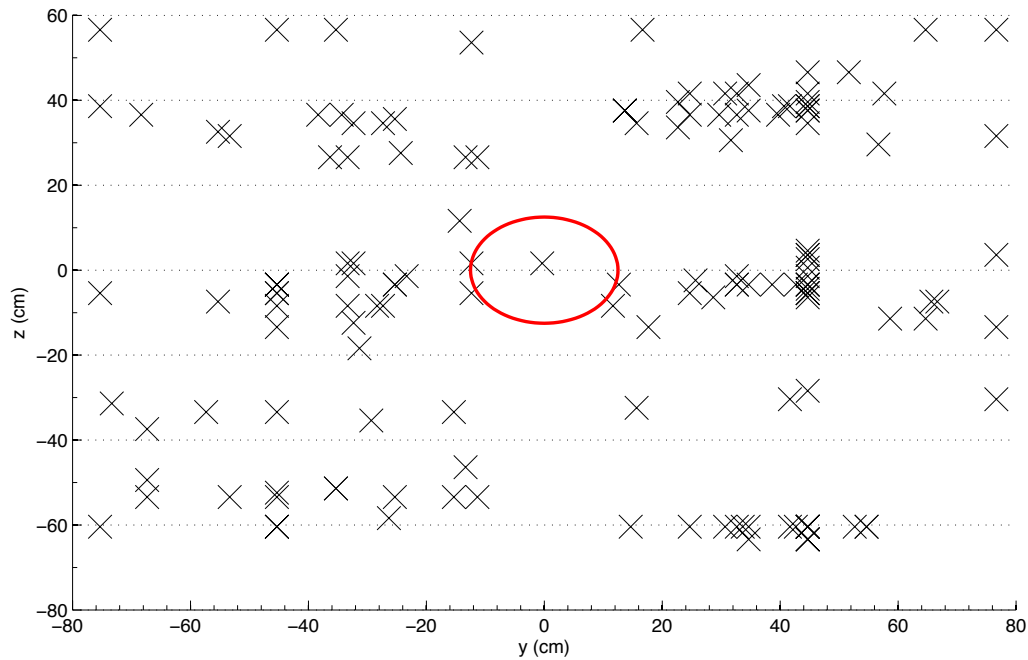


Figure 47: Points with velocity greater than 1.5 cm/s plotted around the silhouette of a cutterhead.

### Region of Influence

There are three aspects of cutter suction head dredging that are important to the dredging process. They are:

1. The velocity field
2. The extent that sediment is picked up after suspension
3. Turbidity generation

The first two aspects are the subjects of this investigation since turbidity generation has been studied in depth in previous experiments. Up until this point the velocity field irrespective of sediment has been examined. The insights gained from the behavior of the velocity field play an important role on how much sediment is picked up. Since a cutterhead works by cutting the sediment

and throwing much of it into suspension around the cutterhead, the velocities needed to take the sediment into the intake are relatively small when compared to the maximum velocity at the intake (Herbich and Brahme, 1986).

In order to pick up the suspended sediment, the vertical component,  $w$ , of the velocity field created by the suction, rotating cutterhead, and swing speed needs to be greater than that of the vertical component of the particle settling velocity,  $w_s$ , of the sediment. There are many methods for calculating the particle settling velocity, mostly empirical. One of the more commonly used equations in dredging was formulated by Schiller (Schiller, 1992):

$$v_t = 134.14(d_{50} - 0.039)^{0.72} \quad (20)$$

where  $v_t$  is the settling velocity,  $d_{50}$  is the median grain diameter in mm. This equation is suitable for use with various sand particle sizes but becomes less accurate as the grain size increases. Usually dredged material consists of a variety of different sediments including silts, clays, sands, and gravels. For this analysis the only material that was used in the calculation of particle settling velocities was sand. Figure 48 shows a plot of the particle settling velocity for various grain diameters ranging from fine sand (0.125 mm or 0.0049 in.) to coarse sand (2.0 mm or 0.7874 in.).

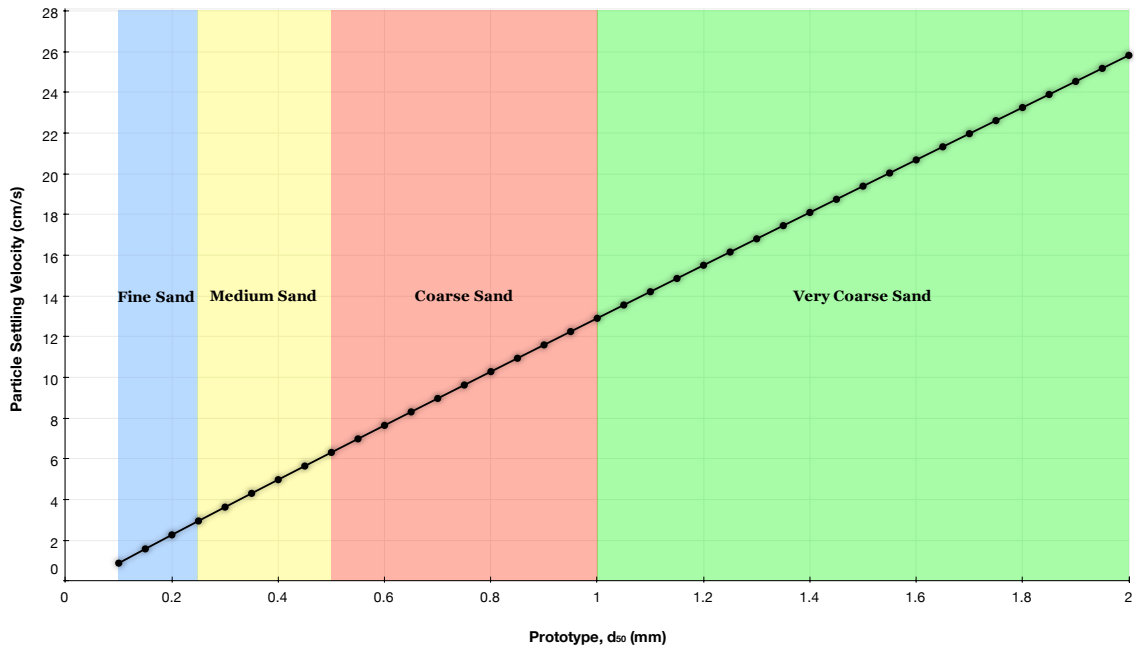


Figure 48: Prototype settling velocities for various prototype sediment diameters.

Since the prototype  $d_{50}$  is used in Figure 48 the grain diameter was scaled down for use with the model dredge. Glover (2002) developed a variation of the scale laws determined by Slotta (1968) and Burger (1997) that took into account Herbich and Brahme's (1986) dimensionless velocity field parameter.

$$\left[ \frac{\omega_{cutter} D_{cutter}}{U_{suction}} \right]_{\text{prototype}} = \left[ \frac{\omega_{cutter} D_{cutter}}{U_{suction}} \right]_{\text{model}} \quad (21)$$

$$\left[ \frac{N_{cutter} D_{cutter}}{V_{settling}} \right]_{\text{prototype}} = \left[ \frac{N_{cutter} D_{cutter}}{V_{settling}} \right]_{\text{model}} \quad (22)$$

Using equation (22) along with known values of the prototype and model intake diameter, prototype and model cutterhead rotation speed, and prototype settling velocity the model settling velocity was calculated. Figure 49 shows model settling velocities for different prototype settling velocities.



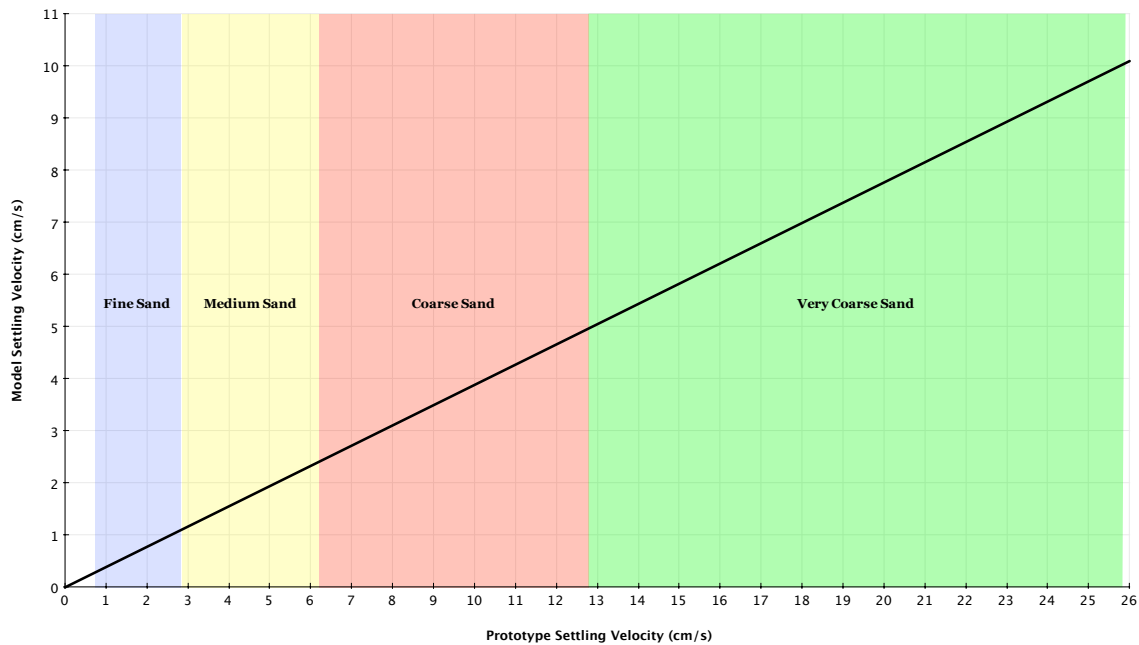


Figure 49: Prototype settling velocity versus model settling velocity. This allows for easy scaling of settling velocities between prototype and model.

Knowing the model particle settling velocities provided a range of velocities that could be compared to those gathered during experimentation. The process for determining the region of influence is as follows: velocity values were plotted at each point for all scenarios, for each view (front, top, and side) a circle or ellipse was found that enclosed all velocities equal to or less than the maximum at each particle size, the regions were then combined into a three dimensional model that allowed for better visualization of the region of influence. Finally, based on the skeleton provided by the region of influence from each view, an ellipsoid was formed that corresponded to the three dimensional region of influence. In each case the direction of the velocity was verified using quiver plots shown in

Appendix 1. This ensured that the sediment was being drawn towards the cutterhead rather than being thrown out. The error is  $\sim 10\text{-}20\text{ cm}$  ( $0.33\text{-}0.66\text{ ft}$ ) due to the spacing of the measurements. Also, in many cases, including all of those determining the region of influence for fine sand, the velocities on either side of the cutterhead were still much greater than those of the particle settling velocities. This means that the region of influence should actually extend further than shown in the results. However, velocities were not measured at distances greater than six suction inlet diameters from the cutterhead. Figure 50 shows the basic shape that the region of influence has. The three characteristic lengths are the major axis diameter, the minor axis diameter, and the outward radius.

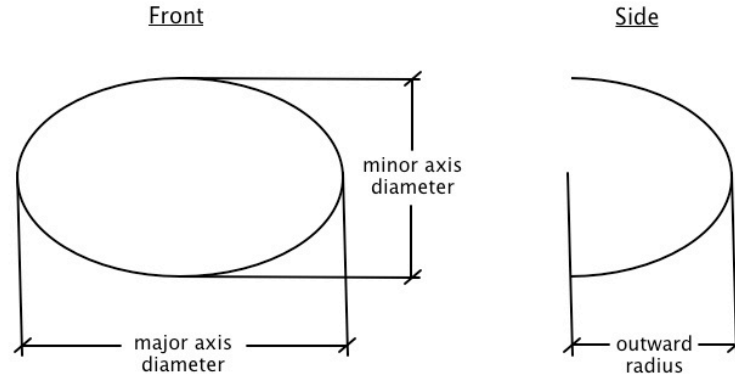


Figure 50: Basic geometry of the region of influence.

Figures 51, 52, and 53 show the region of influence for each scenario based on three different grain sizes (fine, medium, and coarse).

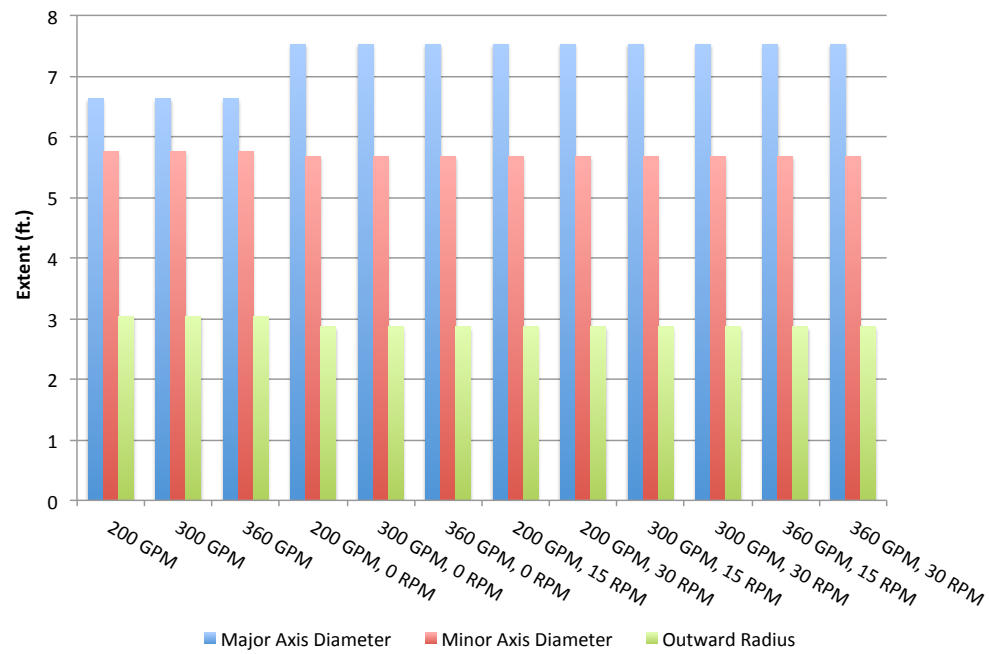


Figure 51: Region of influence dimensions when fine sand is the material being picked up.

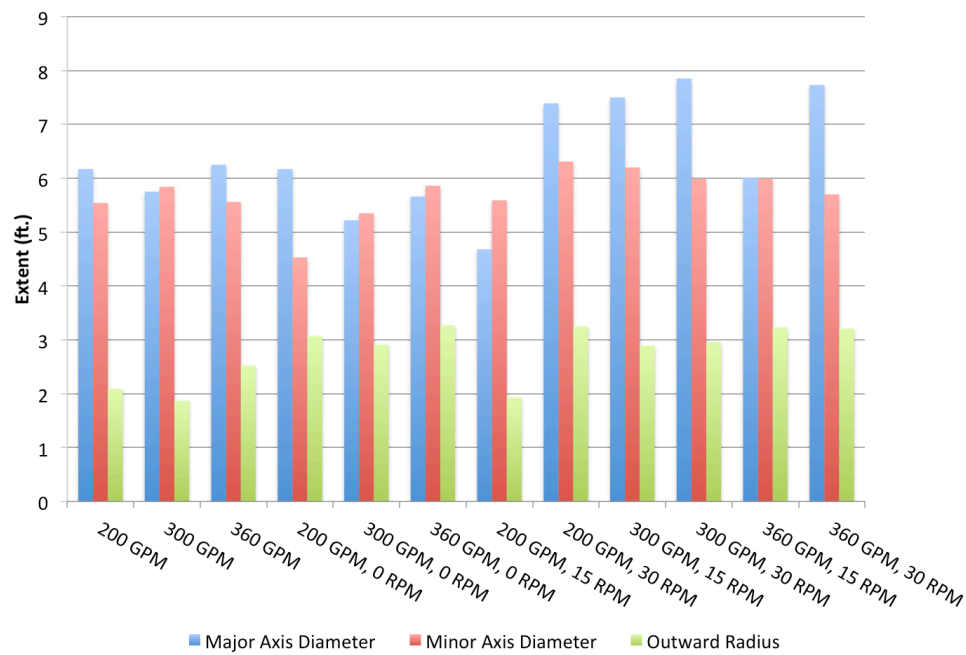


Figure 52: Region of influence dimensions when medium sand is the material being picked up.

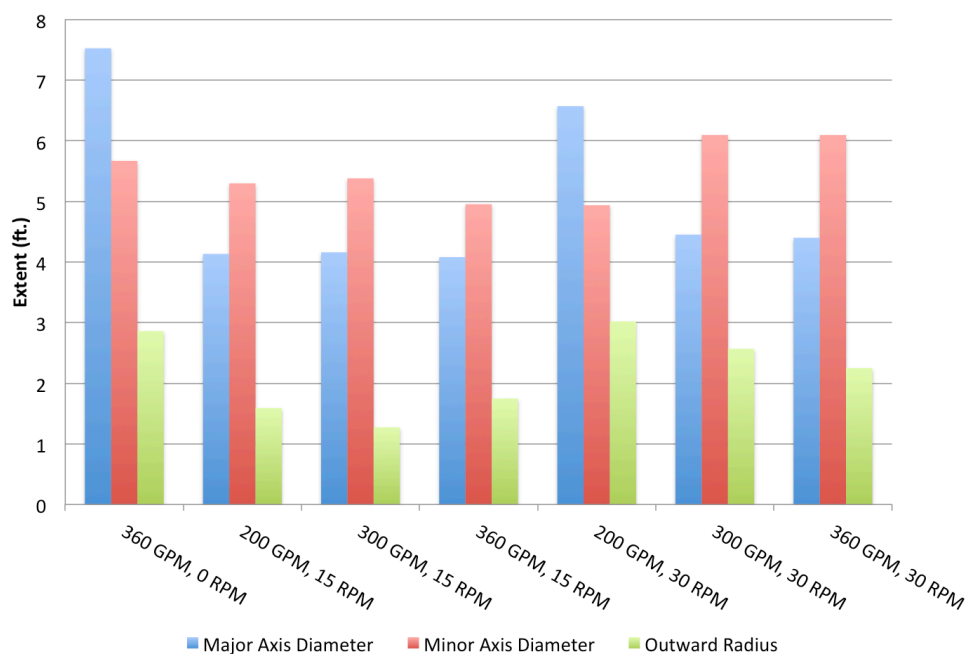


Figure 53: Region of influence dimensions when coarse sand is the material being picked up.

As the grain size increases, a greater flow rate is needed to pull the sediment into the intake. This is why not all scenarios are shown for medium and coarse grain sizes.

A number of observations can be made about the size of the region of influence at each grain size. Fine sand was used first to determine the region of influence. This is the smallest grain size used, so the regions of influence are larger than those for the other grain sizes. In each scenario the region of influence extended outside of the range of measurement. So the results shown in Figure 51 are only a lower bound for the region of influence. To accurately determine the true

region of influence measurements should be taken at points further away from the cutterhead.

Increasing the sediment to a medium grain size of 0.25-0.5 mm (0.0098-0.0197 in.) did not decrease the number of scenarios that were able to pull sediment into the intake. There is a general increase in the size of the region of influence with increasing flow rate as well as with increasing cutterhead rotation speed as seen in Figure 52. Herbich and Brahme (1986) found that velocity field scaling is solely dependent on the volumetric flow rate rather than the velocity at the suction intake - the results show that both the flow rate and the cutterhead rotation speed have a significant impact on the region of influence. The cutterhead rotation speed may have a greater impact since it is directly responsible for the amount of sediment that is thrown into suspension around the cutterhead. It also increases the magnitude of the velocity around the cutterhead which increases the amount of sediment that is pulled into the intake. So, as the cutterhead rotation speed increases so will the amount of sediment. Burger (1997) shows that the production will increase with increasing rotational velocity up to a certain optimum point. This point was found to be between 80-100 RPM depending on the mixture velocity passing through the cutterhead and into the intake.

The outward radius extends ~50% less than the major and minor axes since the cutterhead rotation does not contribute as significantly to the velocity field directly in front of the cutter. In almost all cases for medium sand the major and minor axes were within 0.152 m (0.5 ft) of each other. There is very little change in the outward radius across all scenarios. A slight increase occurs when cutterhead rotation is introduced but the radius remains consistent thereafter. A limit exists to the outward radius in both cases, with and without the cutterhead, that is comparatively small compared to the area of influence above, below, and to either side of the cutterhead. When the cutterhead was not attached to the suction intake the limit was ~0.61 m (2.0 ft) and with the cutterhead the limit was ~0.91-0.99 m (3.0-3.25 ft). That is an approximate 150% increase in the outward radius with the cutterhead attached. This is due to the stationary cutting blades directing more of the suction velocity to the area directly in front of the suction intake.

Once the grain size was increased to coarse sand with median grain diameter of 0.5-1.0 mm (0.0197-0.0394 in) the number of scenarios that had a region of influence significantly decreased. Only half of the scenarios were able to potentially pick up any coarse sand. Figure 53 shows that the only scenarios capable occurred at the highest flow rates and cutterhead rotation speeds.

The volume of each region of influence is shown in Figure 54. The three largest regions of influence by volume were at 200 GPM and 30 RPM, 360 GPM and 30 RPM, and 300 GPM and 30 RPM, respectively. There is a clear decrease in volume as the grain size is increased.

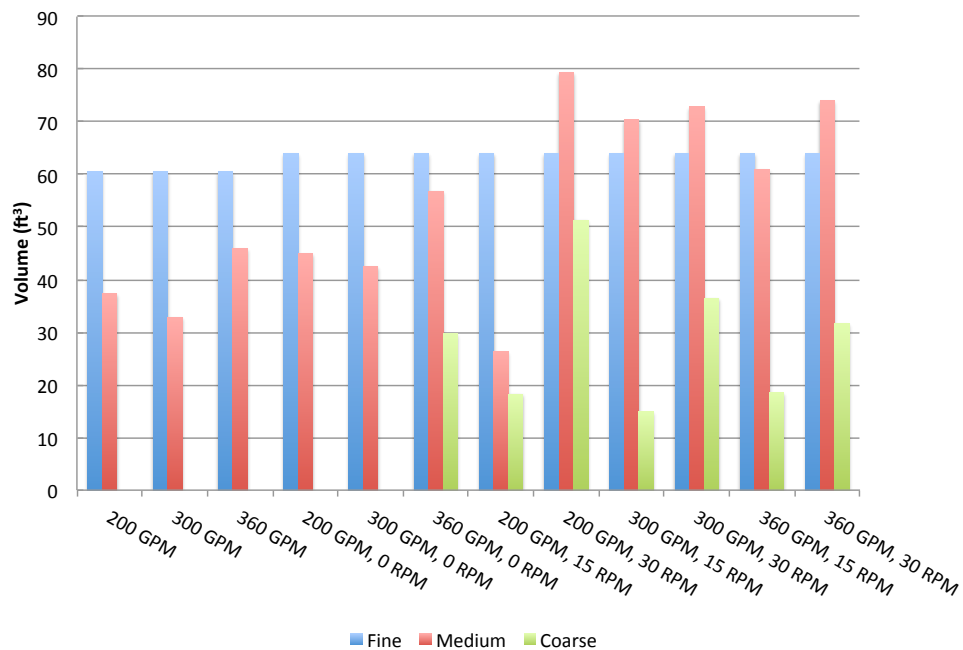


Figure 54: Volume (in ft³) of region of influence for each of the three different grain sizes.

Observations about the size of the region of influence when swinging were difficult to make. The flow field velocities were greater at further distances from the cutterhead, so much so that most regions of influence extended beyond the area of measurement. The regions of influence that were obtained while the ladder was swinging should serve as a guide for later studies.

Figures 55, 56, and 57 show the region of influence for both the overcutting and undercutting scenarios. The settling velocity of coarse sand was used to determine where the boundary of the region of influence would occur. Overall, there was not much variation between the different scenarios. Figure 75 shows that the extent of the region of influence decreases slightly with increasing cutterhead rotation speed. This does not follow the behavior that was observed in the non-swinging scenarios where it was evident that an increase in cutterhead rotation speed would increase the magnitude of the flow field and therefore the region of influence. It is unknown what would cause this behavior; one possibility is the destructive interference between the current generated by swinging and the velocity field created by the rotating cutterhead. The regions of influence ranged from 100 ft<sup>3</sup> to 190 ft<sup>3</sup> while undercutting and from 100 ft<sup>3</sup> to 225 ft<sup>3</sup> while overcutting.



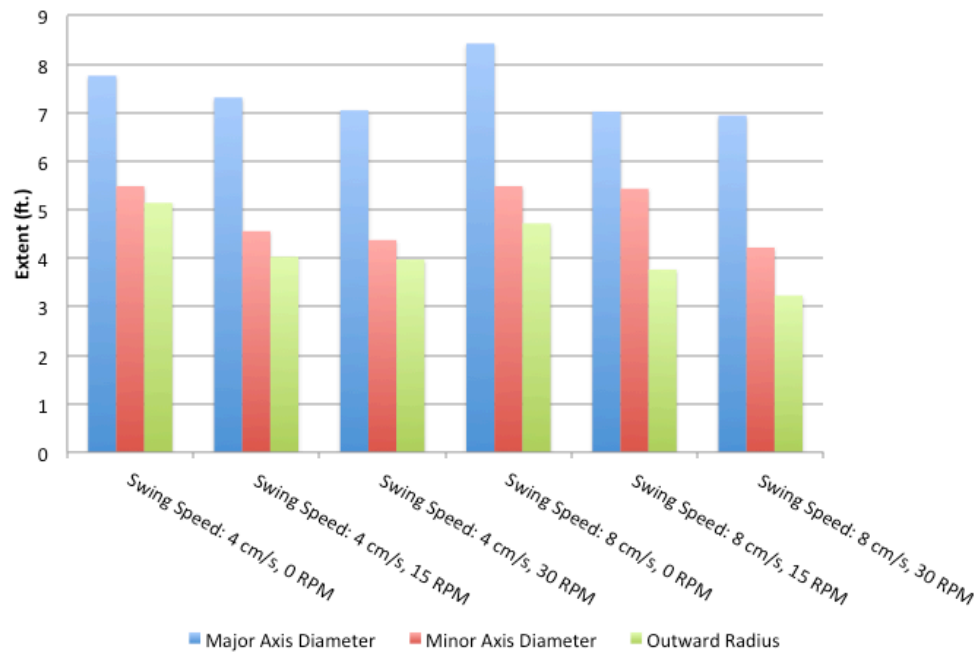


Figure 55: Region of influence dimensions when coarse sand is the material being picked up and the cutterhead is overcutting.

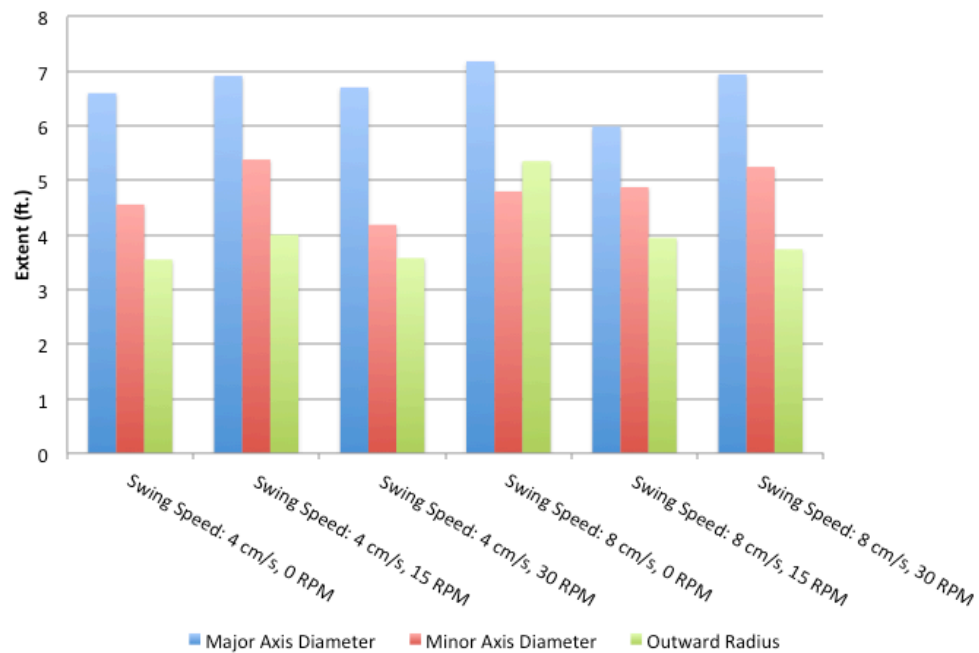


Figure 56: Region of influence dimensions when coarse sand is the material being picked up and the cutterhead is undercutting.

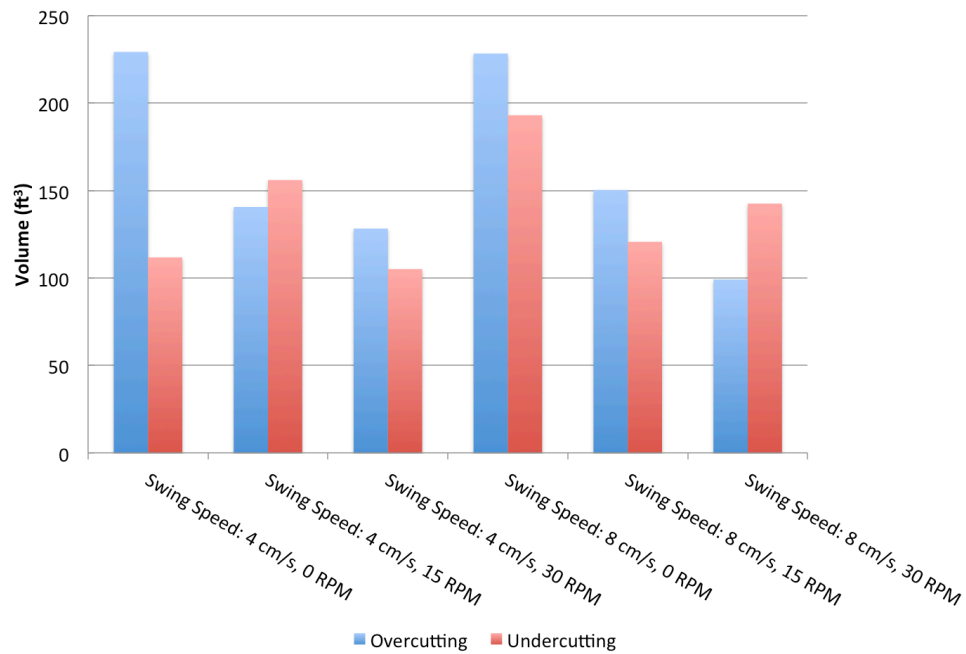


Figure 57: Region of influence volume when coarse sand is the material being picked up.

Very coarse sand (1mm-2mm) was used in the next analysis; its settling velocity was between 5 cm/s and 10 cm/s depending on the exact grain size.

Figures 58, 59, and 60 show the results when very coarse sand was the sediment being picked up. Similar to when coarse sand was being picked up, the region of influence decreased with increasing cutterhead rotation speed. The regions of influence ranged from 130 ft<sup>3</sup> to 225 ft<sup>3</sup> while undercutting and from 100 ft<sup>3</sup> to 175 ft<sup>3</sup> while overcutting.

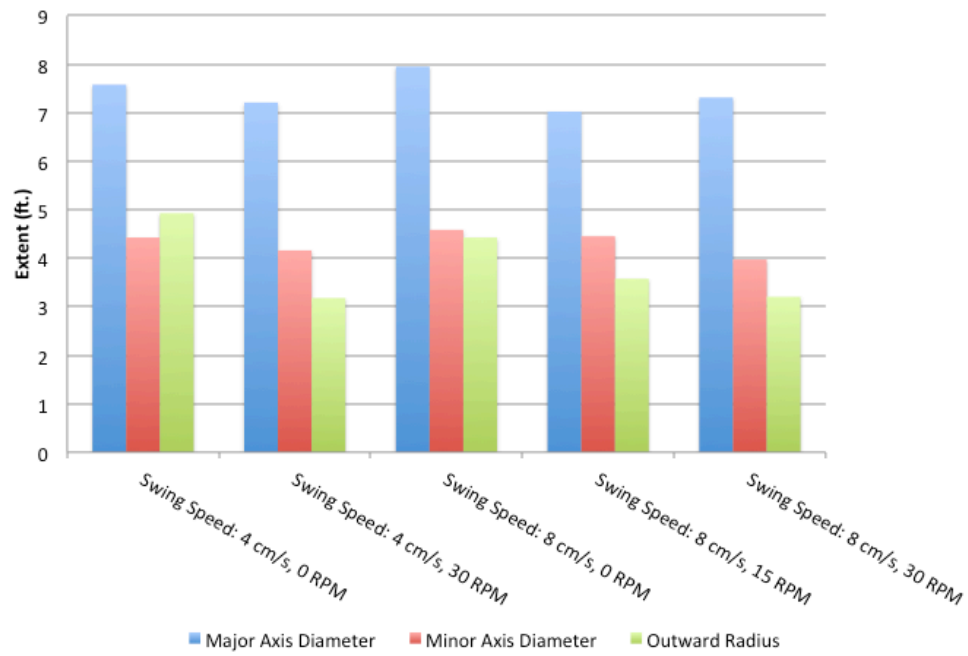


Figure 58: Region of influence dimensions when very coarse sand is the material being picked up and the cutterhead is overcutting.

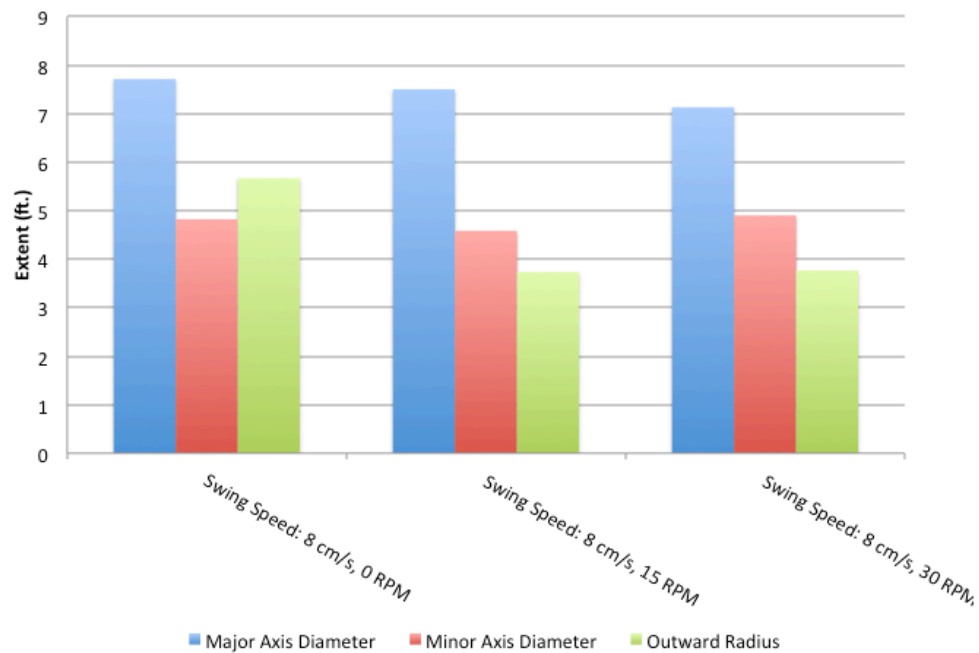


Figure 59: Region of influence dimensions when very coarse sand is the material being picked up and the cutterhead is undercutting.

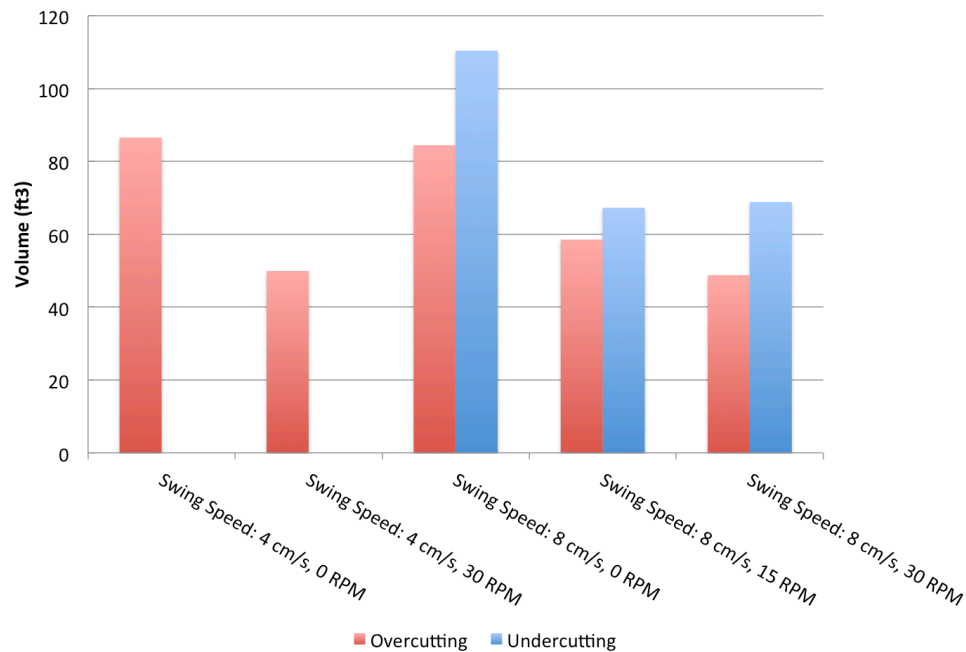


Figure 60: Region of influence volume when very coarse sand is the material being picked up.

### Comparison to Herbich and Brahme (1986)

Herbich and Brahme (1986) conducted much of the initial research around the complex flow surrounding a cutterhead during operation. Together and separately great progress was made in the investigation of velocity flow fields, sediment resuspension around the cutterhead, and factors influencing turbidity near the cutterhead and how to reduce it.

Hydraulic model studies helped to show that the dimensionless velocity field parameter,  $Q/r^2V$ , was valid and could be used to predict velocities around the cutterhead fairly accurately. Additionally, their measurement of velocities around a three dimensional cutterhead served as a basis for this thesis. So, it is

appropriate to draw comparisons between the results they obtained and those derived from the data collected for this thesis.

Their experiments took place in a steel tank measuring 2.4 m (8 ft) long, 1.2 m (4 ft) wide, and 1.2 m (4 ft) deep. Two cutterheads, similar to the one shown in Figure 11, were used with scales of 1:12.25 and 1:2.45. One difference in their setup was the orientation of the suction intake. It was positioned at  $90^\circ$  to the horizontal, whereas the ladder arm detailed in Chapter 3 was at  $30^\circ$  below the horizontal. Herbich and Brahme (1986) also ran tests at  $60^\circ$  to the horizontal and determined that the angle of the suction intake did not have any significant effect on the flow field or velocities. Another difference in their experimental setup is the measurement technique used to record velocities at various points around the cutterhead. At the time acoustic Doppler velocimetry was not widely available so velocities were measured using a combination of a micropropellor turbulence and velocity flow meter, a hot-film anemometer, and color dyes. ADVs are considered to be much more accurate than these methods and were used in this experiment for that reason.

In their investigation, velocity fields were determined for three different pipe diameters at three different heights above the bottom of the tank in contrast to varying the flow rate and cutterhead rotation speed. A description of the exact

pipe diameters and heights was not included in their paper so replicating their results exactly is not possible.

The dimensionless number,  $Q/r^2V$ , was used in conjunction with the velocity data to create a plot for different values of  $x/h$  and  $r/H$  where  $r$  is the radial distance from the center of the pipe,  $x$  is the vertical distance above the bottom, and  $H$  is depth of water in the tank. The velocity field parameter was averaged over all the conditions in the experiment so that the results could be consolidated onto one plot. Once again this creates a problem when trying to compare data, however, orders of magnitude can be observed and used for comparison. Figure 61 shows the contours of  $Q/r^2V$  from Herbach and Brahme's (1986) results.

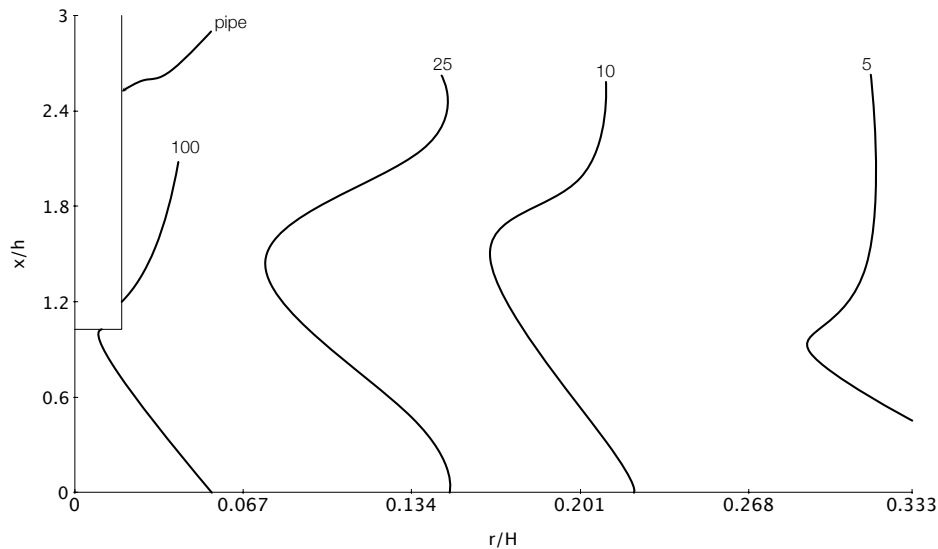


Figure 61: Results from Herbach and Brahme's paper (1986). The dimensionless velocity field parameter plotted for various values of  $r/H$  and  $x/h$ .

Figures 62, 63, 64, and 65 show  $Q/r^2V$  plotted for various values of  $x/h$  and  $r/H$  for the data collected for this thesis. Each plot shows the average of  $Q/r^2V$  for the three different flow rates at a different cutterhead rotation speed as well as with no cutterhead attached. The suction inlet and cutterhead are located at  $r/H=0$  and  $x/h=0$ .

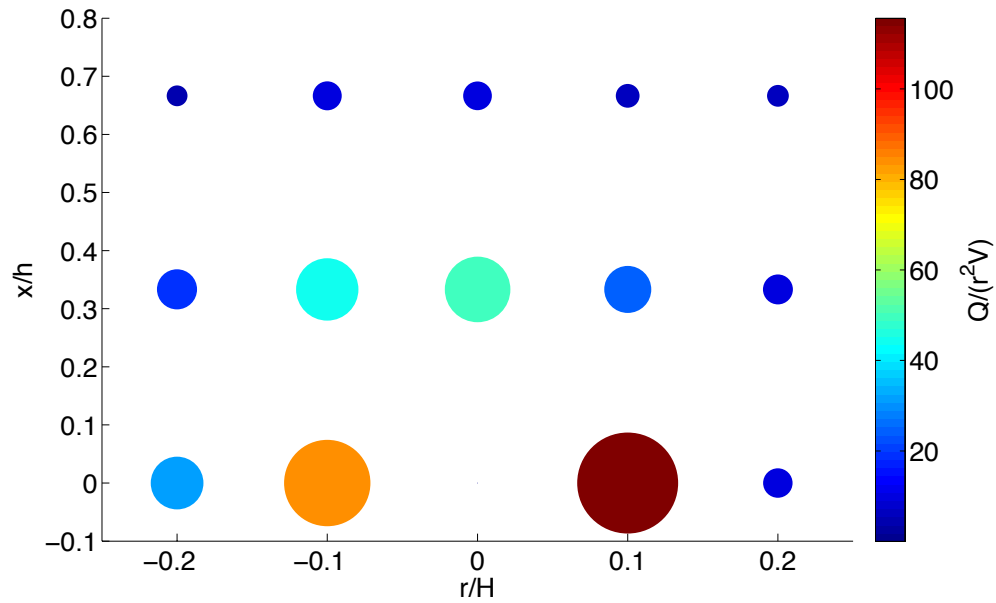


Figure 62: The average of  $Q/r^2V$  for three different flow rates (200, 300, 360) with no cutterhead attached plotted for various values of  $r/H$  and  $x/h$ .

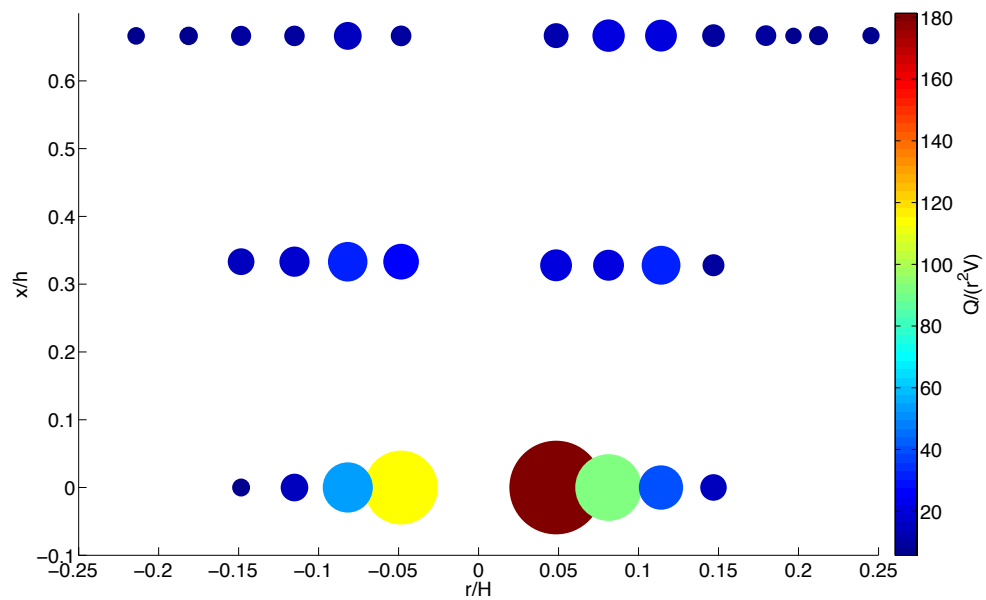


Figure 63: The average of  $Q/r^2V$  for three different flow rates (200, 300, 360) with cutterhead rotation speed of 0 RPM plotted for various values of  $r/H$  and  $x/h$ .

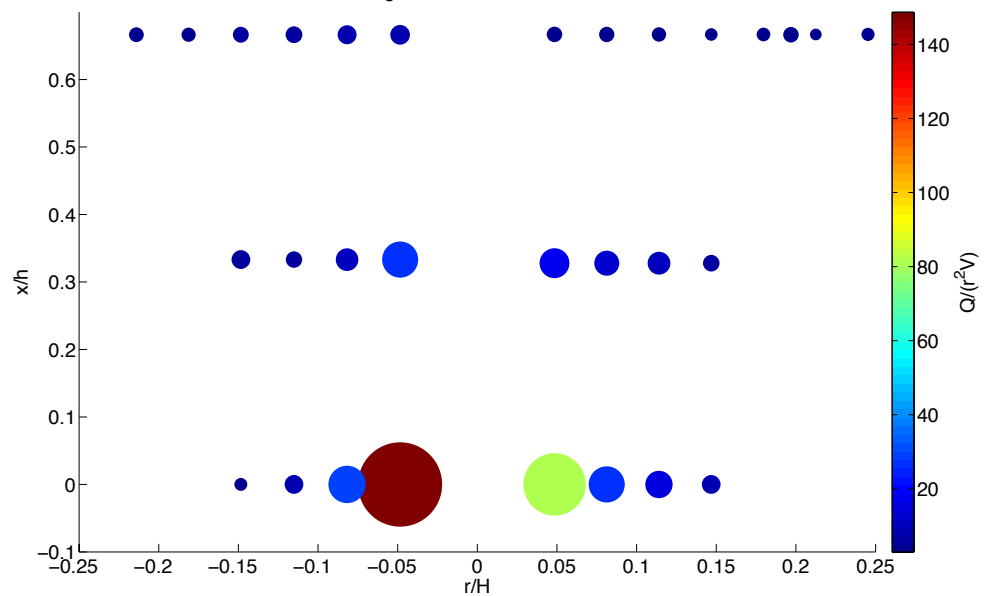


Figure 64: The average of  $Q/r^2V$  for three different flow rates (200, 300, 360) with cutterhead rotation speed of 15 RPM plotted for various values of  $r/H$  and  $x/h$ .



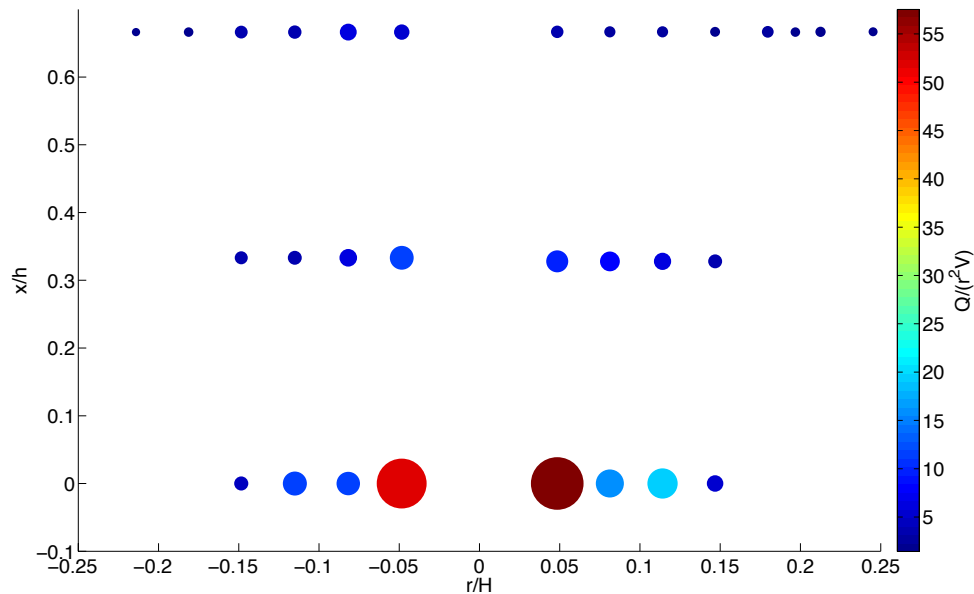


Figure 65: The average of  $Q/r^2V$  for three different flow rates (200, 300, 360) with cutterhead rotation speed of 30 RPM plotted for various values of  $r/H$  and  $x/h$ .

Herbich and Brahme's results show that higher values of  $Q/r^2V$  are observed near the suction intake. The dominant factor being that the velocity field parameter is inversely proportional to the radial distance from intake. Similarly, there is a clear increase in the velocity field parameter near the cutterhead in the three previous plots. The magnitudes are larger than those shown in the Herbich and Brahme, at times almost 200% greater, but this is to be expected since the flow rate is much greater.

The values shown in Figure 62, 63, 64, and 65 are very similar despite the difference in cutterhead rotation speed. This furthers the idea that the velocity field is only dependent on the volumetric flow rate through the suction pipe.

By using equation (23) the velocity fields used in the three previous plots can be scaled to the approximate flow rate and suction diameter used in Herbich and Brahme's study.

$$\left[ \frac{Q}{D^2 V} \right]_{\text{prototype}} = \left[ \frac{Q}{D^2 V} \right]_{\text{model}} \quad (23)$$

This is similar to the scaling law that Glover (2002) used based on the dimensionless parameter developed by Herbich and Brahme (1986). Glover replaced the field velocity with the settling velocity of the sediment and the radial distance from the suction with suction intake diameter. Here, only the radial distance is replaced. Replacing the radial distance with the suction diameter ensures that there is geometric scaling of the flow field. Figures 66, 67, 68, and 69 show the values of the dimensionless velocity field parameter in Figures 62, 63, 64, and 65 scaled down to 55 GPM and a suction diameter of .0279 m (1.1 in).

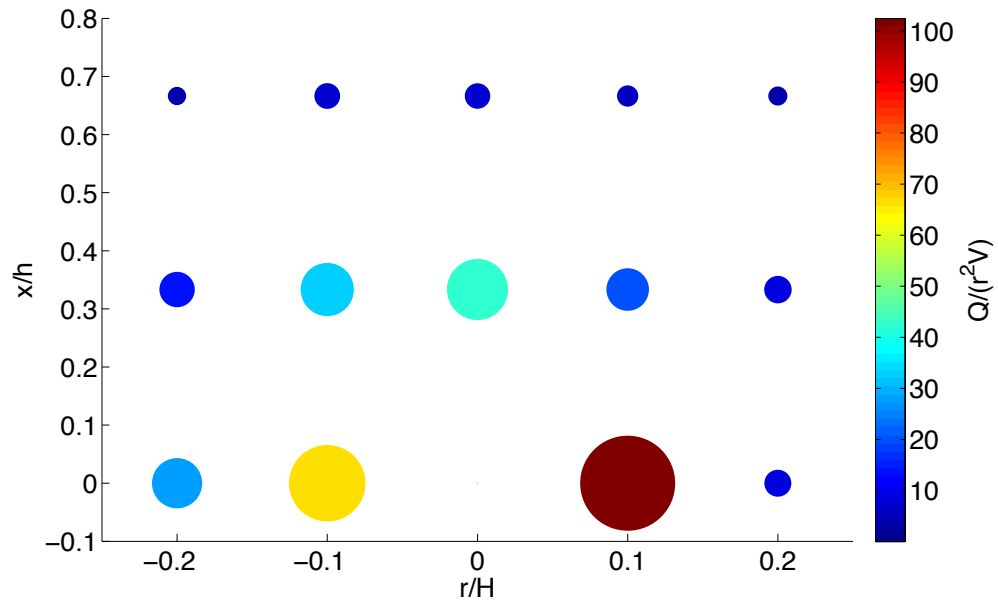


Figure 66: The scaled down (to  $Q=55$  GPM and  $D=1.1$  in) average of  $Q/r^2V$  for three different flow rates (200, 300, 360) with no cutterhead attached plotted for various values of  $r/H$  and  $x/h$ .

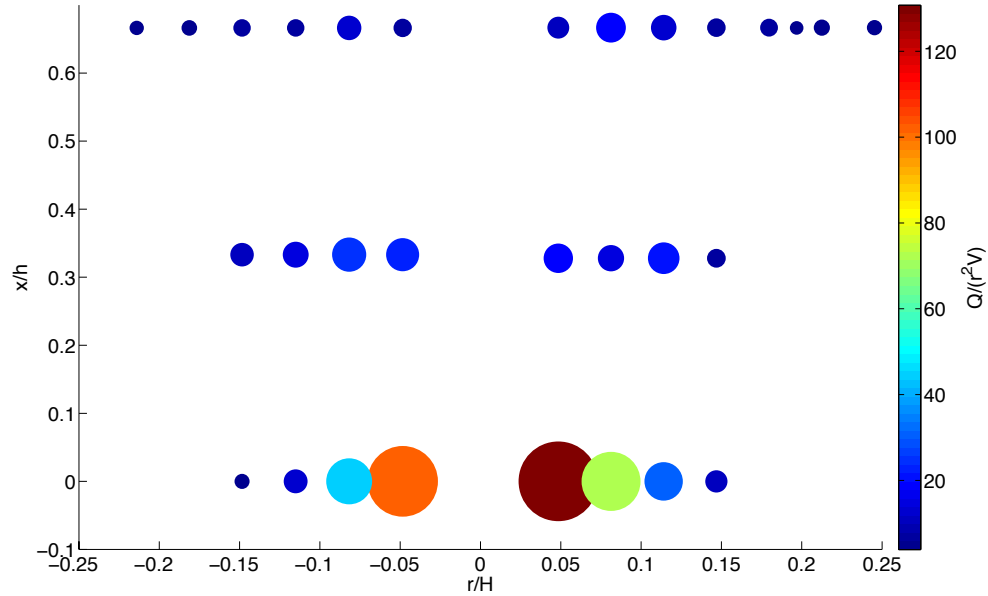


Figure 67: The scaled down (to  $Q=55$  GPM and  $D=1.1$  in) average of  $Q/r^2V$  for three different flow rates (200, 300, 360) with cutterhead rotation speed of 0 RPM plotted for various values of  $r/H$  and  $x/h$ .

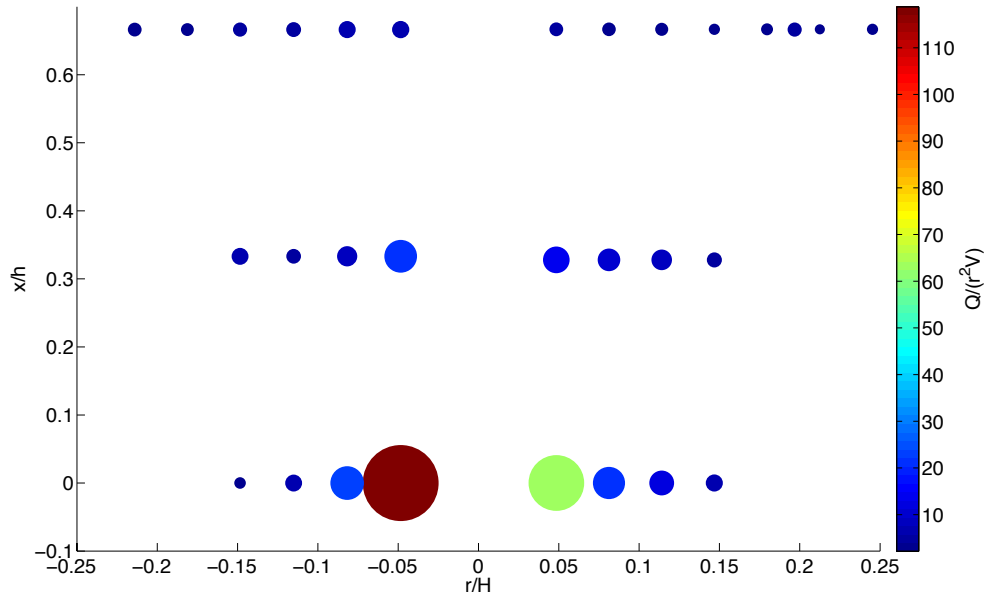


Figure 68: The scaled down (to  $Q=55$  GPM and  $D=1.1$  in) average of  $Q/r^2V$  for three different flow rates (200, 300, 360) with cutterhead rotation speed of 15 RPM plotted for various values of  $r/H$  and  $x/h$ .

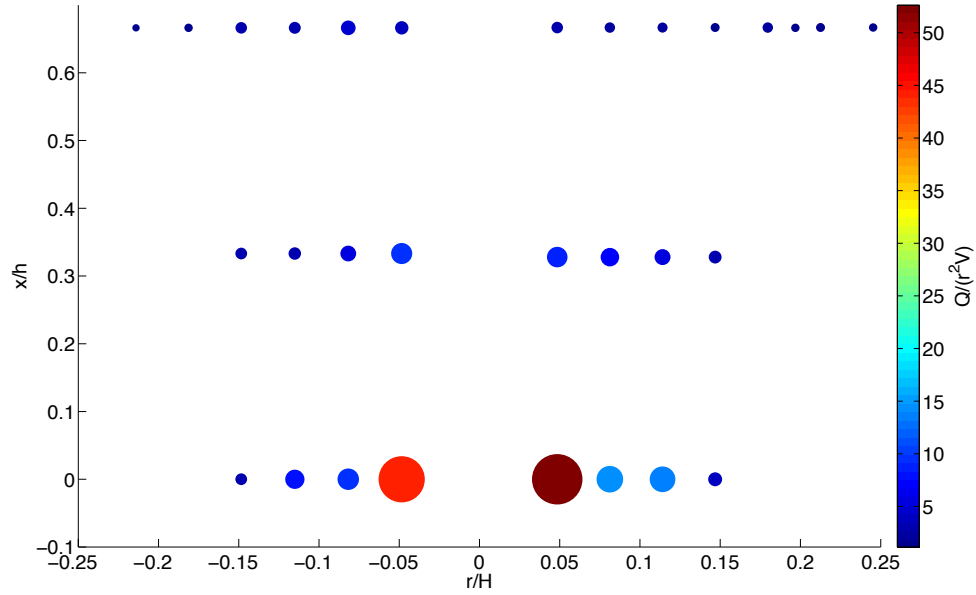


Figure 69: The scaled down (to  $Q=55$  GPM and  $D=1.1$  in) average of  $Q/r^2V$  for three different flow rates (200, 300, 360) with cutterhead rotation speed of 30 RPM plotted for various values of  $r/H$  and  $x/h$ .

As expected the values are smaller and very similar to those in Figure 61. The discrepancy between the values is likely caused by the use of averaged values for  $Q/r^2V$ .

### **Dimensional Analysis**

Up to this point the focus has been on the model dredge; the dredge that is a scaled down model of the prototype, full size dredge. Chapter 3 went into detail describing the different operating parameters of the dredge at the Haynes Coastal Engineering Laboratory. That dredge was designed at a 1:6 scale to a full size dredge operating with a 61 cm (24 in.) suction diameter, 183 cm (72 in.) cutterhead diameter rotating at 40 RPM, a pump capable of pumping 30,000 GPM of slurry at a specific gravity of 1.3, a swing velocity of 50.8 cm/s (1.67 ft/s), and operating with sediment ranging from fine to coarse sand (Glover, 2002). In the design of the model dredge Glover used hydraulic scaling based on the sediment pick-up behavior, kinematic scaling based on the Froude number, and dynamic scaling based on the cutting forces. Since the model has been scaled in each of the three ways, it should pick up a geometrically similar volume of material to the full size dredge.

The region of influence for the prototype dredge is of interest to dredging companies and their dredge operators. In order to scale the geometry of the region of influence the velocity field geometry and velocity field magnitudes

must be scaled. This requires that the ratio of the velocity field geometry to the suction diameter for the prototype must equal that of the model and that the ratio of the velocity field magnitudes to the settling velocity for the prototype must be equal to that of the model (Glover 2002). In other words:

$$\left[ \frac{D_{ROI}}{D_{suction}} \right]_{\text{prototype}} = \left[ \frac{D_{ROI}}{D_{suction}} \right]_{\text{model}} \quad (24)$$

$$\left[ \frac{U}{V_{\text{settling}}} \right]_{\text{prototype}} = \left[ \frac{U}{V_{\text{settling}}} \right]_{\text{model}} \quad (25)$$

In the above equations  $D_{ROI}$  is the diameter of the region of influence,  $D_{suction}$  is the diameter of the suction intake,  $U$  is the velocity at a point, and  $V_{\text{settling}}$  is the settling velocity of particle. Using equation (26) the geometry of the region of influence can be directly calculated.

$$D_{ROI, \text{prototype}} = \left( \frac{D_{\text{suction, prototype}}}{D_{\text{suction, model}}} \right) \cdot D_{ROI, \text{model}} \quad (26)$$

So, with a 1:6 scale between model and prototype the region of influence for the prototype dredge will be 6x greater in the horizontal, vertical, and outward directions. Figures 70, 71, and 72 show the geometry of the region of influence for various particle sizes.

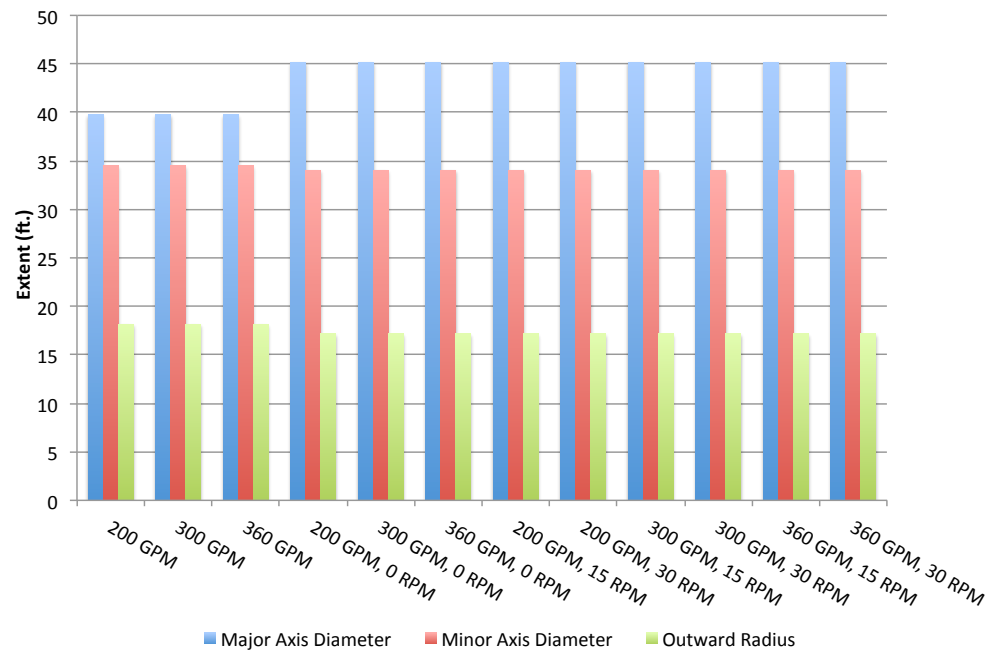


Figure 70: Geometry of the prototype region of influence when the sediment is fine sand.

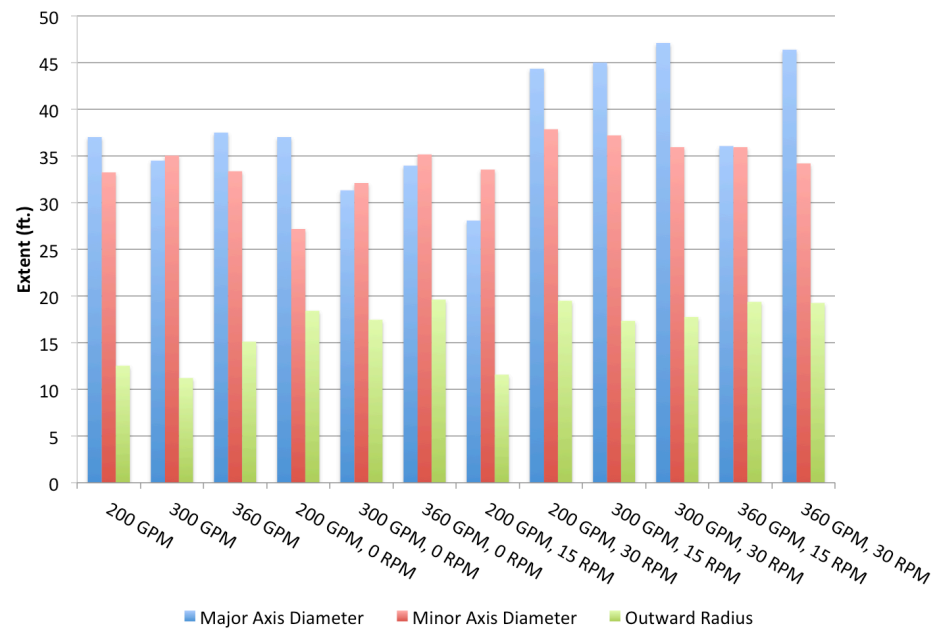


Figure 71: Geometry of the prototype region of influence when the sediment is medium sand.

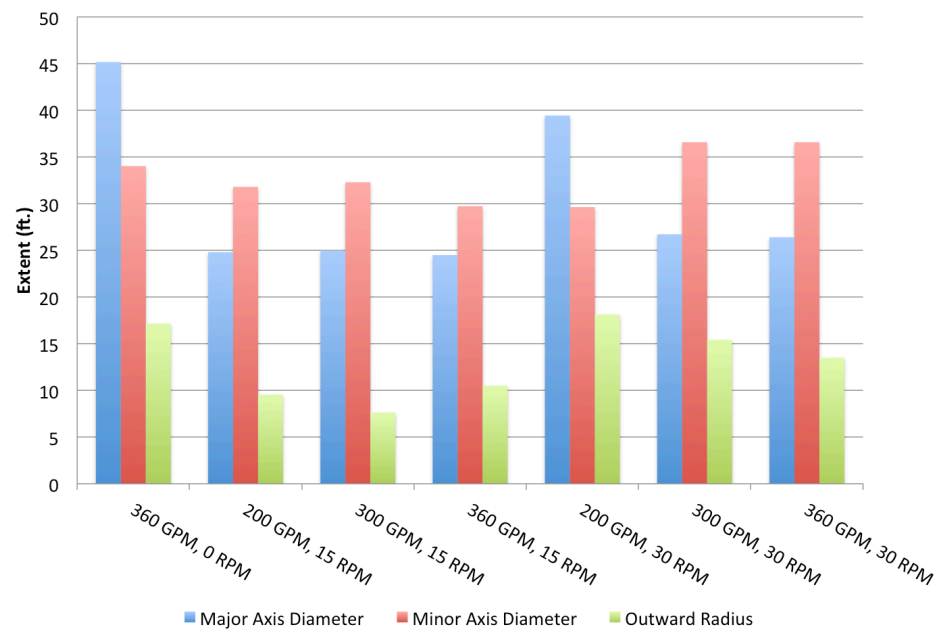


Figure 72: Geometry of the prototype region of influence when the sediment is coarse sand.



In Figure 73 the volumes of each region of influence are shown for the various scenarios and sediment types.

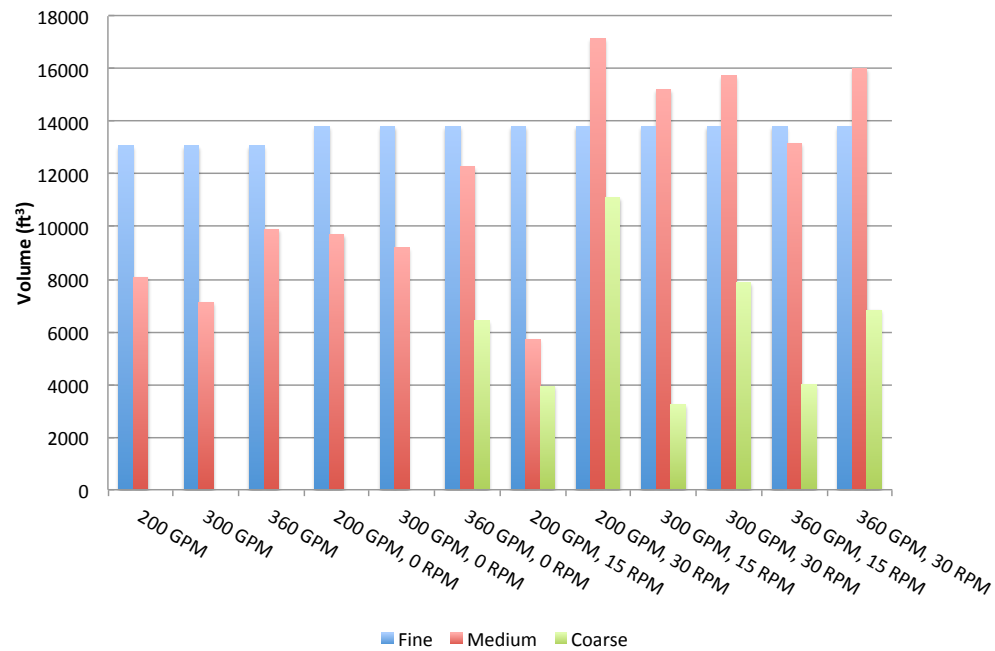


Figure 73: Volume (in ft<sup>3</sup>) of the prototype region of influence for each of the three different grain sizes.

## **CHAPTER V**

### **CONCLUSIONS**

By using the results presented in this thesis, dredge operators, dredging engineers, and researchers will have a better understanding of the behavior of the flow field around a cutterhead as well as the region of influence. The suction flow rate, cutterhead rotation speed, and swing speed each caused increases in the magnitude of the velocity around the suction inlet.

Analysis of the suction flow rate helped visualize how the flow affected the region of influence around the cutterhead. It was found that the maximum velocities are directly proportional to the flow rate. These velocities caused by the suction, cutterhead rotation, swing speed, or a combination of the three occurs very near the cutterhead. At a distance of 60 cm in front of the cutterhead tip the maximum velocities were approximately half that of those in the nearest plane to the cutterhead. At lower flow rates the addition of a stationary cutterhead did not affect the velocities at all. This behavior was observed by Herbich and Brahme (1986). As the distance increased from the cutterhead tip to the plane of measurement there was a decrease in correlation between the flow rate and maximum velocity. However, at higher cutterhead rotation speeds the maximum velocities remained steady across all planes of measurement.

Cutterhead rotation was added to determine its effects on the flow field and region of influence. At lower flow rates the cutterhead rotational speed did not correlate to maximum velocities near the cutterhead. So increasing from 0 RPM to 30 RPMs did not increase the velocities when the flow rate was 200 GPM. At higher flow rates, increasing the cutterhead rotational speed to 30 RPMs caused the maximum velocities to remain steady as the distance increased between the cutterhead and point of measurement. At some point the maximum velocities will decrease, however that point was beyond the scope of measurement. In overcutting situations the highest velocities occurred at the leading edge of the cutterhead. However, when the cutterhead is not rotating the highest velocities occur at the trailing edge of the cutterhead.

The most important aspect of this thesis pertained to the determination of the region of influence around the cutterhead. It was found that the region of influence was nearly symmetrical around the cutterhead, but the shape could more accurately be described as an ellipsoid. The volumes of the regions of influence ranged from 10 ft<sup>3</sup> (0.283 m<sup>3</sup>) to 80 ft<sup>3</sup> (2.27 m<sup>3</sup>) for the model dredge and from 2,250 ft<sup>3</sup> (63.70 m<sup>3</sup>) to 17,000 ft<sup>3</sup> (481.40 m<sup>3</sup>) for the prototype dredge. The region of influence when picking up fine sand was the largest. There was a 20% reduction in the major and minor axes of the region and 33% reduction in the outward radius when the grain size was increased to medium sand. Finally, as the grain size was increased further to a coarse sand the volumes of the

regions of influence decreased by approximately 50%. Analysis of the region of influence with the addition of two swing speeds was also conducted. However, the results were inconclusive and further studies should be performed to better understand how swing speed influences the velocity field around the cutterhead.

Herbich and Brahme (1986) provided a basis for this thesis and comparisons were made to their results. Plots of  $Q/r^2V$  were similar to and showed the same behavior. Herbich and Brahme showed that the velocity field is only dependent on the volumetric flow rate through the suction pipe. Scaling the suction pipe diameter and flow rate down to those used by Herbich and Brahme yielded very similar values.

The flow around a cutterhead is extremely complex and more detailed analysis is needed in the future. The addition of each different operating parameter, suction flow, cutterhead rotation, and swing speed, increases this complexity.

A greater extent of measurements needs to be taken in order to determine the true region of influence for all flow rates, cutterhead rotation speeds, and swing speeds. The theoretical region of influence used to determine the extent of the measurements for this thesis was too small and should be increased. Similarly, a higher resolution of data points could be collected. This would help determine

more accurate dimensions for the region of influence as well as make it simpler to use visualization software that require many points of measurement.

The addition of sediment to each scenario would better simulate real world dredging conditions and possibly validate any velocity measurements.

Expanding the methods of velocity gathering could help achieve this. Using PIV (particle image velocimetry) and high-speed cameras might provide a more accurate model of the region of influence.

## REFERENCES

- Batchelor, G. K. (1967). *An Introduction to Fluid Dynamics*. Cambridge University Press, New York.
- Brahme, S.B. (1983), *Environmental Aspects of Suction Cutterheads*. Ph.D. Dissertation, Texas A&M University, College Station.
- Brahme, S.B., and Herbich, J.B. (1986). Hydraulic Model Studies for Suction Cutterheads. *Journal of Waterway, Port, Coastal and Ocean Engineering*, ASCE, Vol. 112, No. 5, pp. 590-607.
- Burger, M. (2003). *Mixture Forming Processes in Dredge Cutterheads*. Ph.D. Dissertation, Delft University of Technology, Delft, The Netherlands.
- Burger, M. den, (1998). *Meting Verblijftijden Deeltjes in Snijkop (Measurements of Particle Residence Times in a Cutter Head)*. Section of Dredging Technology, Report nr.99.3.GV.5127, Delft University of Technology, Delft, The Netherlands. (in Dutch).

- Dekker, M. A., Burger, M. den, Kruijt, N. P., and Vlasblom, W. J. (2003). Experimental and Numerical Investigation of Cutter Head Dredging Flows. *Journal of Waterway, Port, Coastal and Ocean Engineering, ASCE*, Vol. 129, No. 5, pp. 203-209.
- Glover, G.J. (2002) *Laboratory Modeling of Hydraulic Dredges and Design of Dredge Carriage for Laboratory Facility*. Master's Thesis, Ocean Engineering Program, Civil Engineering Department, Texas A&M University, College Station, TX.
- Goring, D.G., and Nikora, V.I. (2002). Despiking acoustic doppler velocimeter data. *Journal of Hydraulic Engineering*. Vol. 128, No. 1, pp. 117-126.
- Henriksen, John Christopher (2009). *Near-Field Sediment Resuspension Measurement and Modeling for Cutter Suction Dredging Operations*. Ph.D. dissertation, Texas A&M University.
- Herbich, J.B. (2000). *Handbook of Dredging Engineering*, Second Edition. McGraw-Hill, New York, NY.

Kruyt, N.P., van Esch, B.P.M., and Jonker, J. B. (1999). A superelement-based method for computing unsteady three- dimensional potential flows in hydraulic turbomachines. *Communications in Numerical Methods in Engineering*, Vol. 15 No. 6, pp. 381–397.

Mori, N., T. Suzuki, and S. Kakuno (2007). Noise of acoustic Doppler velocimeter data in bubbly flows. *Journal of Engineering Mechanics*, Vol. 133, pp. 122-125.

NORTEK AS. (2009). *ADV Operation Manual*. NORTEK AS, Oslo, Norway.

Pope, S. B. (2000). *Turbulent Flows*. Cambridge University Press, New York.

Schiller, R.E. Jr. (1992). Sediment Transport in Pipes. Chapter VI, *Handbook of Dredging Engineering*, Editor: J.B. Herbich, McGraw-Hill: New York.

Slotta, L.S. (1968). *Flow Visualization Techniques Used in Dredge Cutterhead Evaluation*. Proceedings of the 1968 World Dredging Congress, WODCON II, Rotterdam, The Netherlands, pp. 56-77.

Turner, T. M. (1984). *Fundamentals of Hydraulic Dredging*. Cornell Maritime Press, Centreville, MD. pp. 215.



Voulgaris, G., and Trowbridge, J.H. (1998). Evaluation of the acoustic doppler velocimeter (ADV) for turbulence measurements. *Journal of Atmospheric and Oceanic Technology*, Vol. 15, No. 1, pp. 272-289.

Wahl, T.L., (2003). Discussion of Despiking acoustic Doppler velocimeter data. *Journal of Hydraulic Engineering*, Vol. 129, No. 6, pp. 484-488.

Young, D.R. (2009). *Force on Laboratory Model Dredge Cutterhead*. Master's Thesis, Ocean Engineering Program, Civil Engineering Department, Texas A&M University, College Station, TX.

## APPENDIX A

### QUIVER PLOTS

As an aid to the figures in the Flow Rate Effects and Rotation Effects sections, quiver plots were generated to determine the direction of the velocity at each measurement point. They are included below.

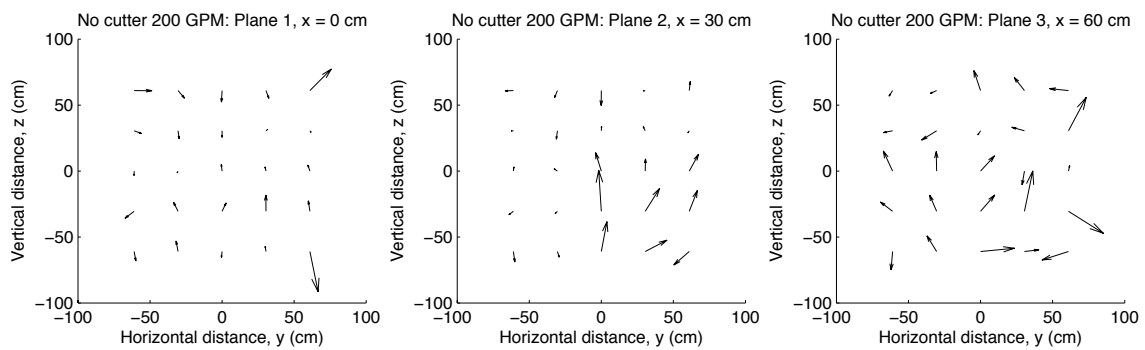


Figure 74: Quiver plots in the y-z plane for the scenario with no cutterhead attached and 200 GPM.

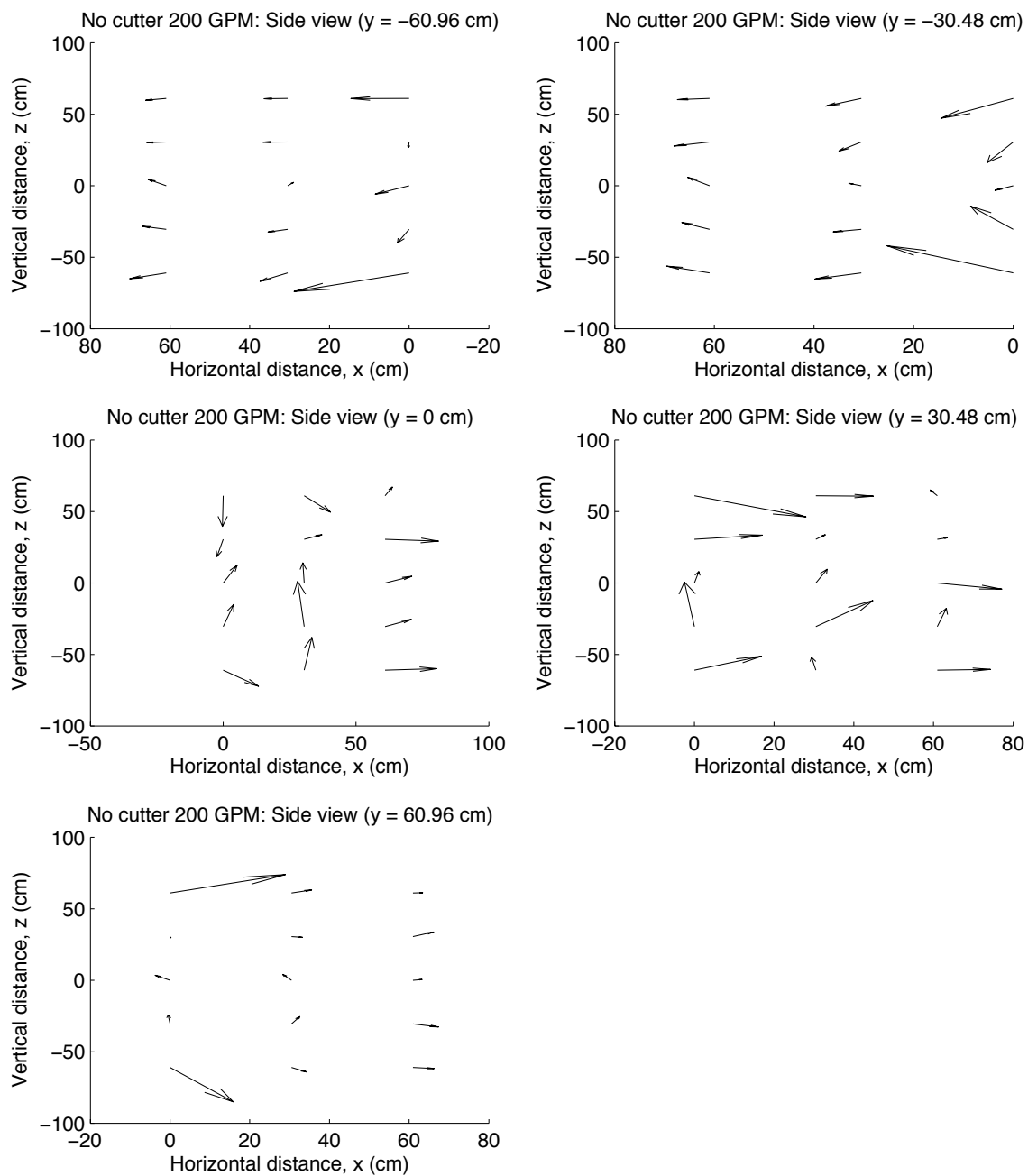


Figure 75: Quiver plots in the x-z plane for the scenario with no cutterhead attached and 200 GPM.

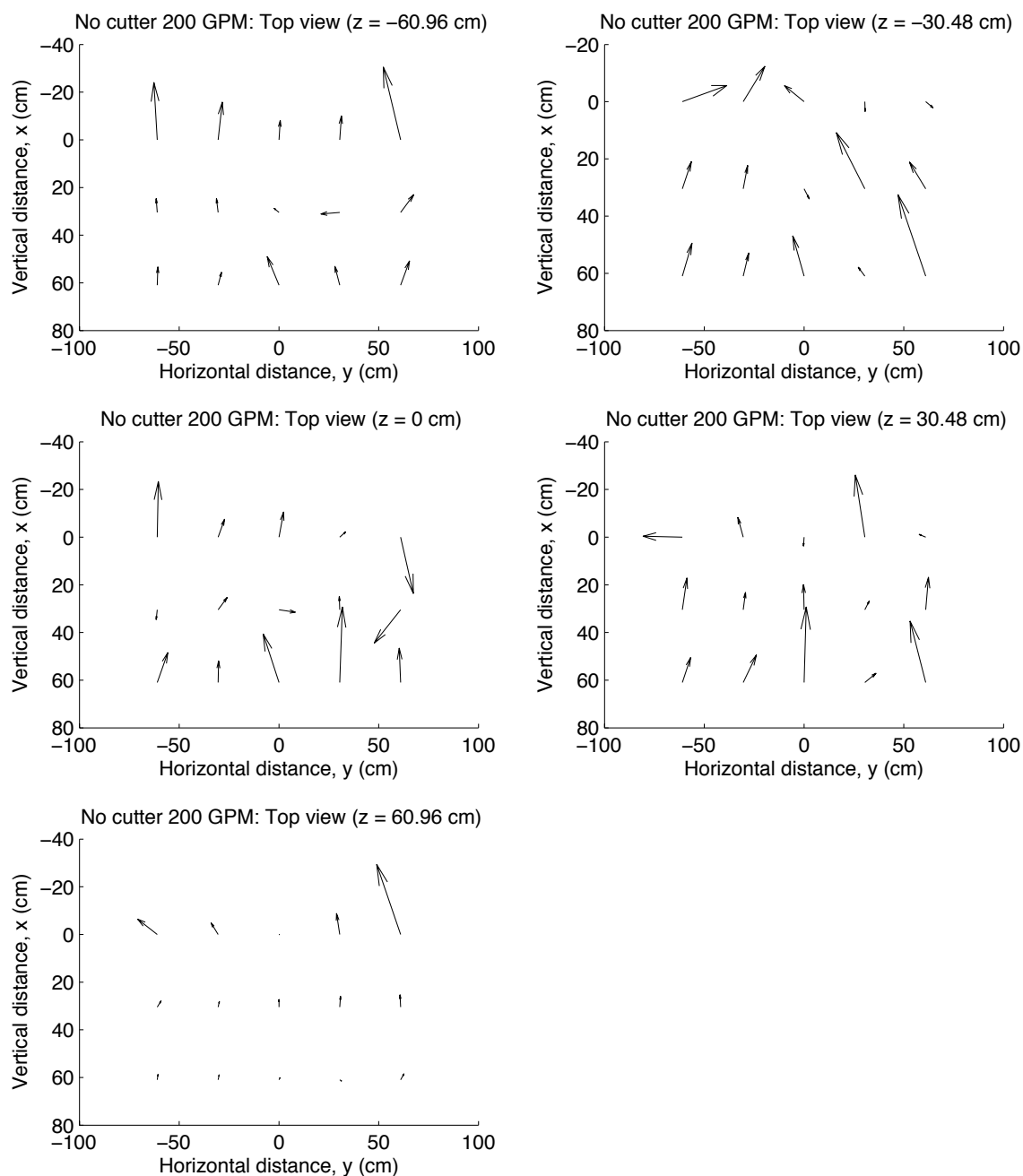


Figure 76: Quiver plots in the  $y$ - $x$  plane for the scenario with no cutterhead attached and 200 GPM.

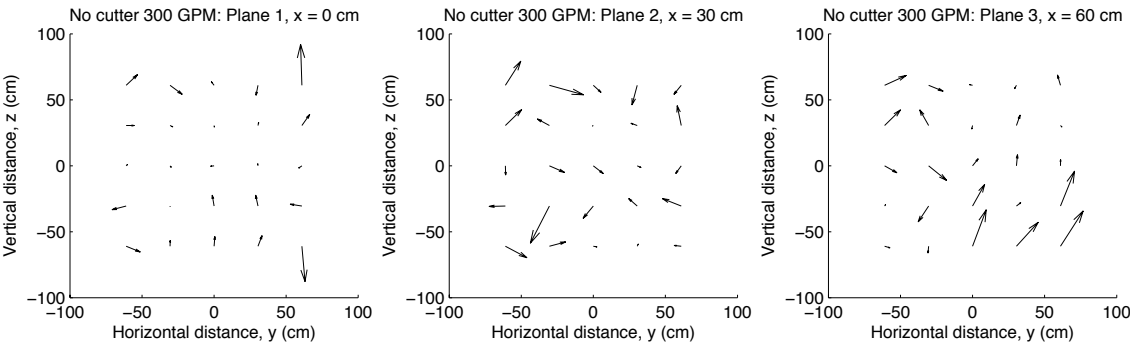


Figure 77: Quiver plots in the y-z plane for the scenario with no cutterhead attached and 300 GPM.

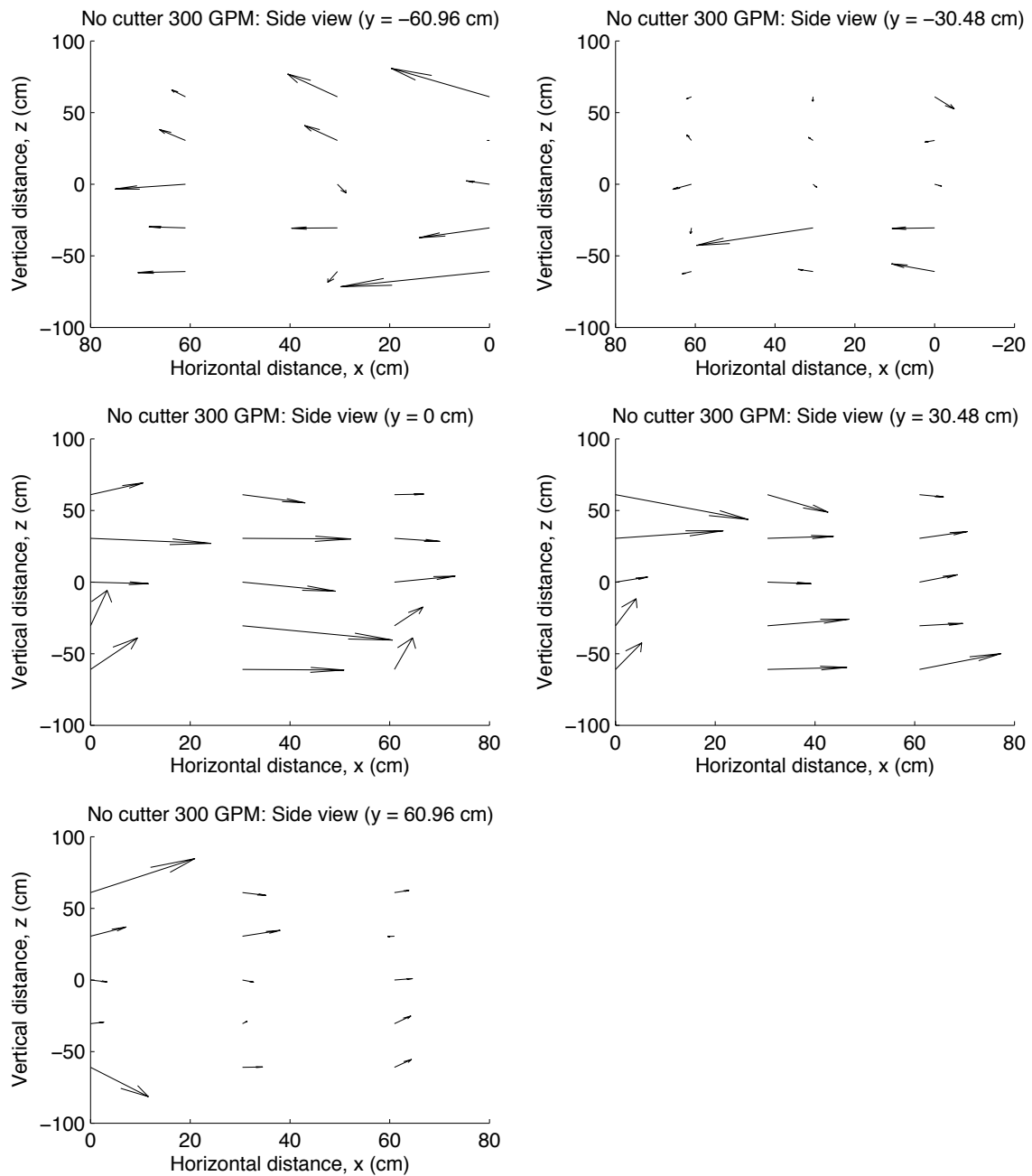


Figure 78: Quiver plots in the x-z plane for the scenario with no cutterhead attached and 300 GPM.

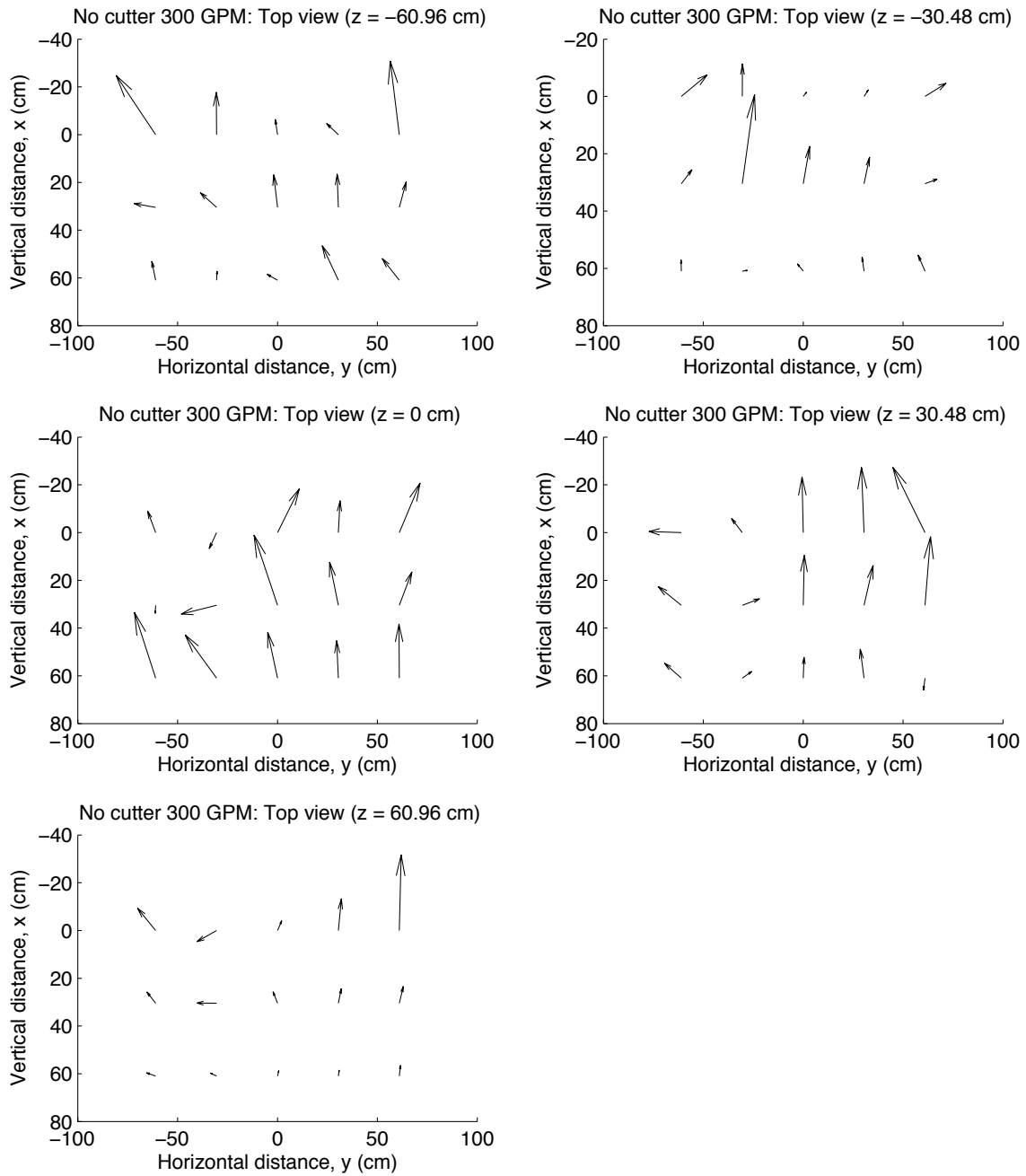


Figure 79: Quiver plots in the  $y$ - $x$  plane for the scenario with no cutterhead attached and 300 GPM.

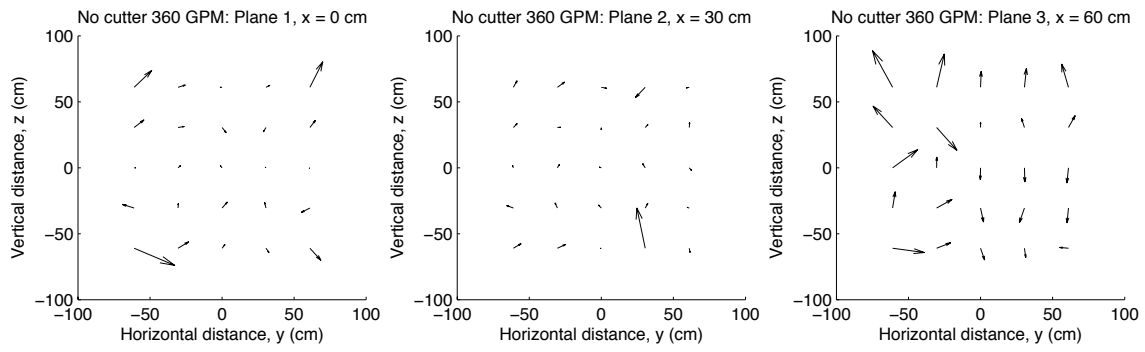


Figure 80: Quiver plots in the y-z plane for the scenario with no cutterhead attached and 360 GPM.



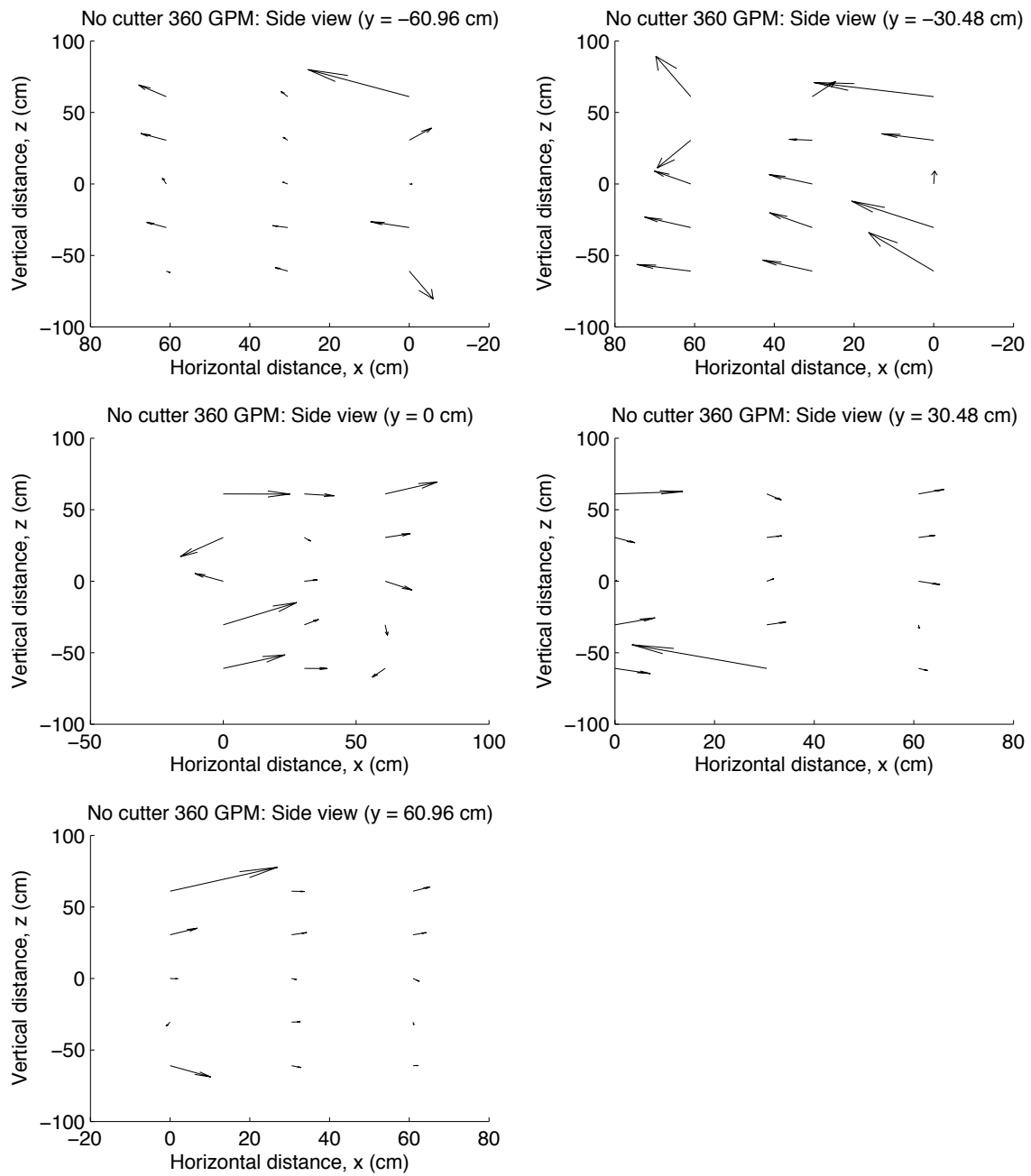


Figure 81: Quiver plots in the x-z plane for the scenario with no cutterhead attached and 360 GPM.

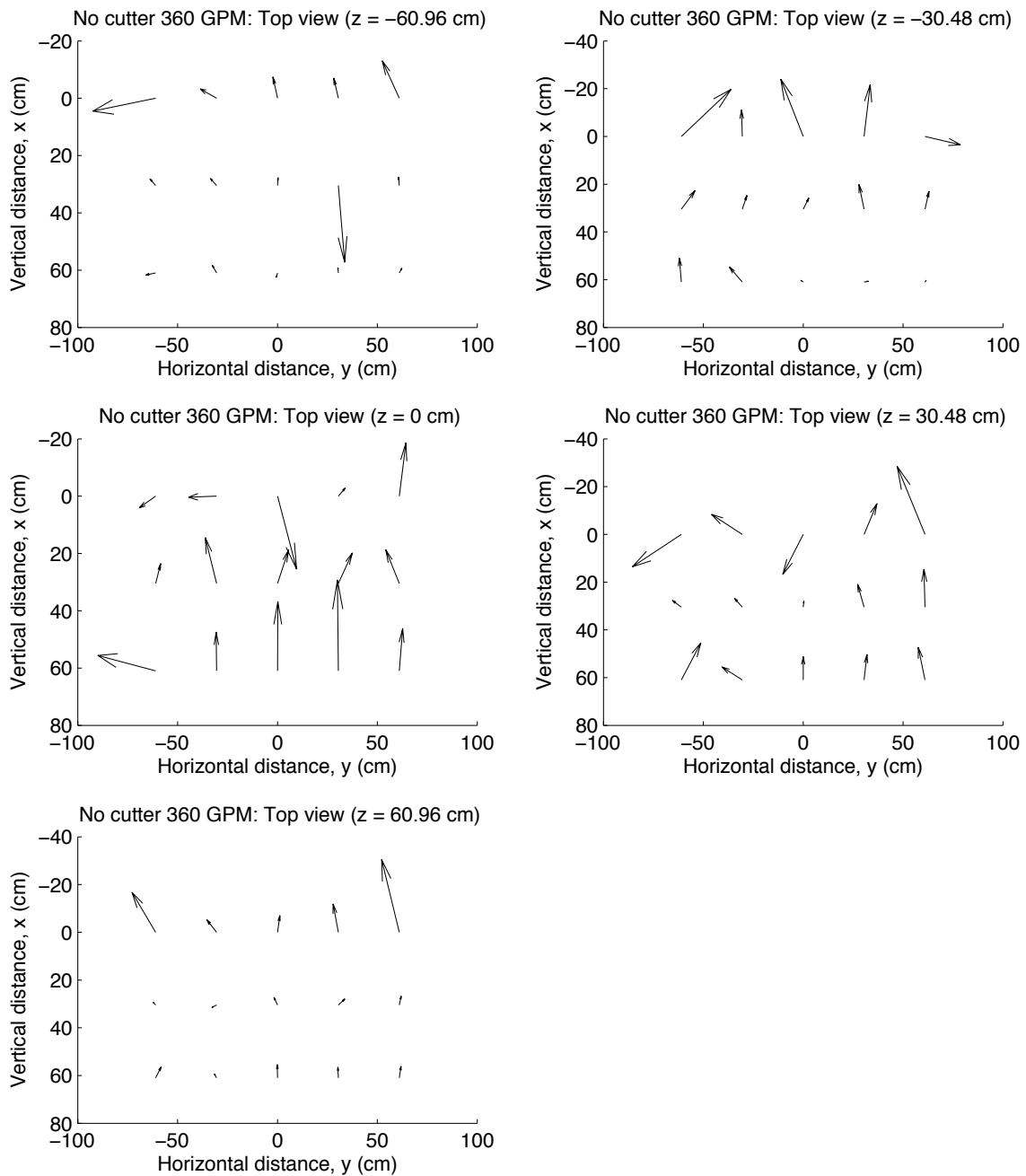


Figure 82: Quiver plots in the  $y$ - $x$  plane for the scenario with no cutterhead attached and 360 GPM.

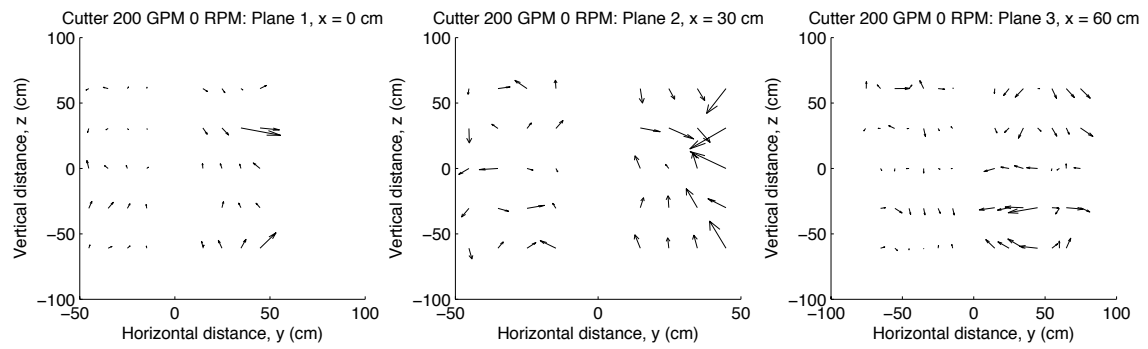


Figure 83: Quiver plots in the y-z plane for the scenario with cutterhead attached, 200 GPM, and 0 RPM.

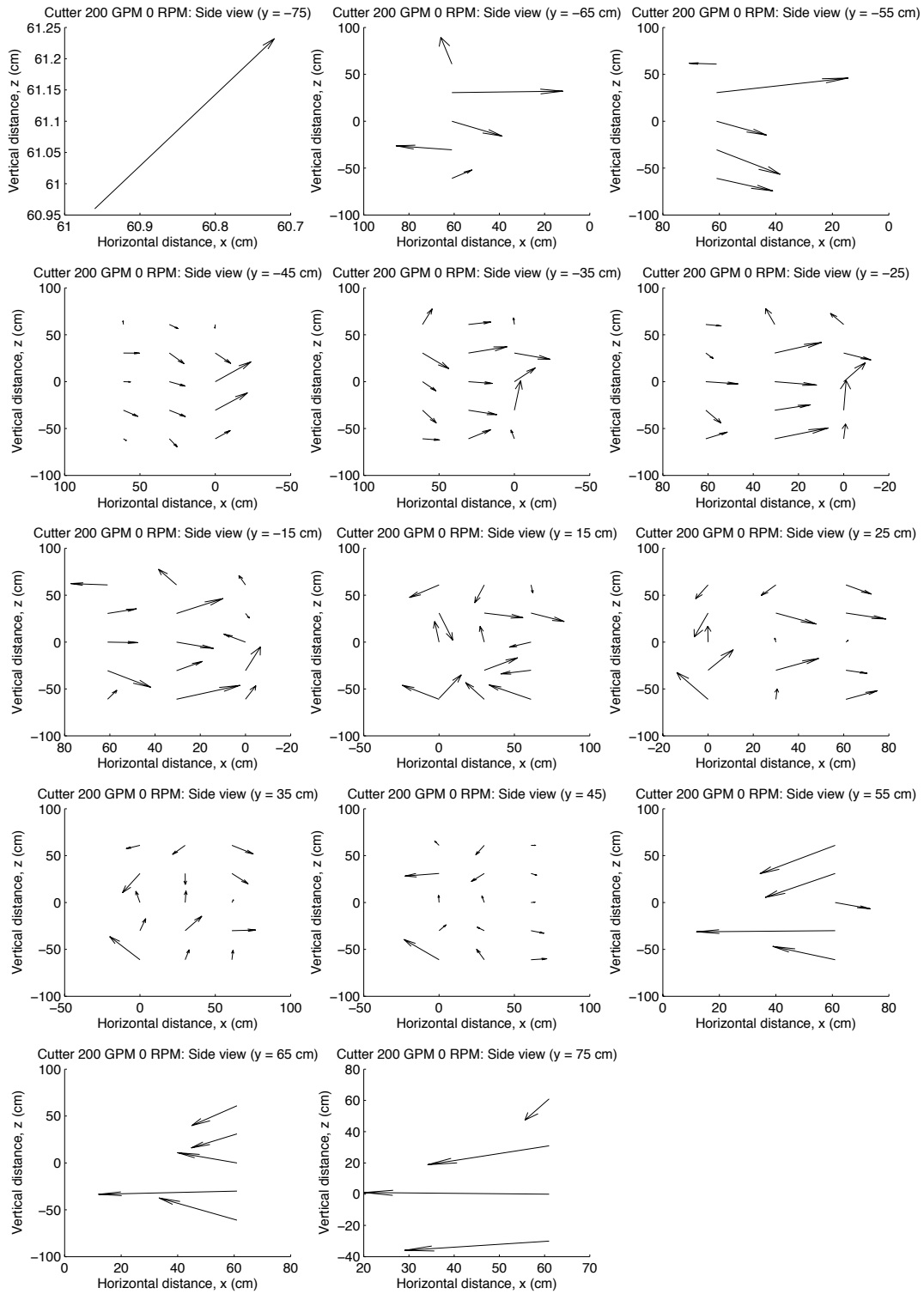


Figure 84: Quiver plots in the x-z plane for the scenario with cutterhead attached, 200 GPM, and 0 RPM.

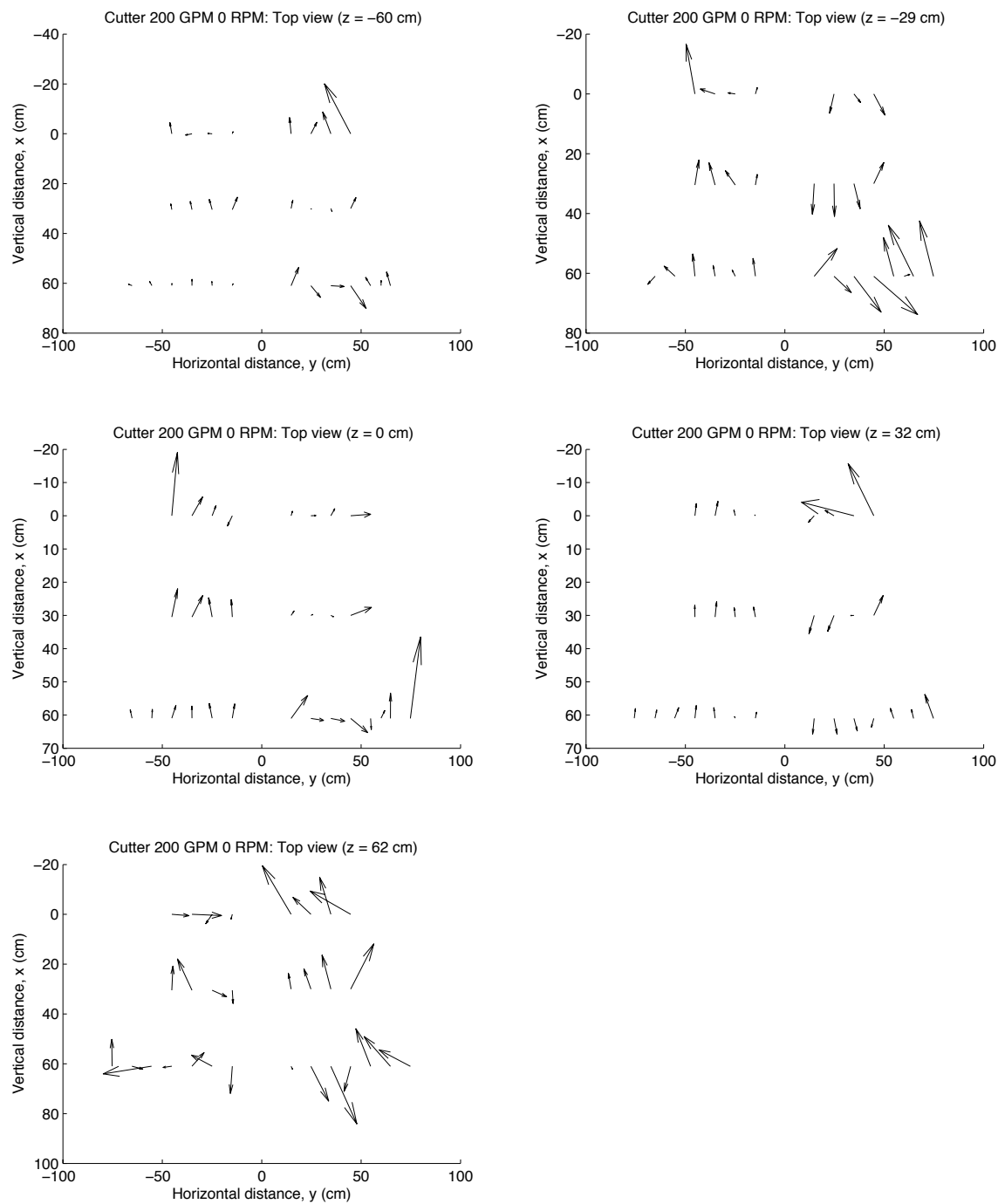


Figure 85: Quiver plots in the  $y$ - $x$  plane for the scenario with cutterhead attached, 200 GPM, and 0 RPM.

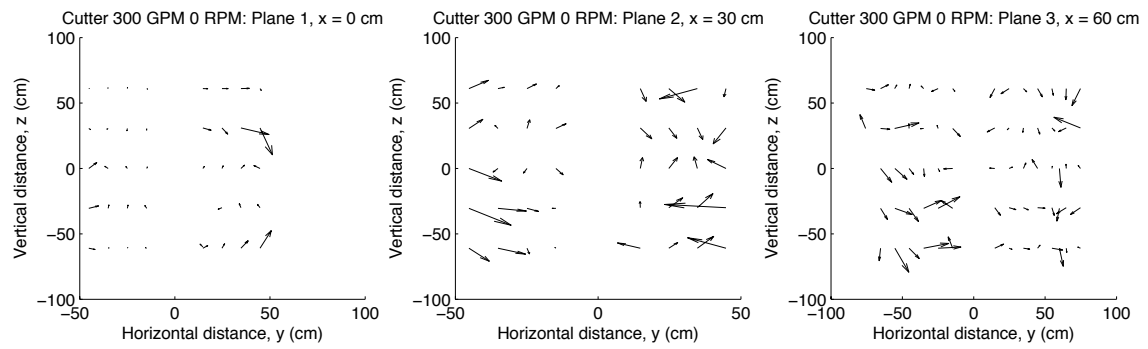


Figure 86: Quiver plots in the y-z plane for the scenario with cutterhead attached, 300 GPM, and 0 RPM.

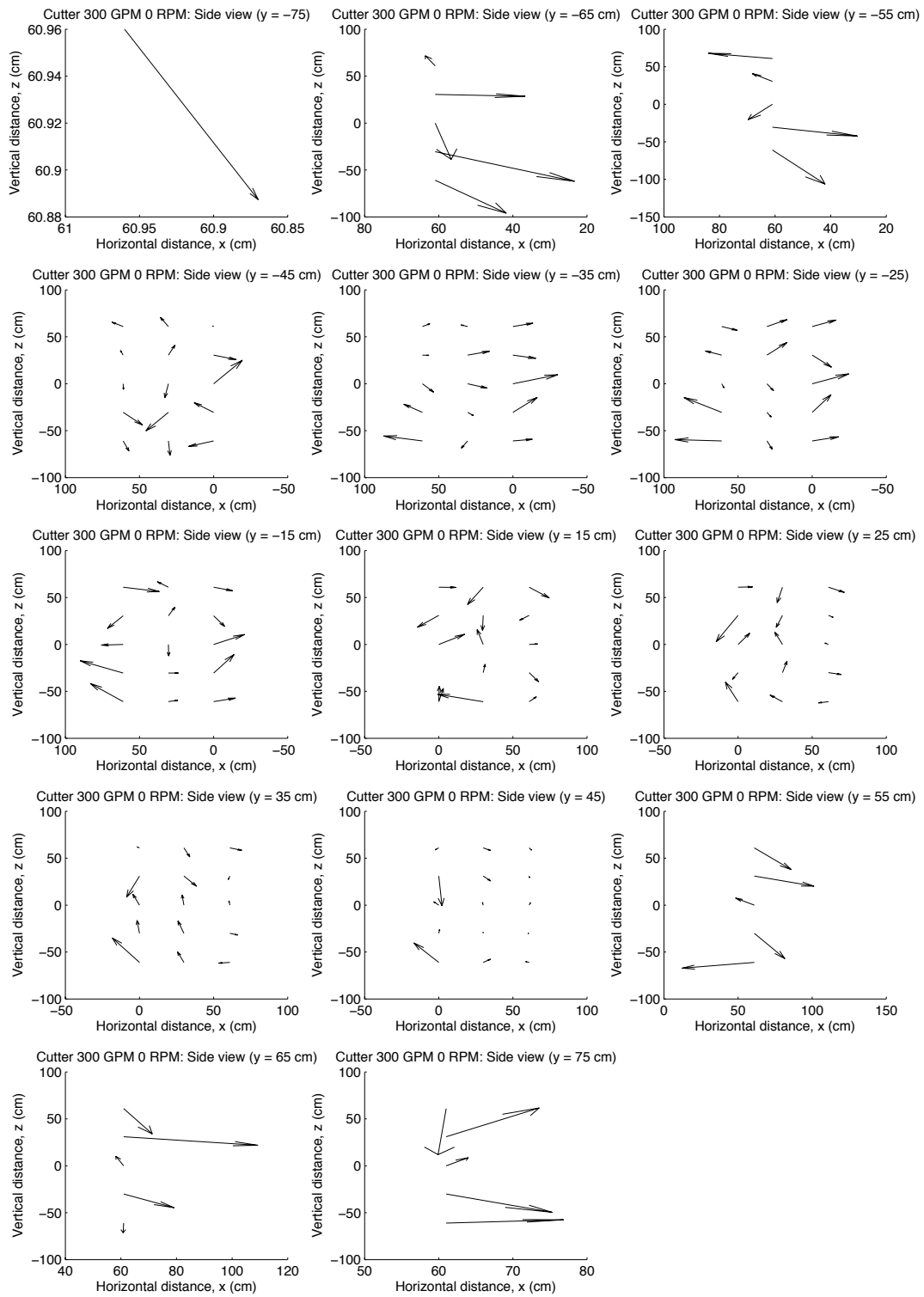


Figure 87: Quiver plots in the  $x$ - $z$  plane for the scenario with cutterhead attached, 300 GPM, and 0 RPM.

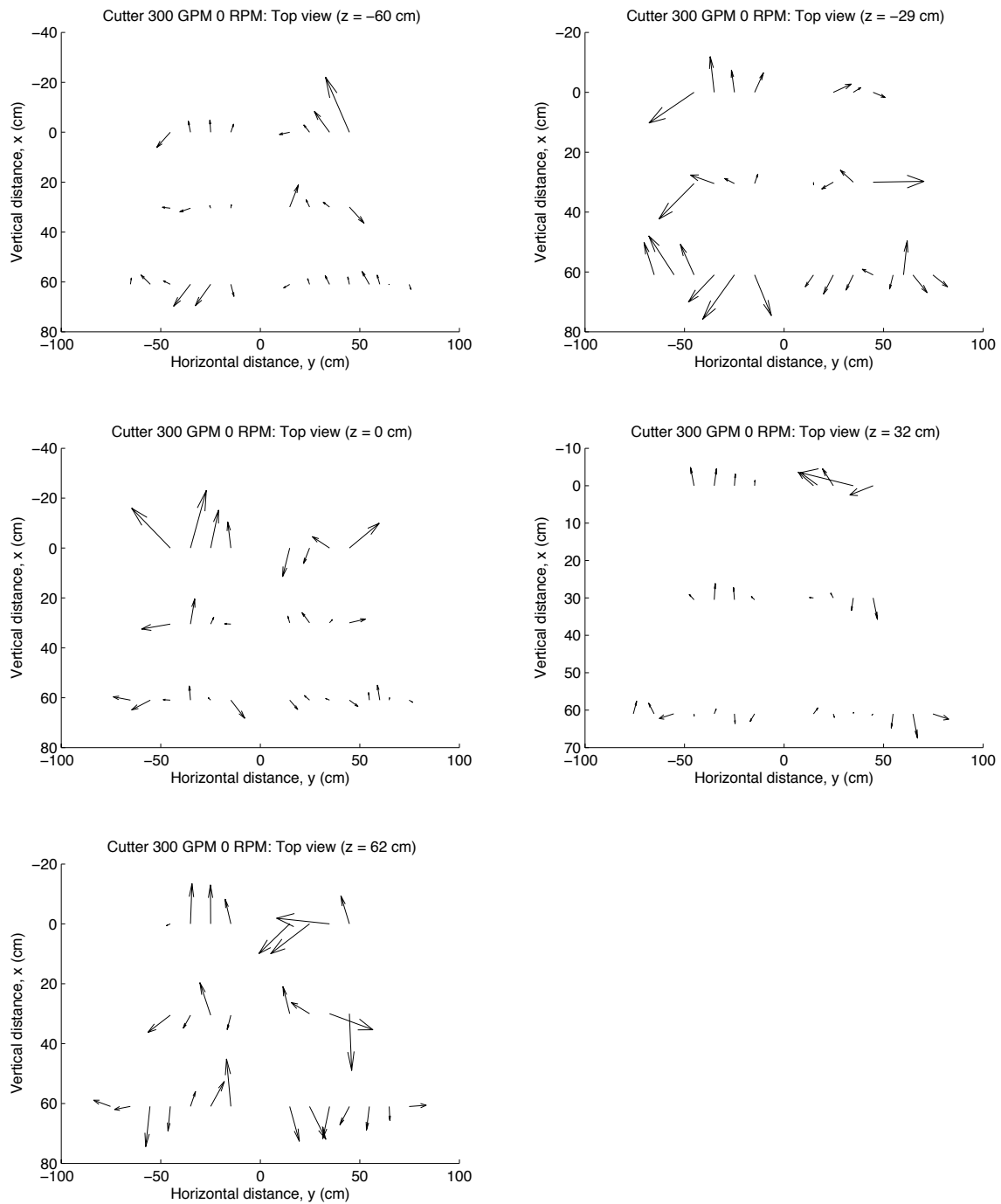


Figure 88: Quiver plots in the  $y$ - $x$  plane for the scenario with cutterhead attached, 300 GPM, and 0 RPM.



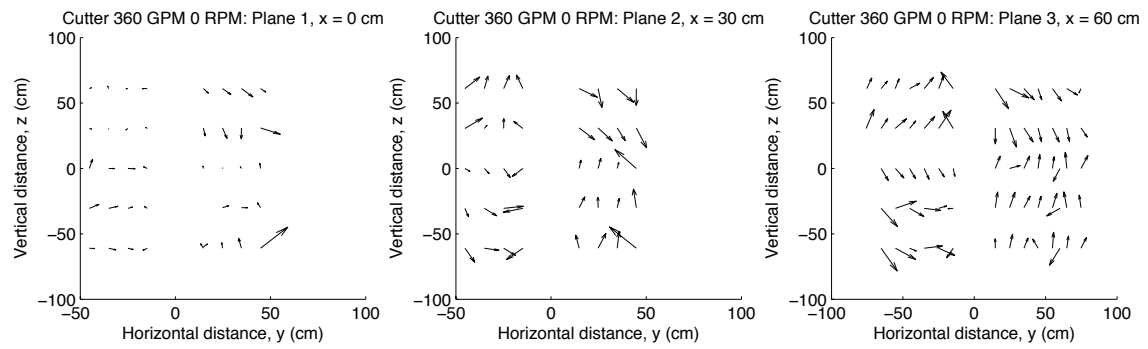


Figure 89: Quiver plots in the y-z plane for the scenario with cutterhead attached, 360 GPM, and 0 RPM.

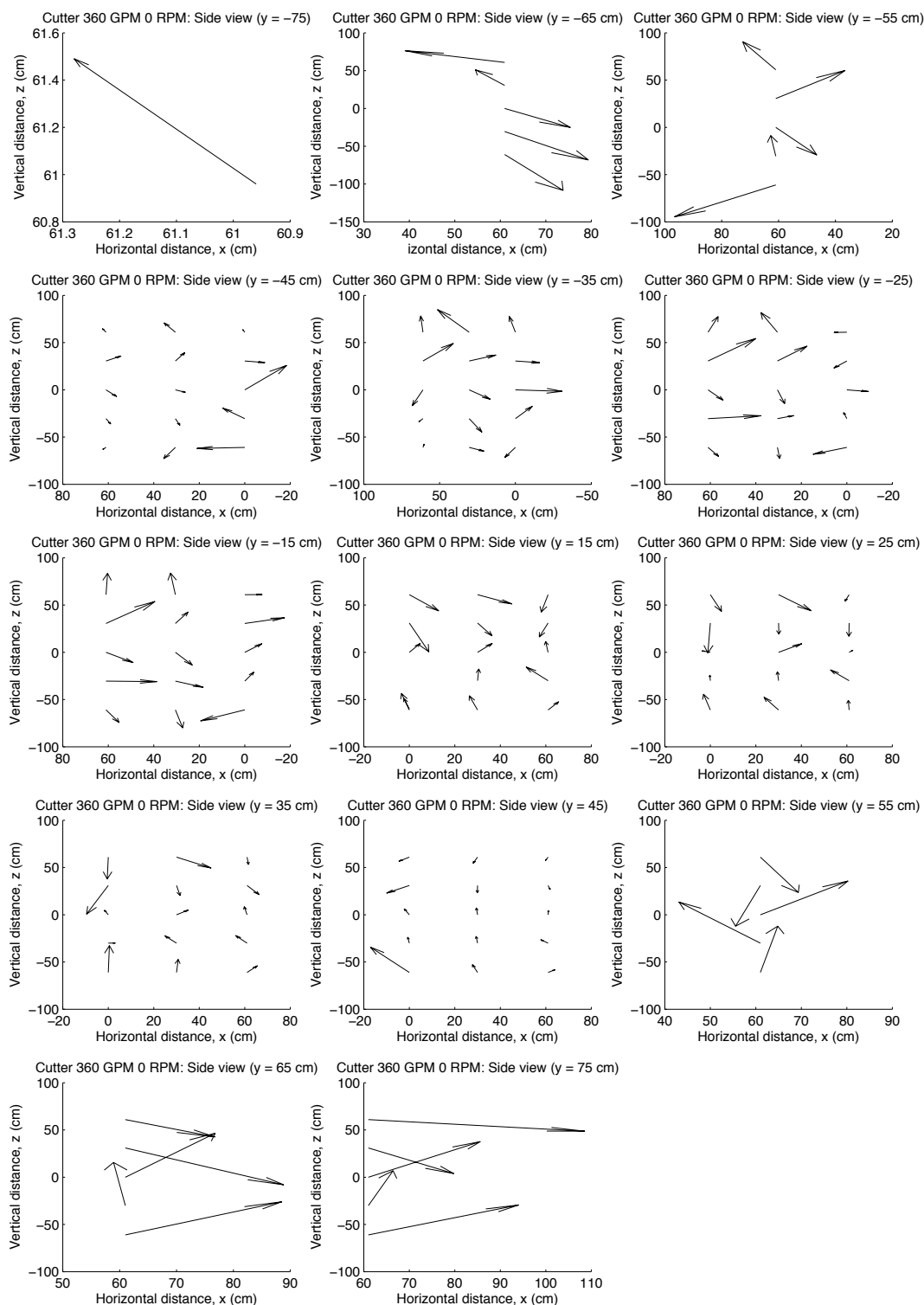


Figure 90: Quiver plots in the x-z plane for the scenario with cutterhead attached, 360 GPM, and 0 RPM.

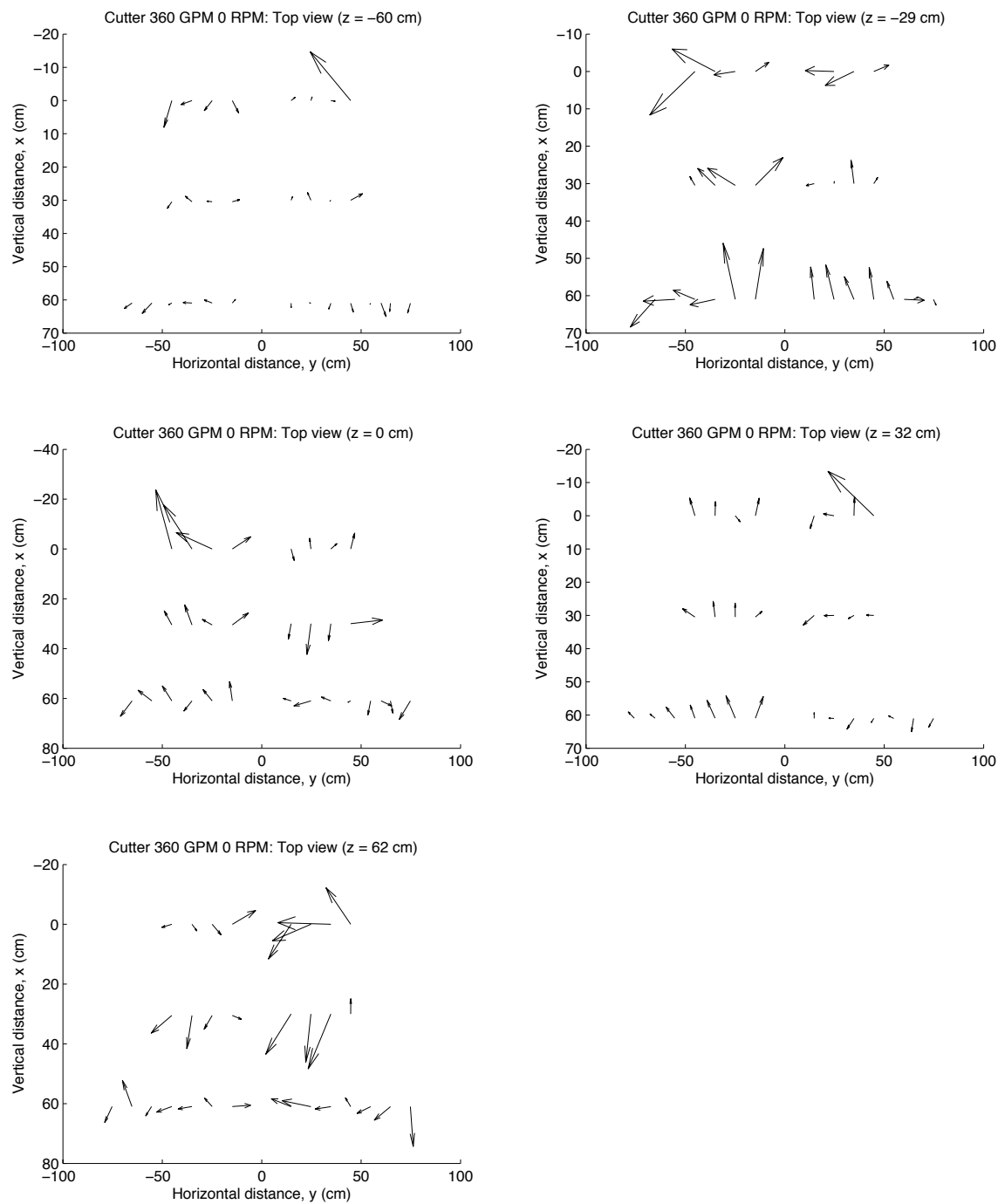


Figure 91: Quiver plots in the y-x plane for the scenario with cutterhead attached, 360 GPM, and 0 RPM.

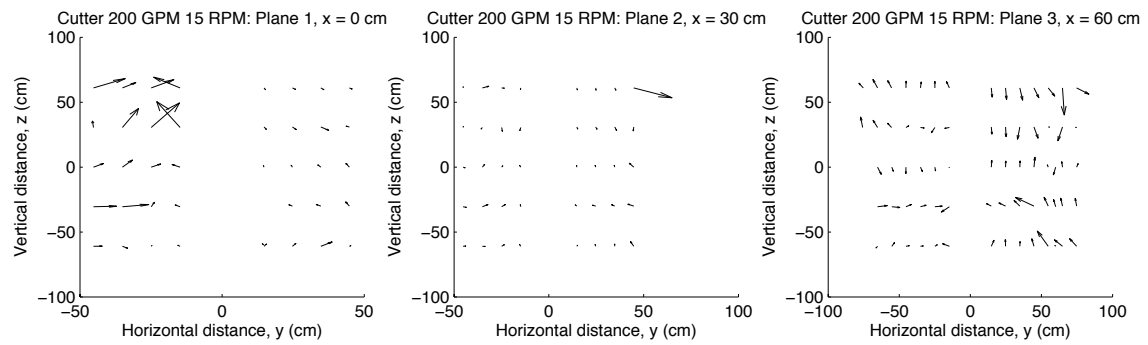


Figure 92: Quiver plots in the  $y$ - $z$  plane for the scenario with cutterhead attached, 200 GPM, and 15 RPM.

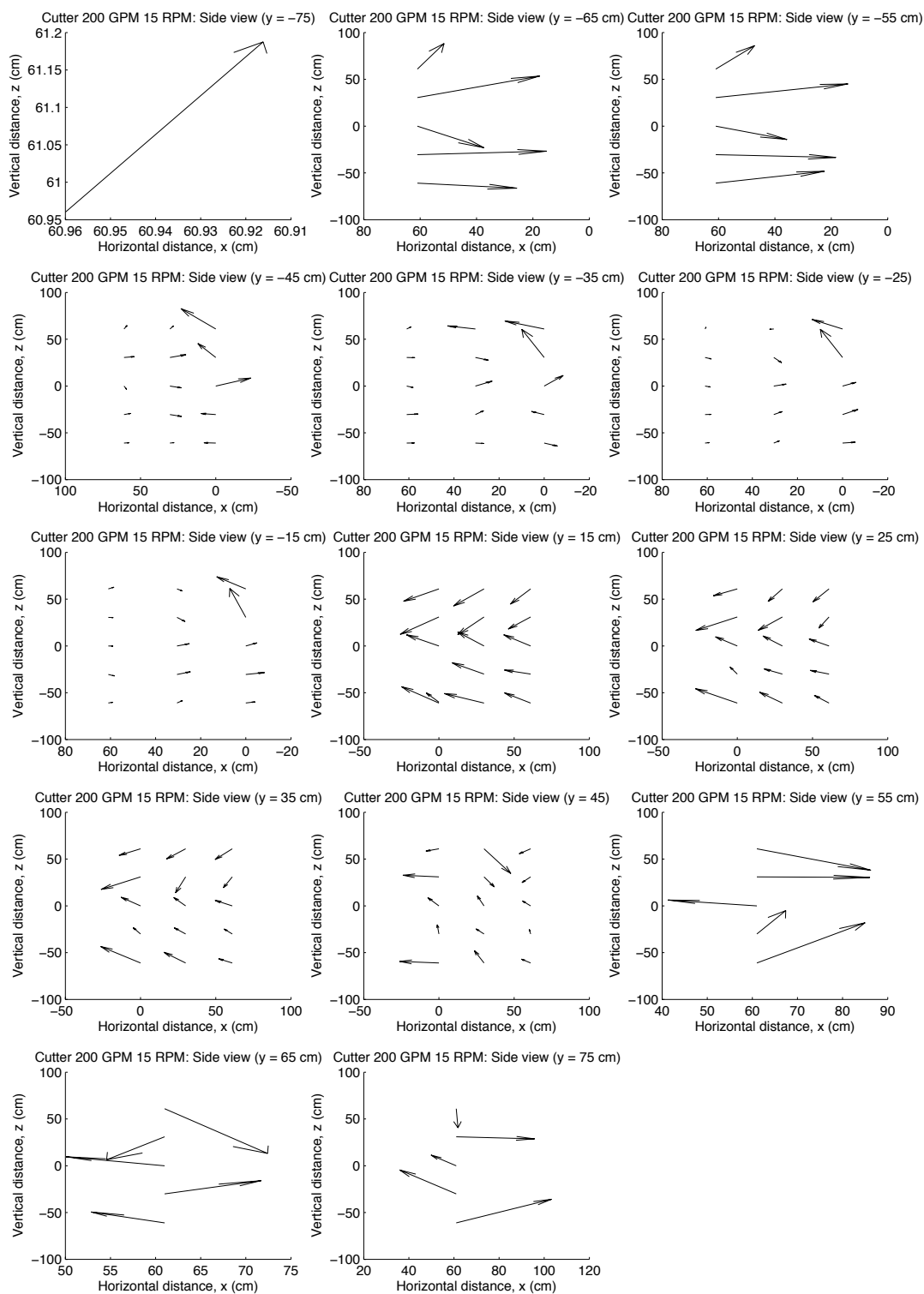


Figure 93: Quiver plots in the  $x$ - $z$  plane for the scenario with cutterhead attached, 200 GPM, and 15 RPM.

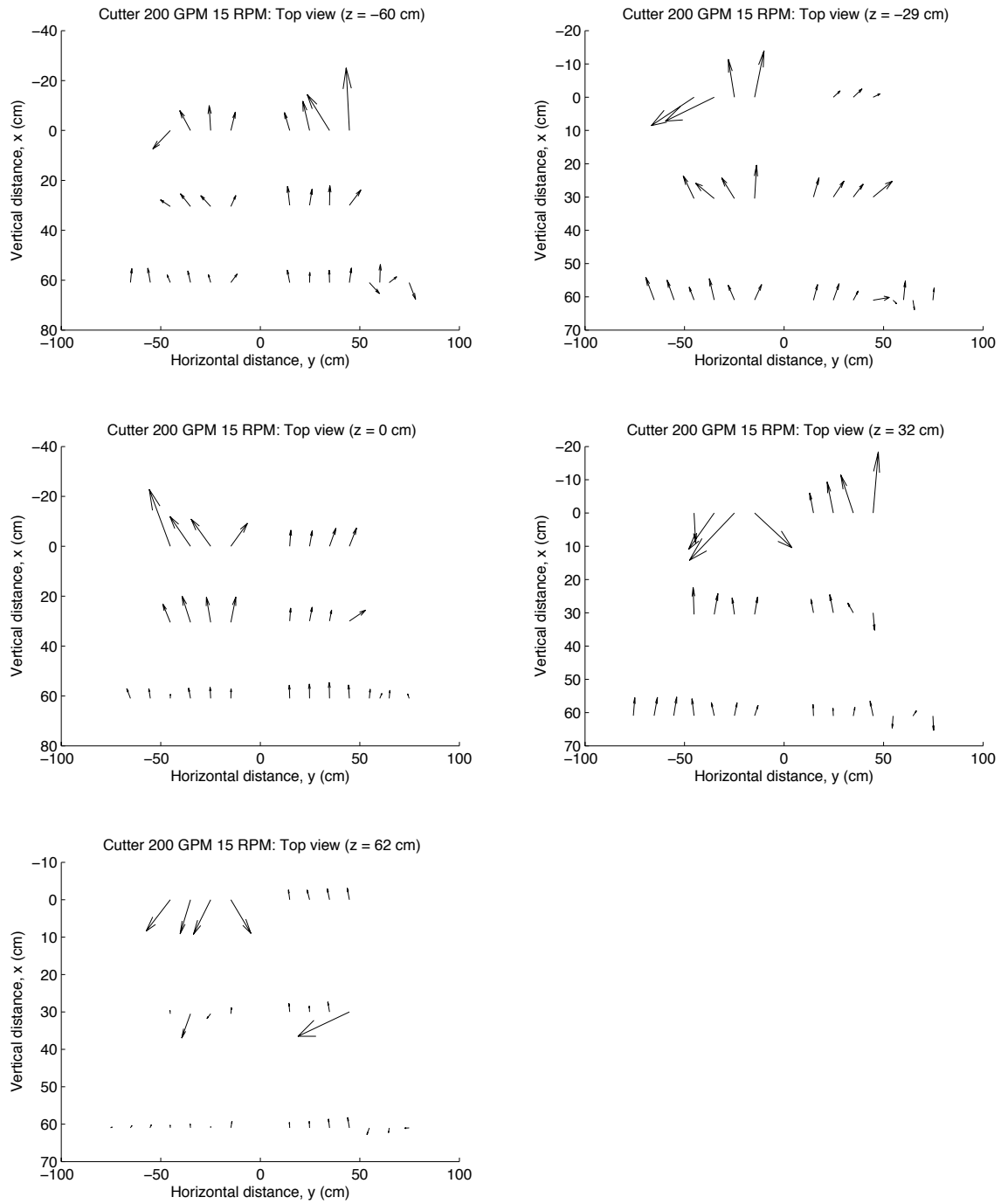


Figure 94: Quiver plots in the  $y$ - $x$  plane for the scenario with cutterhead attached, 200 GPM, and 15 RPM.

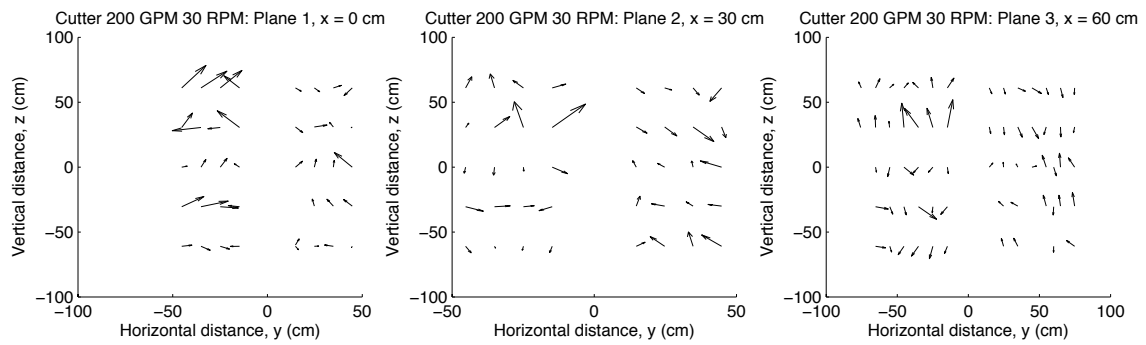


Figure 95: Quiver plots in the y-z plane for the scenario with cutterhead attached, 200 GPM, and 30 RPM.

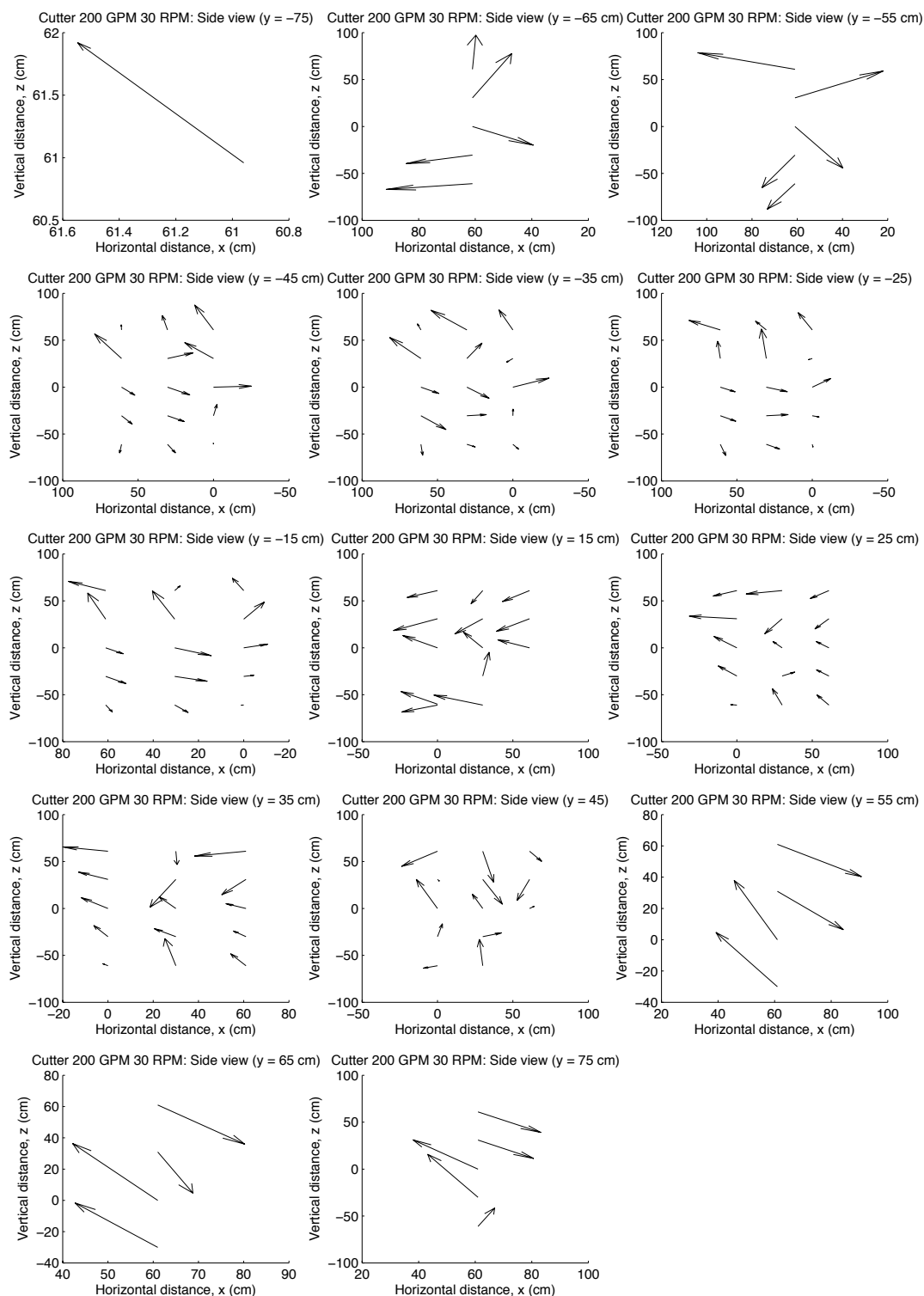


Figure 96: Quiver plots in the  $x$ - $z$  plane for the scenario with cutterhead attached, 200 GPM, and 30 RPM.



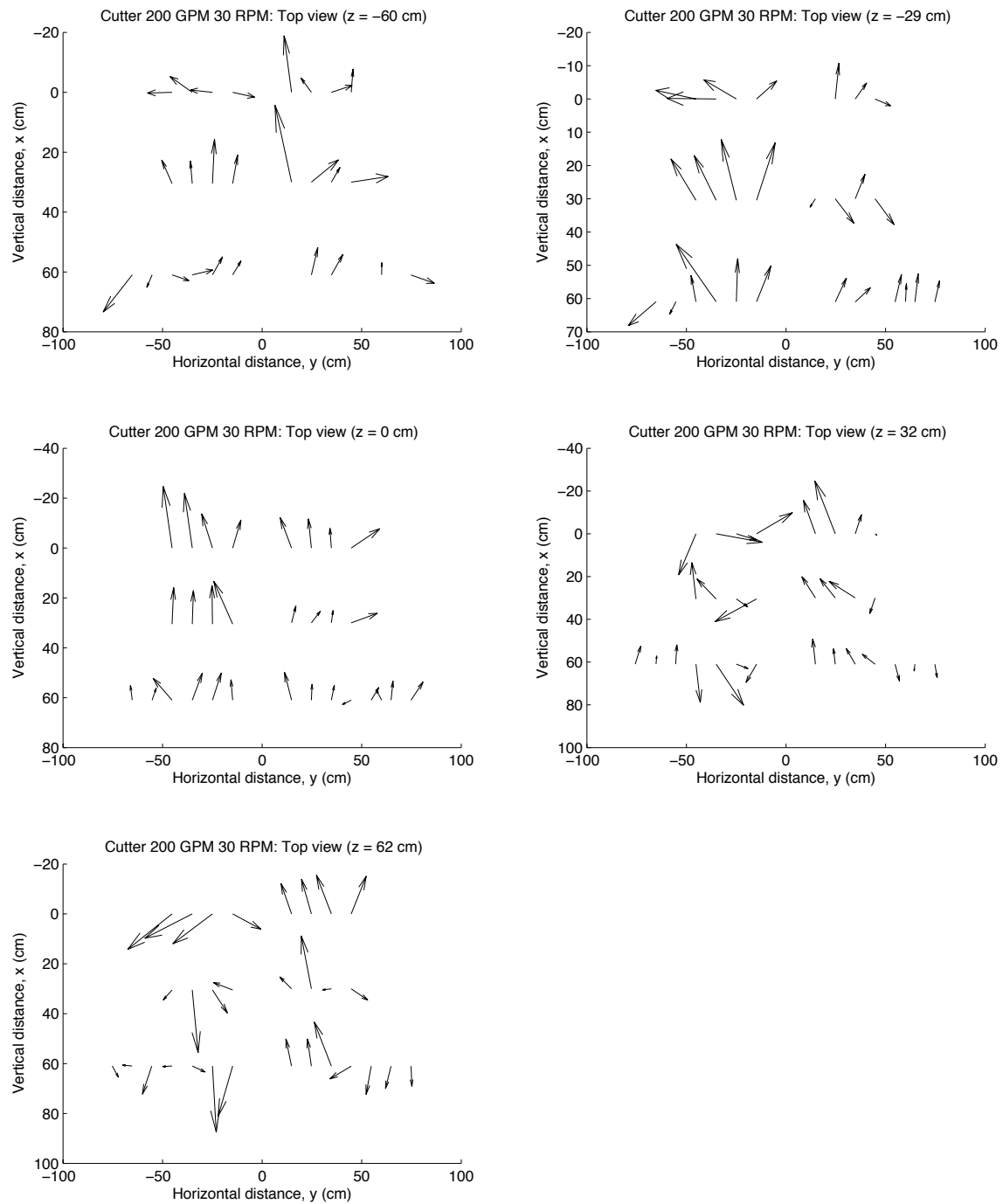


Figure 97: Quiver plots in the  $y$ - $x$  plane for the scenario with cutterhead attached, 200 GPM, and 30 RPM.

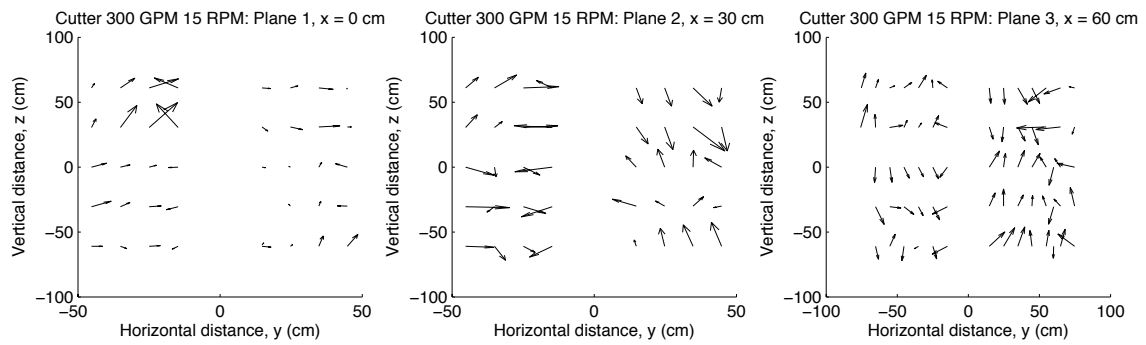


Figure 98: Quiver plots in the y-z plane for the scenario with cutterhead attached, 300 GPM, and 15 RPM.

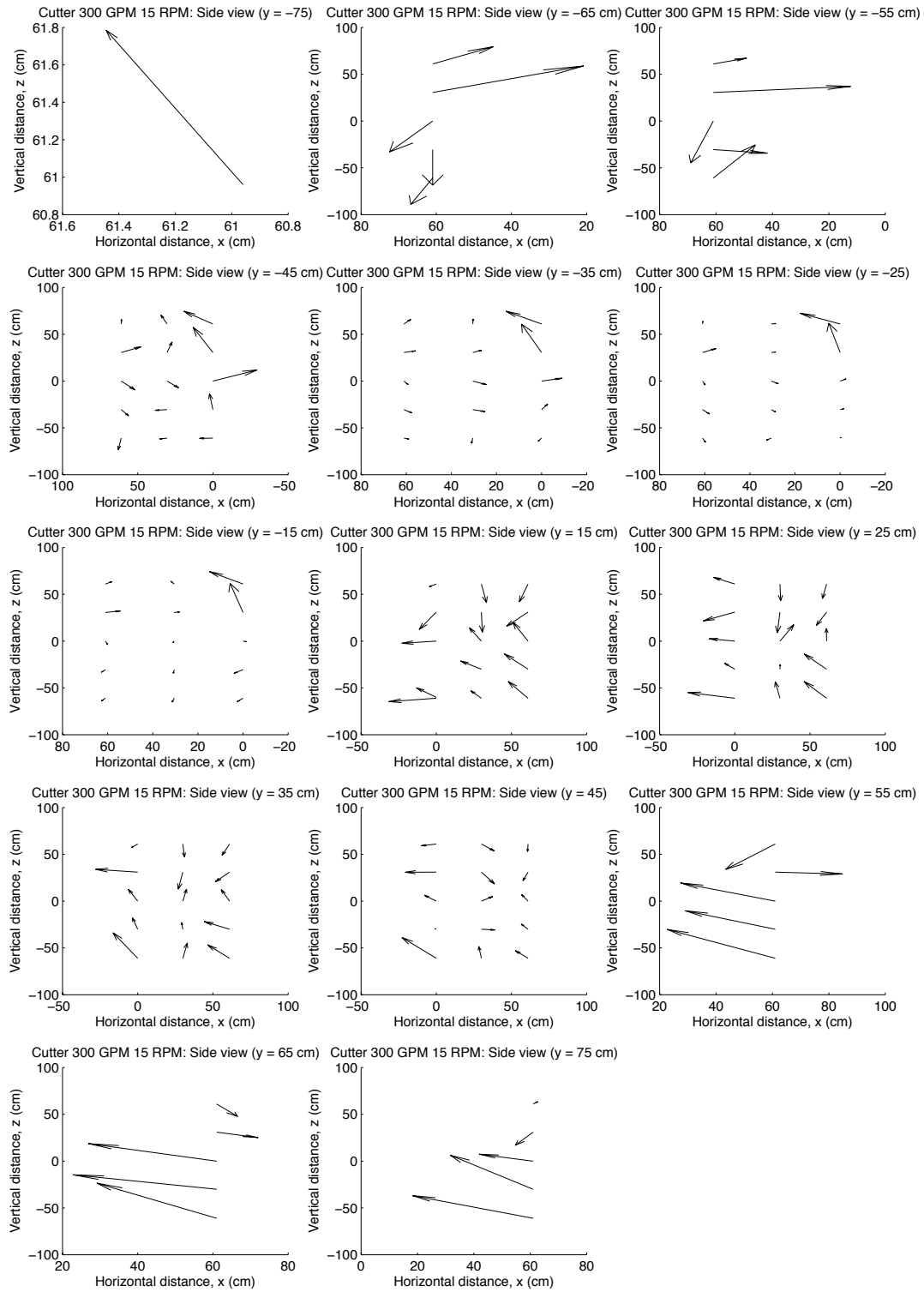


Figure 99: Quiver plots in the  $x$ - $z$  plane for the scenario with cutterhead attached, 300 GPM, and 15 RPM.

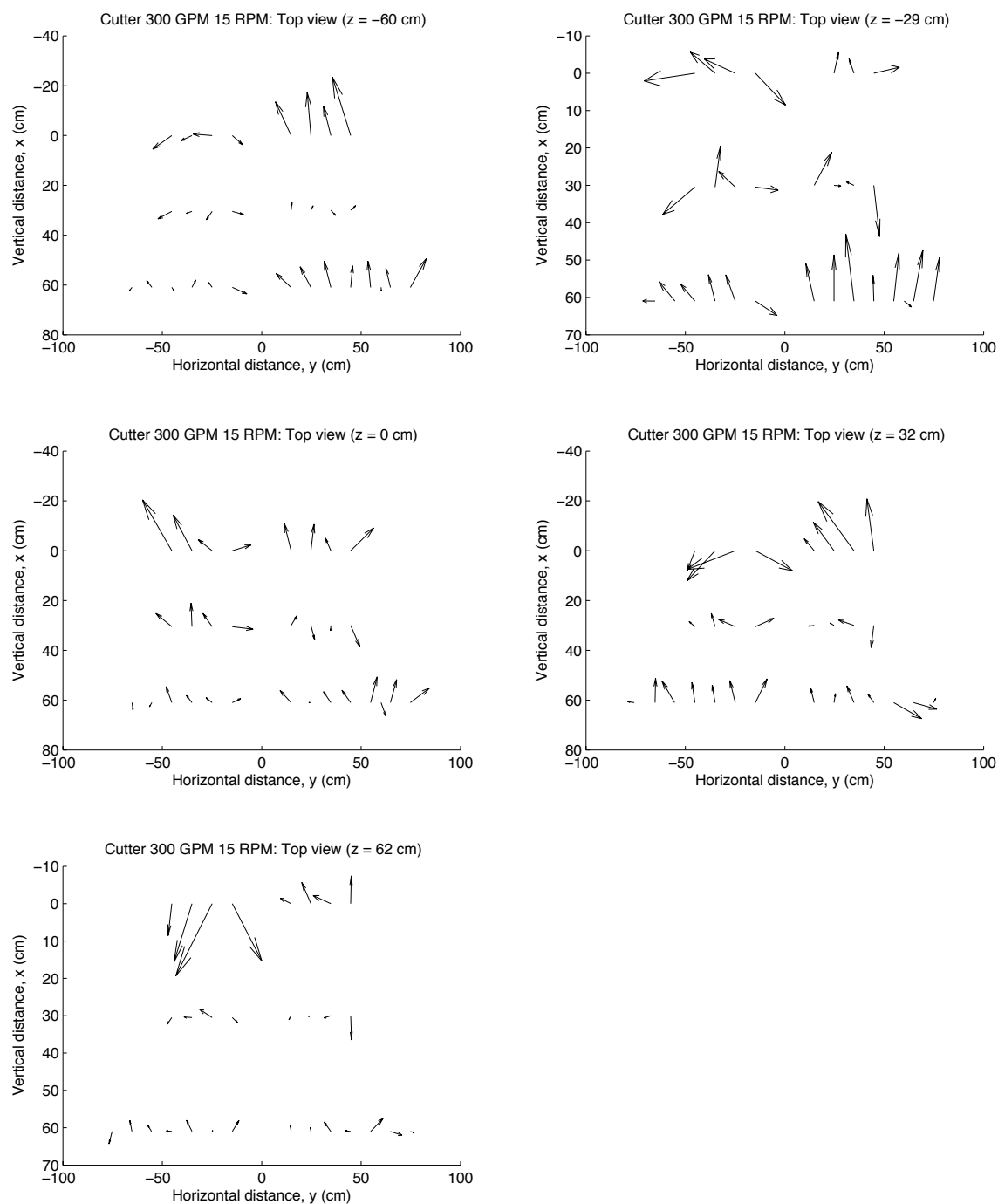


Figure 100: Quiver plots in the  $y$ - $x$  plane for the scenario with cutterhead attached, 300 GPM, and 15 RPM.

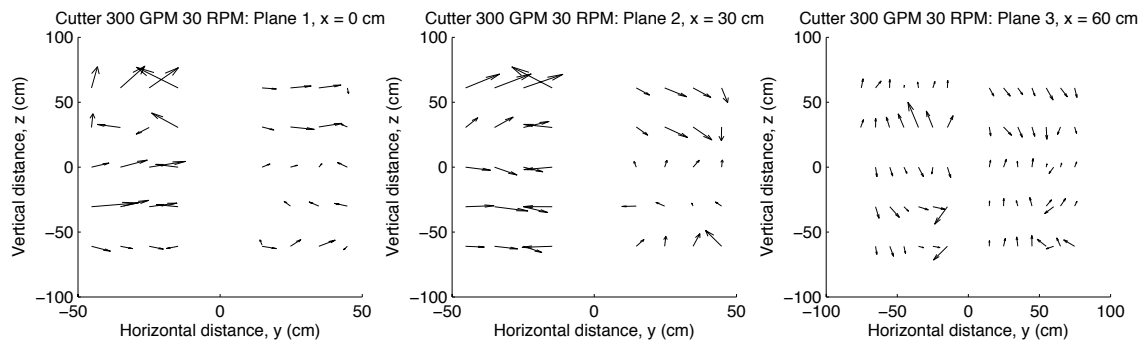


Figure 101: Quiver plots in the  $y$ - $z$  plane for the scenario with cutterhead attached, 300 GPM, and 30 RPM.

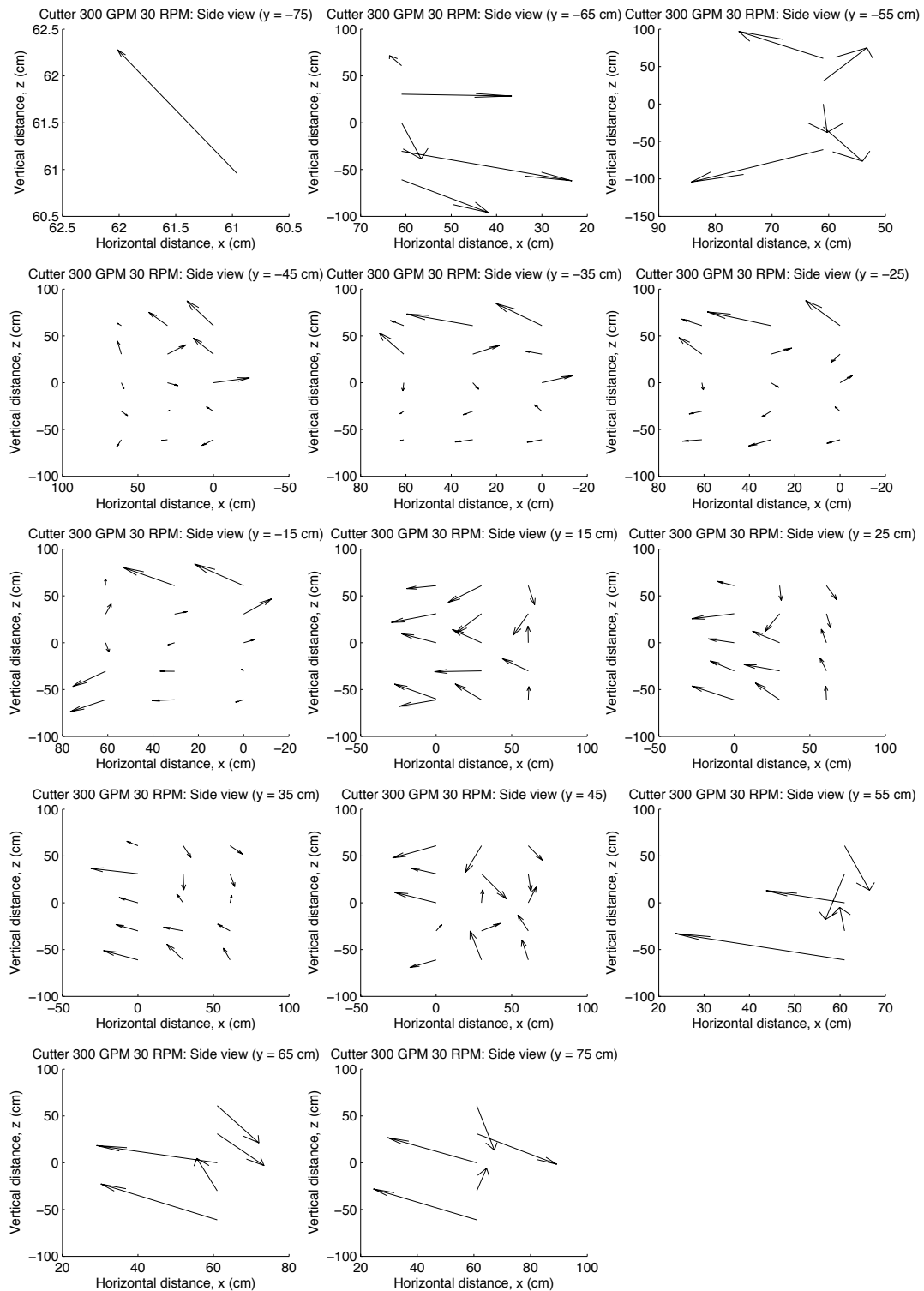


Figure 102: Quiver plots in the x-z plane for the scenario with cutterhead attached, 300 GPM, and 30 RPM.

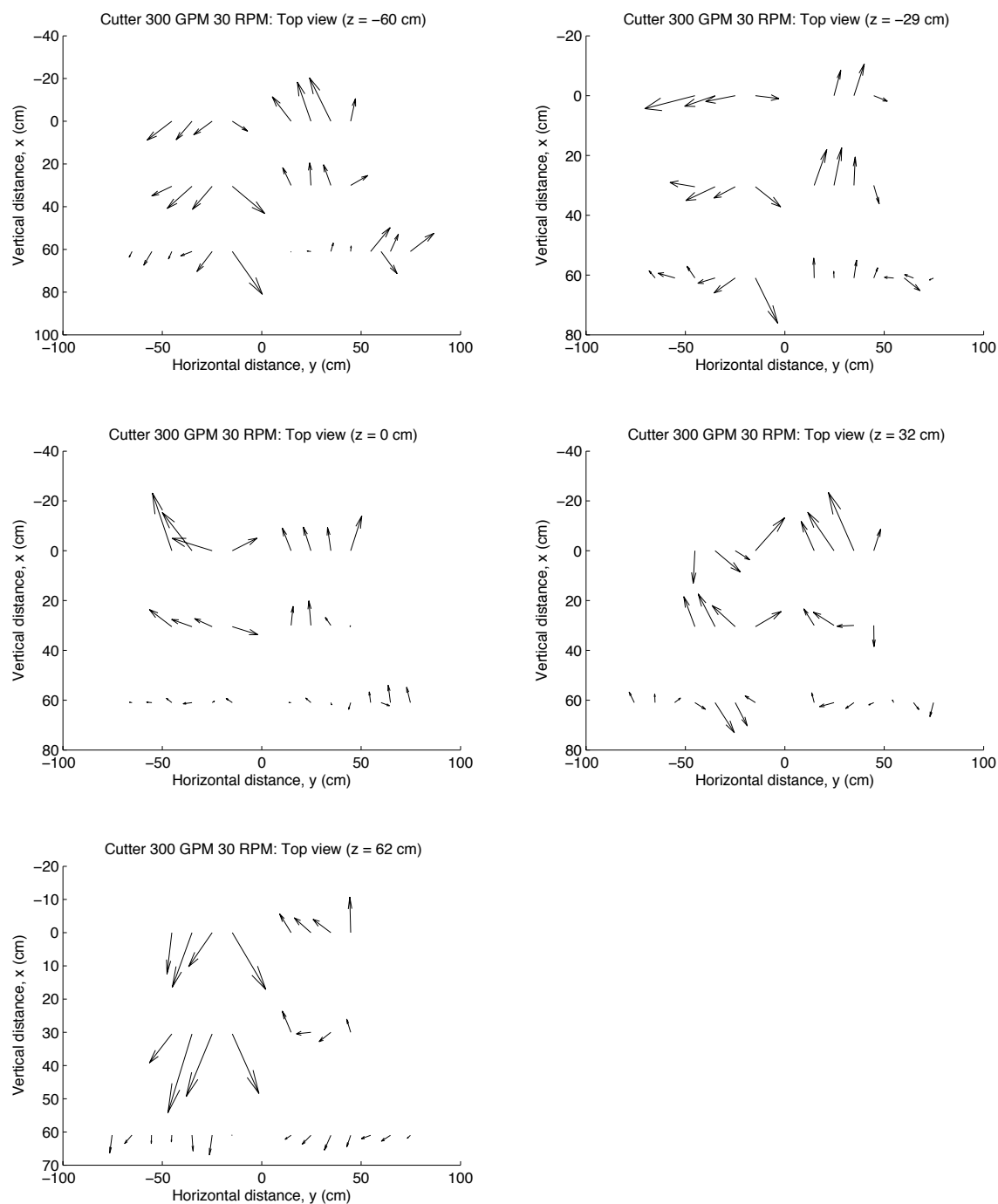


Figure 103: Quiver plots in the  $y$ - $x$  plane for the scenario with cutterhead attached, 300 GPM, and 30 RPM.

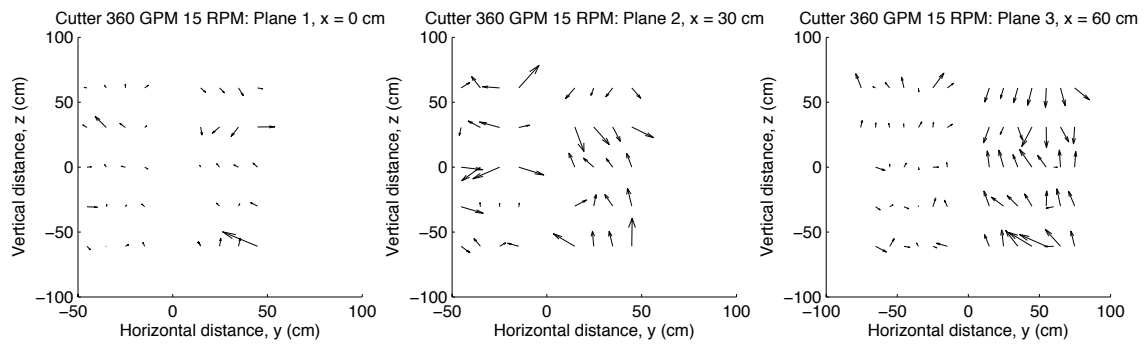


Figure 104: Quiver plots in the y-z plane for the scenario with cutterhead attached, 360 GPM, and 15 RPM.



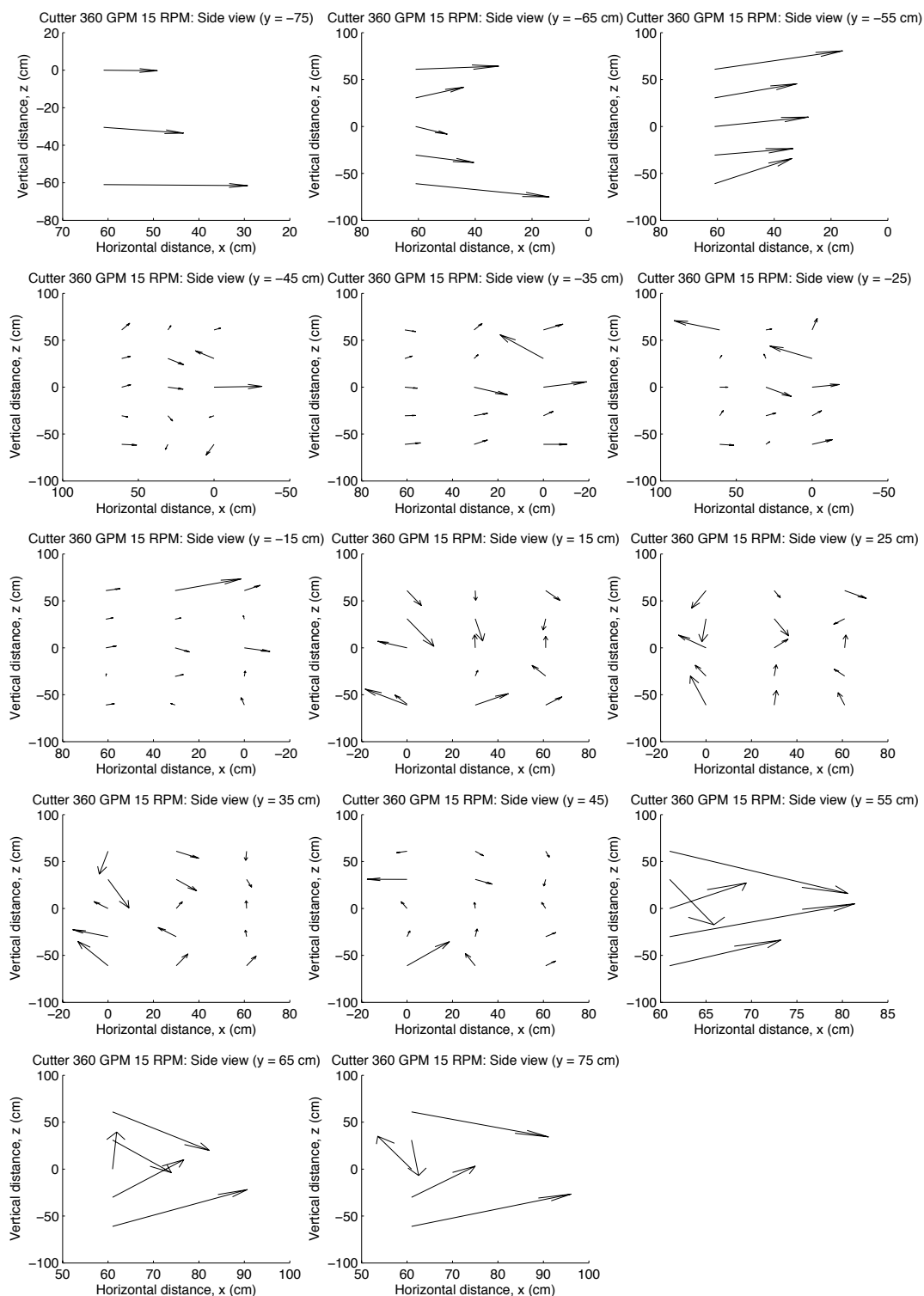


Figure 105: Quiver plots in the  $x$ - $z$  plane for the scenario with cutterhead attached, 360 GPM, and 15 RPM.

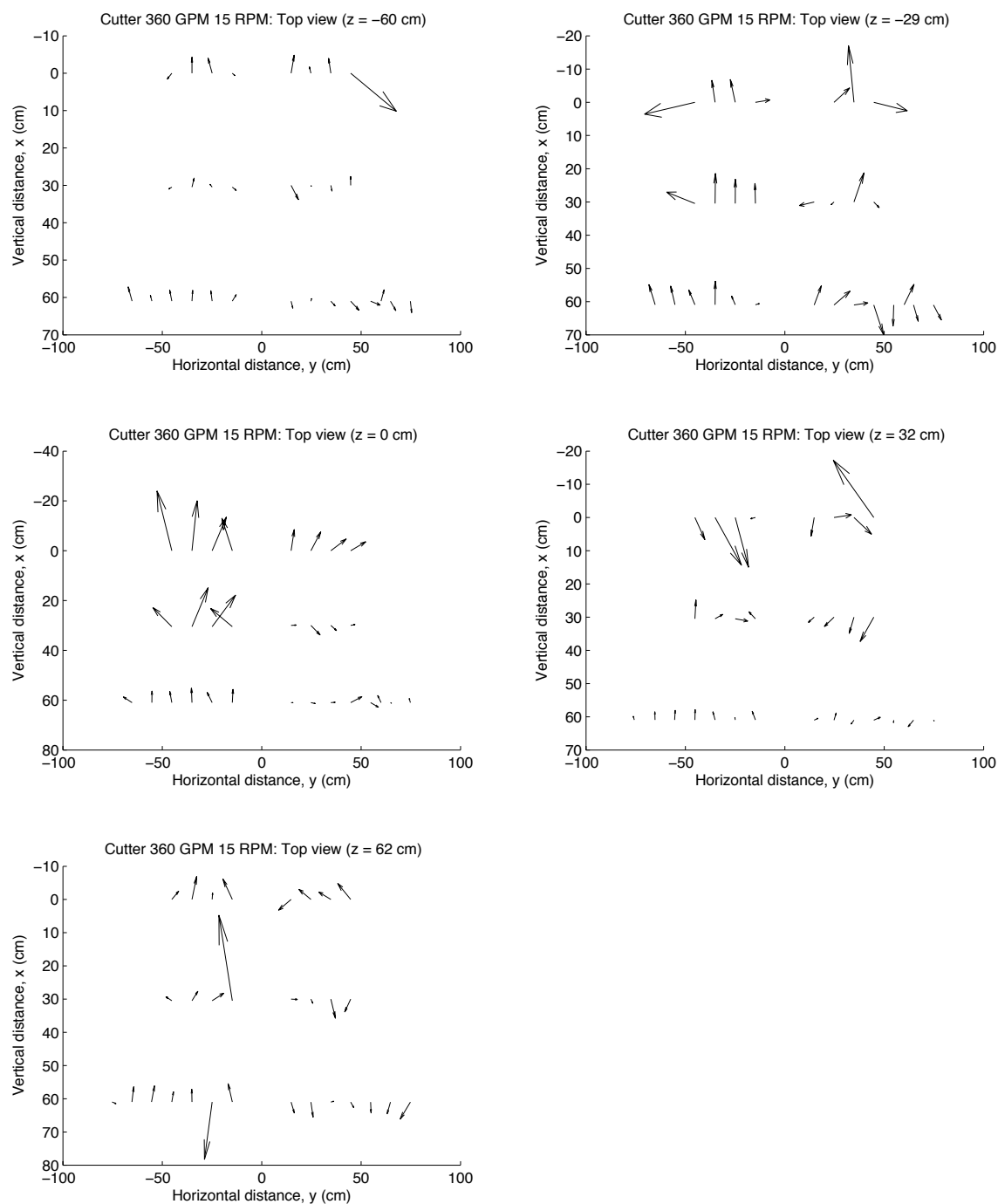


Figure 106: Quiver plots in the  $y$ - $x$  plane for the scenario with cutterhead attached, 360 GPM, and 15 RPM.

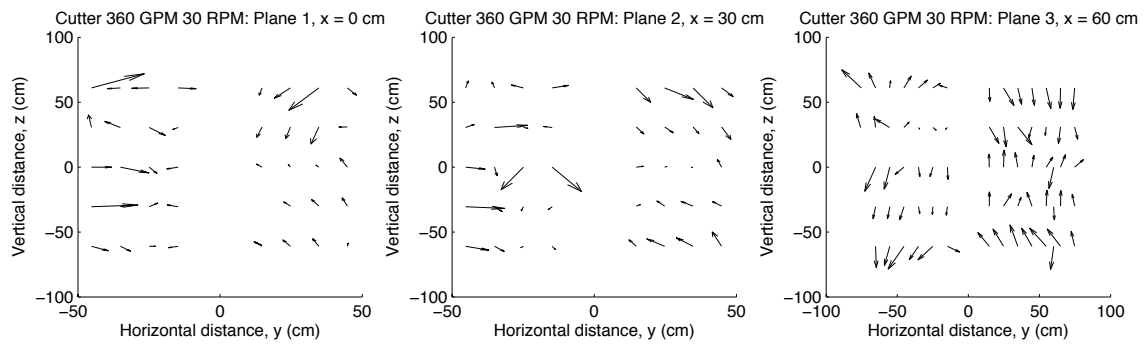


Figure 107: Quiver plots in the y-z plane for the scenario with cutterhead attached, 360 GPM, and 30 RPM.

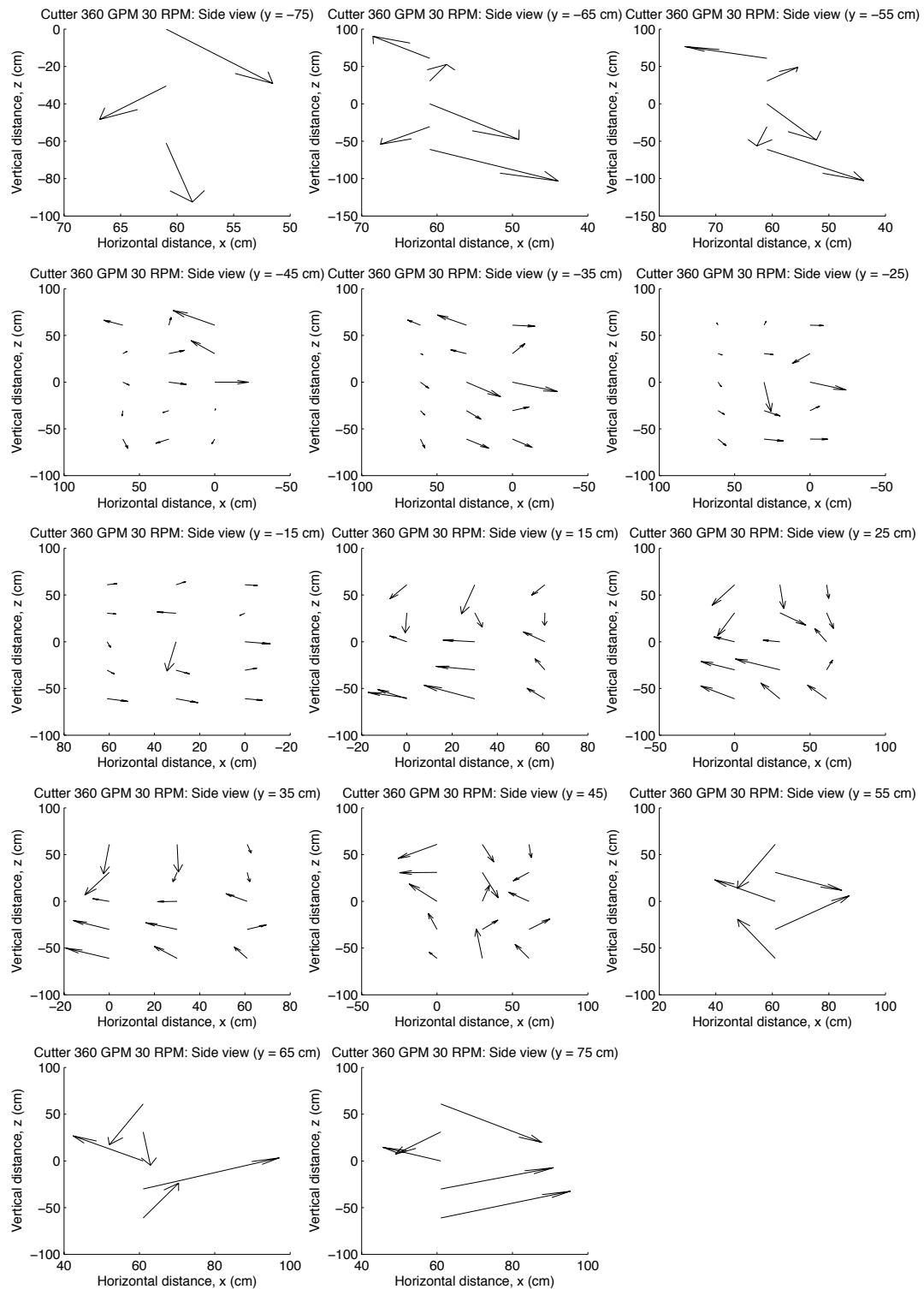


Figure 108: Quiver plots in the x-z plane for the scenario with cutterhead attached, 360 GPM, and 30 RPM.

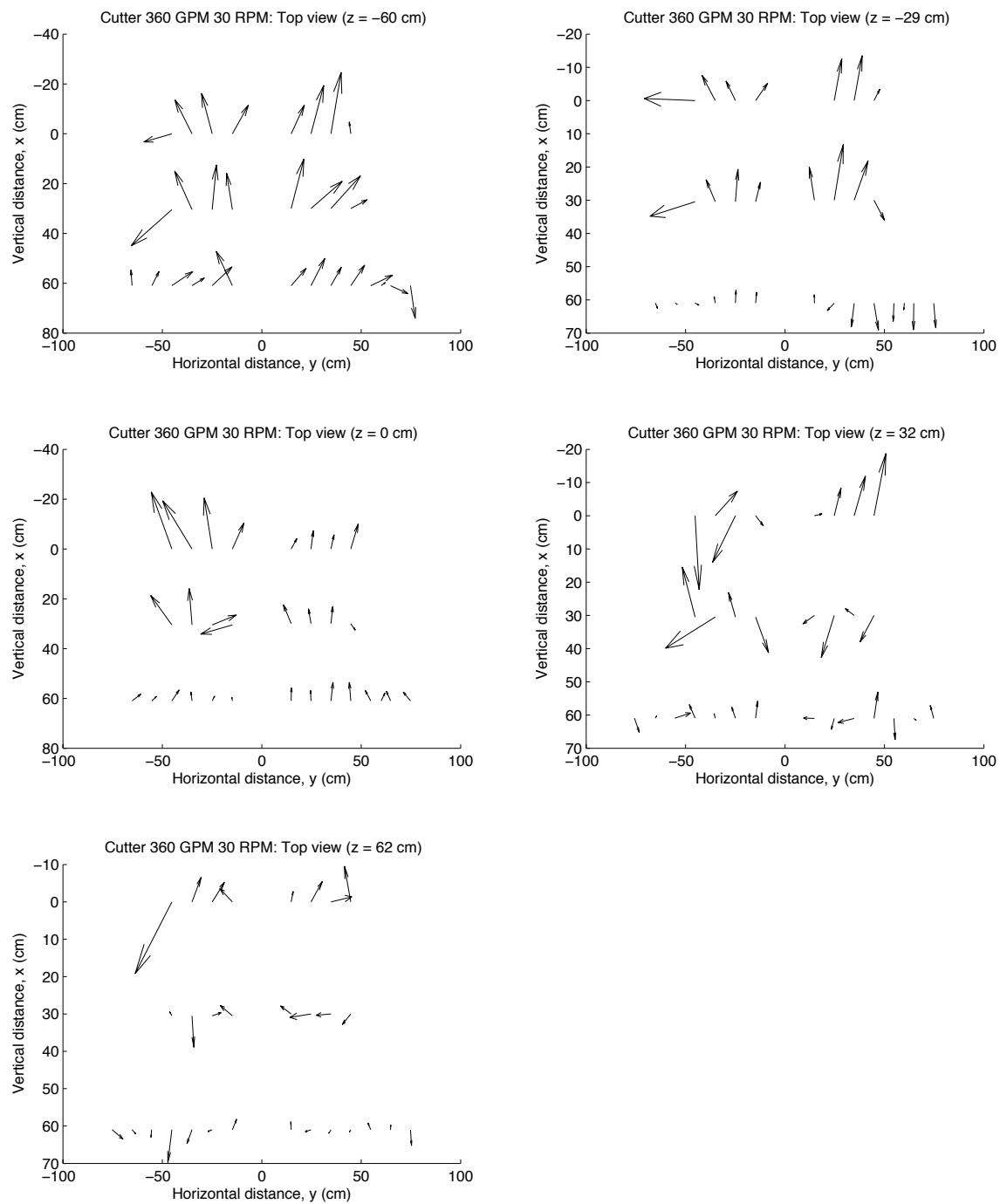


Figure 109: Quiver plots in the  $y$ - $x$  plane for the scenario with cutterhead attached, 360 GPM, and 30 RPM.

**VITA**

Name: Colin Patrick Dismuke

Address: Texas A&M University  
Center for Dredging Studies  
College Station, TX 77843-3136

Email: colin.dismuke@gmail.com

Education: B.S., Ocean Engineering, Texas A&M University, 2010